REVISION 2

1   # Uraninite from the Olympic Dam IOCG-U-Ag deposit: linking

2   # textural and compositional variation to temporal evolution

3   Edeltraud Macmillan[1,2], Nigel J. Cook[3], Kathy Ehrig[2], Cristiana L. Ciobanu[3], and Allan Pring[4]

4   [1]*School of Physical Sciences, The University of Adelaide, Adelaide, SA, 5000, Australia*

5   [2]*BHP Billiton Olympic Dam, Adelaide, SA, 5000, Australia*

6   [3]*School of Chemical Engineering, The University of Adelaide, Adelaide, SA, 5000, Australia*

7   [4]*School of Chemical and Physical Sciences, Flinders University, Bedford Park, SA, 5042,*

8   *Australia*

9   # ABSTRACT

10   The Olympic Dam IOCG-U-Ag deposit, South Australia, the World's largest economic

11   uranium (U) resource, contains three main U-minerals: uraninite; coffinite; and brannerite. Four

12   main classes of uraninite have been identified. Uraninite occurring as single grains is

13   characterised by high-Pb and ΣREE+Y (ΣREY) but based on textures can be classified into 3 of

14   these classes, typically present in the same sample. Primary uraninite (Class 1) is smallest (10-50

15   μm), displays a cubic-euhedral habit, and both oscillatory and sectorial zoning. 'Zoned' uraninite

16   (Class 2) is coarser, sub-euhedral and combines different styles of zonation in the same grain.

17   'Cob-web' uraninite (Class 3) is coarser-still, up to several hundred μm, has variable hexagonal-

18   octagonal morphologies, varying degrees of rounding, and features rhythmic intergrowths with

19   sulfide minerals. In contrast, the highest-grade U in the deposit is found as μm-sized grains to

20   aphanitic varieties of uraninite which form larger aggregates (up to mm) and vein-fillings

21   (massive, Class 4) and have lower-Pb and ΣREY, but higher Ca.

22   Nanoscale characterization of primary and cob-web uraninite shows these have defect-free

23   fluorite structure. Both contain lattice-bound Pb+ΣREY, which for primary uraninite is

24   concentrated within zones, and for cob-web uraninite is within high-Pb+ΣREY domains. Micro-

25   fractured low-Pb+ΣREY domains, sometimes with different crystal orientation to the high-

26   Pb+ΣREY domains in the same cob-web grain, contain nanoscale inclusions of galena, Cu-Fe-

27   sulfides and REY-minerals. The observed Pb zonation and presence of inclusions indicates solid-

28   state trace-element mobility during the healing of radiogenic damage, and subsequent inclusion-

29   nucleation + recrystallization during fS$_2$-driven percolation of Cu-bearing fluid.

30   Tetravalent, lattice-bound radiogenic Pb is proposed based on analogous evidence for U-

31   bearing zircon. Calculating the crystal chemical formula to UO$_2$ stoichiometry, the sum of

32   cations (M*) is ~1 for most classes, but the presence of mono-, di- and trivalent elements (ΣREY,

33   Ca etc.) drive stoichiometry towards hypostoichiometric M*O$_{2-x}$. In the absence of measured O

34   and constraints of hypostoichiometric fluorite-structure, charge balance calculations showing O

35   deficit in the range 0.15-0.29 apfu is compensated by assumption of mixed U oxidation states.

36   Crystal structural formulae show up to 0.20 apfu Pb, and 0.25 apfu ΣREY in Classes 1-3, whilst

37   for Class 4, these are an order of magnitude less. Low-Pb and ΣREY subcategories of Classes 2

38   and 3 are similar to massive uraninite with ~0.2 apfu Ca. Other elements (Si, Na, Mn, As, Nb,

39   etc.), show two distinct geochemical trends: (i) across Classes 1-3; and (ii) Class 4, whereby low-

40   Pb+ΣREY sub-populations of Classes 2 and 3 are part of trend (ii) for certain elements. Plots of

41   alteration factor (Ca+Si+Fe) versus Pb/U suggest two uraninite generations: early (high-

42   Pb+ΣREY, Classes 1-3); and late (massive, Class 4). There is evidence of Pb loss from diffusion,

43   leaching and/or recrystallization for Classes 2-3 (low-Pb+ΣREY domains).

44   Micro-analytical data and petrographic observations reported here, including nanoscale

45   characterization of individual uraninite grains, support the hypothesis for at least two main

46   uraninite mineralizing events at Olympic Dam and multiple stages of U dissolution and

47   reprecipitation. Early crystalline uraninite is only sparsely preserved, with the majority of

48   uraninite represented by the massive-aphanitic products of post-1590 Ma dissolution,

49   reprecipitation, and possibly addition of uranium into the system. Coupled dissolution-

50   reprecipitation reactions are suggested for early uraninite evolution across Classes 1 to 3. The

51   calculated oxidation state ($U^{6+}/(U^{4+}+U^{6+})$) of the 'early' and 'late' populations point to different

52   conditions at the time of formation (charge compensation for ΣREY-rich early fluids) rather than

53   auto-oxidation of uraninite. Late uraninites may have formed hydrothermally at lower

54   temperatures (T<250 °C).

55   Keywords: uranium, uraninite, Olympic Dam, IOCG deposits

INTRODUCTION

57   Uraninite (UO_2), the most abundant U^{4+} mineral found in nature, is also one of the most

58   controversial in terms of the reasoning behind compositional variation relative to crystal-

59   chemistry. It crystallizes with fluorite-type structure, space group *Fm3m* (Frondel 1958), and

60   contains two types of coordination between the atoms: 8-fold, dodecahedral for U^{4+}; and 4-fold,

61   tetrahedral, for O. However, such ideal fluorite-type structure is based on work pertaining to

62   synthetic UO_2 rather than natural uraninite.

63   Natural uraninite has a wide range of compositional variation involving cations of various

64   types, and considerable textural heterogeneity, in particular from occurrences in Precambrian

65   terranes (e.g., Frondel 1958; Janeczek and Ewing 1991, 1992b; Kotzer and Kyser 1993; Finch

66   and Murakami 1999; Förster 1999; Deditius et al. 2007; Ram et al. 2013). For example, high-

3

67   PbO (up to ~20 wt%) in uraninite is found in 'natural fisson reactors' such as Oklo (Gabon;

68   Janeczek and Ewing, 1995), but PbO contents of 7-10 wt% are more common. The high-Pb

69   content is attributed to decay of U isotopes (^{238}U and ^{235}U) to radiogenic Pb (^{206}Pb and ^{207}Pb) and

70   other radiogenic daughter products. High-CaO (up to 11 wt%), and high-REY$_2$O$_3$ (up to 12

71   wt%), are also reported (e.g., Frondel 1958; Fayek and Kyser 1997; Polito et al. 2004; Alexandre

72   and Kyser 2005). In addition to these, a larger number of minor/trace elements are noted,

73   including Th, Bi, As, W, Cu, Mo, V, Si, P, Al, Fe, Mg, Na and K (e.g., Finch and Murakami

74   1999; Alexandre and Kyser 2005; Deditius et al. 2007; Hazen et al. 2009).

75   An important consequence of the fact that uraninite contains a wide range of minor and/or

76   trace elements is that these can be used as 'mineral geochemical signatures' for tracking

77   evolutionary trends among sub-populations. Complemented by an understanding of textural

78   heterogeneity relative to compositional variation, such a 'fingerprinting' method can be used to

79   support genetic models even when sub-µm-scale mineral inclusions are present, and despite

80   uncertainties relating to crystal-structural modifications.

Crystal-structural formulae

82   In a landmark study, Janeczek and Ewing (1992b) contend that natural uraninite differs

83   markedly from synthetic UO$_2$ in that it is nonstoichiometric and has a highly defective fluorite

84   structure. These authors attribute nonstoichiometry and structural defects to: (i) oxidation of U;

85   (ii) cationic substitution; and (iii) α-decay event damage. All of these are critical for the present

86   study. Uranium oxidation is considered a ubiquitous phenomenon in natural uraninite. This

87   implies conversion of U^{4+} to U^{6+} in UO$_2$, leading to formula (1):

88           $$U_{1-x}^{4+}U_x^{6+}O_{2+x} \tag{1}$$

89   where $x \leq 0.25$ and the maximum limit of excess O in a fluorite-type structure is based on

90   Frondel (1958).

91   Cation substitution can decrease excess O below $x \sim 0.25$ if the generalized crystal-structural

92   formula (2) is considered, which can account for other, major substituents measured in natural

93   uraninite, such as REE and Y (hereafter ΣREY) or divalent metals that are incorporated within

94   the structure:

$$\left(U_{1-x-y-z}^{4+}U_x^{6+}REE_y^{3+}M_z^{2+}\right)O_{2+x-0.5y-z}. \tag{2}$$
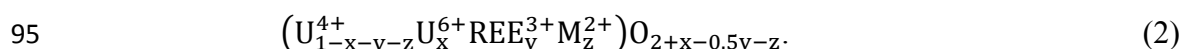
96   Tetravalent U has a comparable radius with Th^{4+}, Zr^{4+}, and REY^{3+} but not with Pb^{2+}.

Uraninite 'auto-oxidation' – mechanisms of Pb incorporation

98   There are two main ways in which Pb is thought to impact on the stability of uraninite (Finch

99   and Murakami 1999): (i) 'auto-oxidation' in which there is charge imbalance; and (ii)

100   accumulation of Pb^{2+} to levels which cannot be accommodated within the uraninite structure.

101   Hazen et al. (2009) provide an updated overview of uraninite 'auto-oxidation' in natural samples.

102   This process is linked to the intrinsic radioactive decay of ^{238}U, ultimately leading to the stable

103   decay product ^{206}Pb (Bourdon et al. 2003).

104   The formation of Pb^{2+} and its occupation of U sites requires a process of uraninite 'auto-

105   oxidation', in which U^{4+} decays to Pb^{2+}, requiring charge compensation by U^{4+} oxidation to U^{6+}

106   up to the O excess limit of $x=0.25$. However, recent studies (e.g., Utsunomiya et al. 2004;

107   Kramers et al. 2009) suggest that radiogenic Pb can be tetravalent rather than divalent, and thus

108   substitute directly for Me^{4+}. Besides the incompatible Pb^{2+} crystal chemistry at high levels, as

109   also seen for uraninite, arguments include slow rates of Pb diffusion, XANES spectra indicating

110   that Pb in titanite is not Pb^{2+} (Kramers et al. 2009), as well as HR-TEM and HAADF-STEM

111 studies observing direct substitution of Pb for Zr in the zircon structure (Utsunomiya et al. 2004).

112 Hazen et al. (2009) draw attention to an important implication of such alternative mechanisms

113 when considering reduction of Pb^{4+} to Pb^{2+} in U-bearing minerals – that it is not necessarily tied

114 to auto-oxidation of U^{4+} to U^{6+}, but potentially related to a post-radioactive decay process.

115   Another alteration mechanism for uraninite relates to production of radiogenic Pb^{2+} higher

116 than a few wt%, which was considered by Janeczek and Ewing (1995) as incompatible with the

117 uraninite structure. Such incompatibility, at high fS_2, favors formation of galena; loss of Pb from

118 uraninite may cause a reduction in overall uraninite volume without release of U^{6+} into solution.

119 However, if fS_2 is insufficient to strip Pb from the uraninite, it has been shown to develop Pb-

120 rich and –poor domains (Finch and Murakami 1999).

121   Lastly, Hazen et al. (2009) point to the fact that uraninite, unlike zircon, is more resistant to α-

122 decay damage (resulting in an aperiodic structure known as the 'metamict state') due to rapid

123 annealing kinetics (e.g., Janeczek and Ewing 1991). Such a process may, however, account for

124 lead redistribution via enhanced permeability brought about by damage to the lattice (i.e. rapid

125 Pb-diffusion coupled with rapid self-annealing of radiation damage). Formation of galena from

126 reduction of Pb^{4+} following interaction with a reducing-fluid, and formation of coffinite ($USiO_4$)

127 via interaction with Si-bearing groundwater (Deditius et al. 2009) may also occur. A further

128 possibility is the creation of 'bubbles' in U-minerals from production of radiogenic He (α-

129 particles; e.g., Roudil et al. 2008).

130 **Superstructuring in uranium oxides**

131   Recent experimental and *ab initio* crystal modeling studies (e.g., Desgranges et al. 2009;

132 Andersson et al. 2013) show that 'hyperstoichiometric' fluorite-derived UO_{2+x} is a complex

133 binary material that has large fields of homogeneity and several long-range ordered compounds

6

134   with large unit cells (superstructures with cubic or tetragonal symmetry), some of which are

135   based on the archetypal motif of the fluorite structure. Of these, the most stable compounds are

136   U_4O_{9-y} and U_3O_7, each with multiple polymorphs as a function of temperature. Such properties

137   relate to the mixed valence character of U-oxides (U exhibits stable valences of III-VI where

138   adjacent valences can easily co-exist), as well as to the clustering tendency of additional,

139   interstitial oxygen atoms in the structure. At U:O ratios higher than 3:7, the fluorite sub-structure

140   changes via shear-transformation into the layered structure of U_3O_8, with hexagonal symmetry

141   (Allen and Holmes 1995).

142   The present study uses several micro-beam techniques including Scanning Electron

143   Microscopy (SEM); Mineral Liberation Analysis (MLA); Electron Probe Microanalysis

144   (EPMA); Focused Ion Beam (FIB)-SEM and Transmission Electron Microscopy (TEM). These

145   are used to characterize textural, morphological and chemical variation in uraninite from samples

146   throughout the Olympic Dam (OD) orebody with two main goals: (i) to define the crystal-

147   chemical formula of uraninite and its variation; and (ii) to track the evolution of uraninite from

148   primary to subsequent generations.

GEOLOGICAL SETTING

150   The Olympic Dam iron-oxide copper-gold (IOCG)-uranium-silver deposit (520 km NNW of

151   Adelaide, South Australia) is part of the Olympic Cu-Au-(U) province in the eastern Gawler

152   Craton (e.g., Skirrow et al. 2007) and has been considered to define the IOCG class of deposits

153   (e.g., Hitzman et al. 1992). The deposit is hosted by the Olympic Dam Breccia Complex

154   (ODBC), which is in turn located within the Roxby Downs Granite (RDG) (Reeve et al. 1990), a

155   member of the ~1590 Ma Hiltaba Intrusive Suite (HIS; Creaser and Cooper 1993; Flint et al.

156   1993). On the Gawler Craton, the HIS are unconformably overlain by the Gawler Range

157   Volcanics (GRV), the extrusive equivalents of the HIS (Flint et al. 1993). Hiltaba Suite

158   granitoids cluster around 1588 to 1596 Ma (U-Pb zircon dating; Mortimer et al. 1988; Creaser

159   and Cooper 1993; Johnson and Cross 1995).

160   As discussed by Reeve et al. (1990), the orebody can best be thought of as a continuum from

161   granite breccia (<10% hematite) to various forms of hematite-rich breccia (from 10% to >90%

162   hematite). OD is thought to have formed in a near-surface environment, where either multiple

163   mafic maar-diatreme volcanoes vented via magmatic, phreatic and hydrothermal explosions

164   (Reeve et al. 1990; Haynes et al. 1995; Johnson and Cross 1995) or it was formed beneath and

165   partly within a sedimentary basin (McPhie et al. 2011).

166   The source of metals and fluids in IOCG deposits, including OD, remains contentious. At OD

167   ore genesis is attributed to coupled redox reactions in which a hotter, reducing Fe-rich fluid

168   mixed with cooler, oxidizing meteoric fluids (Reeve et al. 1990; Oreskes and Einaudi 1992;

169   Haynes et al. 1995). In particular, transportation and precipitation of Fe and U are thought to be

170   related, since much of the hematite contains finely disseminated U-minerals (Oreskes 1990).

171   Recently, Ciobanu et al. (2013) have shown that hematite features oscillatory and sectorial

172   zonation coincident with varying contents of U, Pb, W and Mo, inferring these elements are

173   lattice-bound. Pb-Pb ages obtained on the high-U zones in hematite indicate that the ~1.6 Ga

174   magmatic-hydrothermal event is also important in terms of U-precipitation within host minerals

175   playing a major role in defining hydrothermal alteration at OD.

176   Several superimposed events impacted on the orebody and/or surrounding region, including

177   the Kararan Orogeny (~1565-1540 Ma; Flint et al. 1993), intrusion of dolerite dykes (ca. 800

178   Ma; Zhao and McCulloch 1993), and the Delamerian Orogeny (~490-514 Ma; Foden et al.

179   2006). Each of these represent sources of heat and/or allowed for fault reactivation that may have

180   driven hydrothermal circulation, alteration and associated remobilization of ore components. All

181   these events are hereafter referred to as "resetting" events.

182   Ehrig et al. (2012) show that the ODBC features strong mineralogical and geochemical

183   zonation. Several zones of sulfides are defined upwards and lateral (from periphery to center) as:

184   chalcopyrite-pyrite, chalcopyrite-bornite, bornite-chalcocite and chalcocite; polymetallic (Zn-Pb)

185   mineralization is also recognized on the ODBC margins. Copper-U-Au mineralization is

186   associated with hematite-rich breccias (Fe >20 wt%), with strong evidence for structural control.

187   There is some degree of correlation between Cu, U and Au in higher-grade zones; intermediate

188   or low grade zones do not, however, show such a relationship (figure 4 in Ehrig et al. 2012).

189   The dominant uranium minerals are uraninite/pitchblende, coffinite and brannerite (Roberts

190   and Hudson 1983; Reeve et al. 1990). Uraninite and pitchblende have been used interchangeably,

191   but pitchblende is a textural term (with no formal mineralogical standing) and it does not cover

192   the variety of morphologies and textures at OD; the term 'uraninite' will thus be used in this

193   study. Minor to trace amounts of uranium can also be found in uranothorite, thorite, thorianite,

194   hematite, and REY-group minerals (Reeve et al. 1990; Ehrig et al. 2012; Ciobanu et al. 2013).

195   The proportion of uraninite relative to coffinite and brannerite increases with total Fe content

196   (Ehrig et al. 2012). Whereas average grain sizes of the uranium minerals are 20 μm; isolated

197   grains to aggregates of U-minerals range from <0.5 μm to >1 mm. They tend to be disseminated

198   and complexly intergrown with all minerals. Where uranium concentrations are high, micro-

199   veinlets and stringers of uraninite are common. Unlike sulfides, uranium minerals do not appear

200   to display deposit-scale zonation, e.g., no consistent patterns relative to sulfides or alteration

201   minerals (Fig. 1). However, uraninite appears to be more strongly associated with hematite and

202 sulfides whereas coffinite and brannerite tend to be more strongly associated with gangue

203 minerals (Ehrig et al. 2012).

204 Previous studies at OD focused on U-mineralization in higher-grade, central parts of the

205 deposit where the more massive, stringer-like uraninite textures are typical (Trueman et al. 1986;

206 Oreskes and Einaudi 1990; Johnson 1993). At that time, obtaining quantitative compositional

207 data for the very fine, disseminated grains was difficult. Contemporary micro-analytical

208 instrumentation offers improved resolution and imaging capability. This study also benefits from

209 the improved geological knowledge about OD over the past 20 years (e.g., extensive drill-hole

210 and mineralogical database), allowing more targeted sampling of both high- and low-grade U

211 ores.

212 # ANALYTICAL METHODS

213 Polished thin-sections were examined by SEM, using a Quanta 450 Field Emission Gun

214 (FEG) SEM with silicon-drift detector (Adelaide Microscopy, University of Adelaide). Back-

215 Scatter Electron (BSE) image montages were produced for each polished thin section from the

216 MLA 650 Environmental SEM (Central Science Laboratory, University of Tasmania). These

217 were taken to record the locations of all U-mineral grains identified by SEM, and facilitated

218 subsequent analysis.

219 Assay data were initially used (Table 1, Table A1) to ensure a range of U_3O_8 grades were

220 sampled, followed by modal mineralogical characterization by MLA (ALS Mineralogy,

221 Brisbane; measured minerals listed in Table A2). Bulk modal mineralogy (Table A3) was

222 measured using the x-ray modal (MLA XMOD) technique. Sparse phase liberation mapping

223 (MLA SPL_Lite) was employed to specifically target U-minerals and measure the relative

224 abundances of U-minerals (Table 1), as well as details of all minerals found in contact with U-

10

225   mineral grains (Figs. 2-3, Table A4). Details about the MLA system and measurement

226   techniques are given in Appendix 1.

227   Quantitative analysis of uraninite composition was obtained using a Cameca SX-Five

228   Electron Probe Micro-Analyzer (EPMA) equipped with 5 tunable wavelength-dispersive

229   spectrometers at Adelaide Microscopy, University of Adelaide. Operating conditions were 15

230   keV accelerating voltage, 100 nA beam current, 40° takeoff angle, with 0.5 to 1 μm-sized beam.

231   From Monte Carlo modeling, for a 15 keV accelerating voltage and 0.5 μm beam, the excitation

232   volume is expected to be ~150 nm (width) × 100 nm (depth) (Goemann 2012). A total of 28

233   elements were measured: U, Pb, Th, Na, Mg, Al, Si, P, S, K, Ca, Ti, Mn, Fe, Cu, As, Zr, Nb, Y,

234   Ce, La, Pr, Nd, Sm, Gd, Sr, Ba, Te. Measurements for Mg, Al, K, Sr, Ba and Te are omitted from

235   Tables 2–5 and A6–A10 as they were commonly <mdl (minimum detection limit). Elemental

236   mapping was performed at 20 keV accelerating voltage, 100 nA beam current and 1 μm beam-

237   size. Standards, X-ray lines, count times and typical mdl values are reported in Appendix 1,

238   Table A5. The Probe for EPMA software (Donovan 2014) was used for data processing.

239   Nanoscale characterization of uraninite grains was carried out on a Dual Beam FEI Helios

240   Nanolab 600 platform at Adelaide Microscopy. This was used to slice and prepare TEM foils as

241   well as for imaging, i.e., cross-section using Secondary Electron (SE) mode and Scanning

242   Transmission Electron Microscopy (STEM) modes, following procedures given in Ciobanu et al.

243   (2011); see also Appendix 1.

244   The TEM study was performed on a Philips 200CM instrument operated at 200 kV (Adelaide

245   Microscopy). The instrument is equipped with a double-tilt holder and Gatan digital camera.

246   Measurements on the electron diffractions were performed using DigitalMicrograph™.

247   Diffraction patterns were interpreted using WinWulff™ software and crystal structures from the

11

248   American Mineralogist Crystal Structure Database (www.geo.arizona.edu/AMS/amcsd.php).

249   High-Resolution TEM (HRTEM) imaging in Bright Field (BF) mode and electron diffractions

250   were used for crystal structure and nanoscale characterization of uraninite from the FIB-prepared

251   foils. In addition, TEM energy-dispersive X-Ray (EDX) spot analysis was performed to obtain

252   insights into uraninite chemistry from areas representative of different patterns, as well as to

253   identify the micro- and nanoscale inclusions.

254   # RESULTS

255   Samples were selected to ensure coverage of the broadest possible range of uraninite

256   associations throughout the OD orebody and from all sulfide zones. In order to show the

257   representative character of the 23 selected samples, they are plotted together with 300 other U-

258   bearing ore samples on diagrams showing bulk mineralogy (Fig. 1). The samples were selected

259   to represent typical deposit-wide ranges in the relative proportions of U-minerals (Fig. 1), U_3O_8

260   grades and uraninite texture type (Table 1).

261   Most samples were derived from peripheral and deeper parts of the deposit which are not as

262   intensely overprinted by superimposed cycles of brecciation and alteration as the center of the

263   deposit. A third of the samples are from granitic breccias with variable proportions (40-90%) of

264   granite clasts, whereas the other two-thirds are from hematite breccias with hematite proportions

265   ranging between 60 and >90% (Table 1). One sample in the latter category contains clasts of pre-

266   existing volcanics (GRV) rather than granite. Hematite is the stable Fe-oxide throughout all

267   samples.

268   According to MLA data, the 'closest mineral association' with uraninite (minerals in direct

269   contact with uraninite) does not change among the samples, but the relative proportions of

270   individual components within the associations help to define the four classes (Figs. 2 and 3).

12

271 Minerals found in association with uraninite are dominated by hematite and Cu-Fe-sulfides, and

272 collectively, their total abundance ranges from ~25 to ~85 wt%. The other components are either

273 relict granitic or hydrothermal minerals within the OD breccias, e.g., sericite/chlorite, fluorite,

274 carbonates, barite, quartz, alkali-feldspars, as well as REY-minerals and coffinite. Brannerite is

275 rarely found in contact with uraninite, but can be found within samples that contain uraninite

276 (Fig. 1).

277 **Uraninite petrography and textural classes**

278 Uraninite occurrence varies from dispersed, single grains with sizes ranging from ~10 μm to

279 several hundred μm (Figs. 4-6), to much finer-grains (up to few μm) forming larger aggregates

280 and a whole range of anastomozing-banded-crustiform fabrics (Fig. 7). In some samples,

281 hematite contains finer-grained (<1 μm), pervasive disseminations of uraninite (or other U-

282 bearing minerals and/or galena); this occurrence is difficult to assess compositionally since the

283 grain-size is below the microbeam resolution.

284 Single grains of uraninite have a wide range of habits, encompassing cubic, prismatic, and

285 cub-octahedral (hexagonal to octagonal planar morphologies). Such grains also tend to display

286 zonation patterns which are expressed by differing concentrations of Pb, ΣREY and Ca (±Si).

287 Higher- and lower-contrast on BSE images corresponds to higher Pb+ΣREY and Ca+Si contents,

288 respectively.

289 Four classes of uraninite have been defined based both on petrographic characteristics (size,

290 habit, textures, compositional zonation patterns and fabrics) and on composition. Class

291 discrimination in terms of the latter was founded on quantitative compositional k-means cluster

292 analyses.

Class 1: Primary uraninite

Grains with simplest cubic-habit, small in size (10-50 µm), euhedral (Fig. 4a, b) and displaying oscillatory zonation patterns parallel to the grain outline (Fig. 4a, b) are called 'primary'. This uraninite type is rare and although relatively unaltered, can feature inward marginal replacement by sulfide minerals (Fig. 4b). Sectorial zonation in cross-section is suggested by Pb-poor lamellae with diagonal arrangement (Fig. 4a). Some of the fine-grained uraninite, typically within hematite, is also included in this class.

Class 2: Zoned uraninite

Coarser, sub-euhedral grains also exist, with more complex internal heterogeneity characterized by fields of inclusions, porosity and fractures, as well as by co-existing zonation patterns which are distinct to those seen within the Class 1 uraninites. For example, one zoned uraninite with a prismatic outline displays Pb- and ΣREY-zonation only on the margins (visible on BSE images; Figs. 4c and 5b) whereas two compositionally-distinct domains, each of square shape and touching one another at one corner, were identified by EPMA mapping, forming the main middle part of the grain (Fig. 5). These Pb- and ΣREY-depleted domains are also the richest in mineral inclusions, and are partially outlined by fractures infilled by sulfide±fluorite (Fig. 5a, b).

Class 3: Cob-web uraninite

Uraninite grains featuring persistent intra-grain associations with Cu-Fe-sulfides, mostly as rhythmic intergrowths from core to margin, also display the highest complexity in habit, size and degree of grain rounding (Figs. 4d and 6). These are termed 'cob-web', and are similar in morphology to the 'cog-wheel' or '*structure en roué dentée*' uraninite textures described from Oklo, Gabon (Gauthier-Lafaye et al. 1996).

14

316   Some of the simplest cob-web grains are centered on square-shaped areas, the characteristic

317   morphology of the primary class. They display, however, rhythmic core-to-margin intergrowths

318   with sulfides such as bornite; sectorial zoning is suggested by sulfide replacement diagonally

319   crosscutting marginal zones of uraninite (Fig. 4d). Internal heterogeneity of cob-web grains is

320   also shown by incipient formation of areas with coffinite (Fig. 4d), as well as the presence of

321   more varied, micron- to nanoscale inclusions, particularly of REY-minerals (see below) and

322   galena, in addition to Cu-Fe-sulfides. Further heterogeneity is expressed as domains with

323   oscillatory zonation, different sub-grain orientations, and patchy or irregular veinlets of fluorite

324   and/or sulfides.

325   Changes in grain geometry from core to margin are commonly contained between domains of

326   uraninite and sulfides (particularly bornite). For example, grains with octagonal outlines feature

327   cores with cubic habit (Fig. 6a), and hexagonal-outlined cores are enveloped by margins with

328   extra facets (Fig. 6b). In the same grains, sectorial domains of uraninite or sulfides are present

329   either in the cores or on the margins. These domains are complemented by zones with more or

330   less coherent rhythmic intergrowths between uraninite and sulfides. The latter also displays high

331   textural variation in terms of either the relative proportions and/or the thickness of the two main

332   components. Grains with octagonal sections and simpler core to margin rhythmic intergrowths

333   may show a higher degree of rounding, although they also preserve some indication of a cubic

334   core (Fig. 6c, d). In such cases a 'swelling' of the margins may occur around lens-shaped

335   domains of fluorite.

336   **Class 4: Massive uraninite**

337   The uraninite which is characteristic of higher-grade ores, although very fine-grained in

338   comparison to all previous classes, is found in more consistent accumulations throughout a given

15

339   area in a sample. The range of observed fabrics for this class, called 'massive', encompasses

340   anastomozing-crustiform varieties (Fig. 3), symplectitic intergrowths with coffinite, pisolitic and

341   banded-crustiform varieties with sulfides, as well as colloform and aphanitic varieties (Fig. 7). In

342   general, all subtypes of massive uraninite have a 'mottled' appearance in BSE images due to

343   variation in Si and Ca contents; however, the more homogenous aphanitic subtype (grey,

344   irregular patches in BSE images, Fig. 7d) have the highest concentrations of these elements.

345   Massive uraninite is also lower in Pb and ΣREY compared to uraninite from the other three

346   classes.

347   Symplectites of uraninite and coffinite are observed as up to ~50 μm-thick envelopes around

348   more homogenous, colloform coffinite. Such associations are seen around inner cores of

349   quartz±bornite, and are hosted by a finely intergrown matrix of siderite-fluorite-sericite (Fig. 7a).

350   Fine grains of galena are present throughout the uraninite, and outer parts of the symplectites can

351   also be intergrown with bornite. Pisoliths are also observed, and consist of uraninite enveloping

352   cores of Cu-Fe-sulfides within a matrix of hematite+sericite (Fig. 7b). This uraninite subtype is

353   commonly observed within the same sample as other subtypes of massive uraninite. Another

354   form of massive uraninite are the anastomozing, banded, crustiform and colloform subtypes

355   which commonly infill fractures and cavities (Fig. 7c, d), or form fine stringers. These subtypes

356   are all intimately associated with Cu-Fe-sulfides. The thickness of uraninite bands vary widely,

357   from <1 μm up to >1 cm. In some cases, the crustiform-colloform uraninite subtypes infill the

358   space between box-work textures in hematite, or occur as part of the breccia cement.

359   **Associations and distribution of uraninite classes**

360   The majority of the single uraninite grains belong to Classes 2 and 3. Each can be further

361   subdivided into high-Pb, -ΣREY or high-Ca sub-groups since generally each individual grain

362   contains domains characterized by distinct concentrations of these elements. This is usually,

363   although not always, linked to zonation patterns or other distinct characteristics mentioned

364   above.

365   Uraninites from Classes 1-3 are typically found within the same sample. As a result, the

366   dominant minerals found in contact with these uraninites are almost identical (i.e., hematite

367   (~50%) and sulfides (~20%; Fig. 2). Other minerals found in association with uraninites of

368   Classes 1-3 include fluorite, quartz, sericite/chlorite and carbonates, although the relative

369   abundance of these minerals in direct contact with uraninite differs for Class 1 and Classes 2/3

370   uraninites. One notable feature for uraninites of Classes 1-3 is the persistent presence of REY-

371   minerals (~2-3%).

372   Massive uraninite (Class 4) is usually not present in samples with uraninite belonging to

373   Classes 1-3. The various subtypes of Class 4 uraninites are found in association with differing

374   minerals (Fig. 2). Samples with uraninite-coffinite intergrowths have relatively lower sulfide

375   content (~20%), minor hematite (~5%), but higher fluorite, barite and greatest abundance of

376   alkali-feldspars. In contrast, the other subtypes of massive uraninite are associated with hematite

377   (40%), sulfides (45%), quartz and sericite+chlorite (~10% combined); other minerals are sparse

378   to absent.

379   The distribution of uraninite classes can show a vertical zonation within a given drillcore. For

380   example, in one of the deepest drillcores (SE lobe, RD1988; Table 1), uraninite across a 1000 m-

381   thick interval (S4 to S7) ranges from massive (pisoliths and coffinite associations) at a depth of

382   ~880 m (S4), through zoned and cob-web uraninite at 1620 m to ~1770 m (S5, S6) to fine-

383   grained (primary) uraninite inclusions in hematite at a depth of ~1800 m (S7). A comparable

384   trend is broadly observed in other drillcores albeit over much smaller vertical intervals. In one

17

385   drillcore, however, primary to cob-web categories are found together over an interval of ~300 m

386   (S17-S15, RD3035; Table 1). In general, the distribution of different uraninite classes shows no

387   pattern that can be correlated with lithology or sulfide zoning; Class 4 uraninites are, however,

388   typically found within zones of the highest U-grade.

389   **Crystal structure and nanoscale characterization of uraninite**

390   FIB-SEM and TEM work was employed for crystal structure assessment and nanoscale

391   characterization of uraninite grains from Classes 1 and 3. The main purposes were to assess

392   whether there are any crystal structural modifications from primary to cob-web classes, and if the

393   presence of nanoscale inclusions can explain measured changes in concentration of minor

394   elements such as Pb, ΣREY or Ca. These issues are relevant for uraninite chemistry (EPMA data

395   in the following section), particularly for assumptions of stoichiometries other than UO_2, the

396   oxidation state of Pb, and for the interpretation of measured concentrations of elements as being

397   within the uraninite itself (lattice-bound), or due to the presence of discrete, sub-μm-sized

398   mineral inclusions (i.e., below EPMA spot size).

399   The primary uraninite grain selected is one of the smallest (~15 μm), and displays oscillatory

400   zonation patterns typical for Class 1. FIB cross-sectioning through the middle of the grain (Figs.

401   4a and 8a) with orientation parallel to the square section exposes an overall isometric, cube-

402   shaped morphology and shows that the oscillatory and sectorial zoning expands from the darker

403   center (close to the surface) to brighter margins; only the latter was retained on the TEM foil

404   after thinning (Fig. 8b). FIB-STEM imaging of this foil shows the fine-scale (<1 μm, down to

405   tens or hundreds of nm) of the oscillatory zoning (Fig. 8c). The main part of the grain contains

406   no inclusions, pores or fractures, but on one side of the grain, replacement by Cu-Fe-sulfides and

18

407   fluorite, pore-attached nanoscale inclusions (tens of nm in size) and a coarser inclusion of galena

408   (~0.5 μm), were identified (Fig. 8b, d).

409   Several grains from the cob-web class were cross-sectioned to evaluate their internal textures.

410   One of these grains displays considerable complexity: rounding and marginal replacement by

411   sulfides ± fluorite; internal domains with weak oscillatory zonation; and most importantly, the

412   presence of a zone between the inner part and the outer grain margin containing inclusions of

413   REY-minerals (Figs. 6d and 9a). In this case, the FIB cut was positioned across the boundary

414   between the REY-inclusion-rich and REY-inclusion-free domains. Ion beam imaging of the

415   grain surface prior to cross-sectioning showed the different orientations of these domains to one

416   another. FIB-STEM and TEM imaging of the foil (Fig. 9b) reveals the extension of the two

417   distinct domains at depth, as well as further details of the inclusion fields, their shape and sizes.

418   Two generations of pore-attached inclusions can be inferred (Fig. 9a), the earliest of which

419   features the coarsest pores with multi-component phases precipitated within them, and the latest

420   is characterized by trails of nm-scale inclusions and nanometer-scale veinlets crosscutting the

421   early inclusions; only a few sulfide inclusions are present. The REY-mineral inclusions range

422   from a few to hundreds of nm in size, and have either irregular or roughly euhedral shapes (Fig.

423   9c). Their speciation was identified, using TEM-EDX and electron diffraction, as synchysite

424   (coarsest, most abundant) and monazite (Ce-dominant in both cases). Selected areas of electron

425   diffractions (SAED; Fig. 9d, e) confirm distinct orientations for uraninite in the two domains,

426   i.e., *(111)** uraninite axis in each domain at 106° on the [11-2] zone axis.

427   HR-TEM imaging of the thin edges of each foil shows lattice fringes free of defects (e.g.,

428   down to [0-11] zone axis of uraninite; Fig. 10a). In addition, zero-order SAEDs with planar

429   symmetries obtained from both foils include [100] uraninite zone axes (Fig. 10b), indicating no

19

430 crystal-structural modifications in the uraninite from either primary or cob-web types. SAEDs

431 can be indexed using space group *Fm-3m* with *a*=5.468 Å (Wyckoff 1963). In contrast, uraninite

432 from the REY-inclusion-rich domain shows areas with satellite reflections along (*hkl*)* and along

433 directions parallel to the cube axes (Fig. 10c, d). Such satellite reflections are obtained from

434 areas over sizable single-grain inclusions (as in Fig. 9c) which are epitaxial with uraninite e.g.,

435 *(100)** monazite is at *½(111)** uraninite (Fig. 10c). Satellite reflections like those in Fig. 10d

436 could be attributed to the presence of still finer particles but these may also be indicative of

437 localized areas undergoing long-range super-structuring (e.g., 9 x *a* ~24.3 Å) within uraninite, as

438 suggested by experimental and *ab initio* modeling studies (Desgranges et al. 2009; Andersson et

439 al. 2013). Further work is needed to document the presence of such nanoparticles.

440   Representative TEM-EDX spectra show that uraninite from all categories hosts Pb (Fig. 10e-

441 g). The presence of REE+Y is also convincingly shown for primary uraninite and the domain

442 free of REY-mineral inclusions in the cob-web study case (Fig. 10e, f). Most importantly,

443 uraninite from the domain rich in REY-mineral inclusions in the cob-web grain shows

444 consistently lower Pb content and no ΣREY; other elements such as Ca, variably abundant, but

445 low amounts of Si, Al and/or Fe are present (Fig. 10g).

Compositional data for uraninite

Data presentation

448   Of the 23 samples analyzed in this study, Class 1 uraninites were identified in 2 samples,

449 uraninites of Classes 2-3 were found in 8 samples (including both samples containing Class 1

450 uraninites), and Class 4 uraninites were identified in 5 samples. The remaining 10 samples

451 contained fine-grained pervasive disseminations of U-minerals (Table 1). Uranium minerals in

452 all 23 samples were analyzed by EPMA, but results from only 7 samples are reported here. Two

453 factors contributed to data rejection: i) uraninite was too fine-grained to obtain "clean" spot

454 analyses; and ii) uraninite grains contained Si-Ca-Fe-bearing inclusions, or had partially

455 dissolved/altered rims making "clean" spot analysis impossible (poor analytical totals, 85-90

456 wt%). A total of 581 analyses were thus deemed acceptable (means reported in Tables 2-5 and

457 A6-A10). Roughly half represent Class 1-3 uraninites, and the others represent Class 4

458 uraninites. The mode of occurrence of uraninite, including whether it is intimately intergrown

459 with sulfides, fluorite and/or REY-minerals (Figs. 4, 6 and 7), was considered for selection of

460 compositionally homogeneous areas for EPMA analysis. Although the unique characteristics of

461 Class 1-3 uraninite make their identification relatively simple; finding these uraninites is difficult

462 because they are typically fine-grained (10-50 μm) and dispersed throughout a given sample.

463 Although only 3 analyses of primary uraninite are reported, these are critical for evaluating the

464 textural-chemical evolution of uraninite in the deposit.

465 Significant variation in grayscale is seen on BSE images of individual grains (Fig. 4a-c), due

466 to grain-scale compositional variation expressed as distinct zones or patches. EPMA analysis

467 points were selected to quantify the variation in grayscale on BSE images of individual grains

468 implying compositional variation. Hence, when the grains were sufficiently large, multiple

469 analyses were taken from different parts of the same grain.

470 EPMA data for the four textural classes are reported as mean analyses (Tables 2-5, A6-A10)

471 which emphasize the compositional differences between and within classes. Analyses are

472 presented both as wt% oxides and as atoms per formula unit (apfu), calculated on the basis of 2

473 O atoms (i.e., assumed MO_2 stoichiometry). The apfu calculations require several critical

474 assumptions: 1) Mineral stoichiometry conforms to ideal $(U.....)O_2$; 2) cation valencies given in

475 Tables 2-5 are correct; 3) S^{6+}, Fe^{3+}, Cu^+ and P^{5+} are omitted since these elements are probably

476 restricted to nanoscale inclusions; 4) As is present as As^{5+} (even though it has been reported as

477 As_2O_3); 5) all other elements measured are lattice-bound; and 6) any anion substitution (e.g., F^-,

478 OH^- or CO_3^{2-} for O^{2-}) is insignificant. To highlight the chemical variability within and between

479 uraninite classes, total apfu values have been calculated, as have ΣREY.

480 For the wt% oxides, iron is reported as Fe_2O_3 since hematite is the only co-existing Fe-oxide.

481 Lead is reported as PbO_2 rather than PbO given FIB-TEM evidence for lattice-bound Pb within

482 uraninite here, and analogy with the proposal of radiogenic Pb^{4+} in U-bearing zircon elsewhere.

483 The term "Alteration Factor" (AF) expresses $\Sigma(SiO_2+CaO+Fe_2O_3)$ wt%, and has been applied by

484 others (e.g., Alexandre and Kyser 2005; Pal and Rhede 2013) to highlight the degree of

485 hydrothermal alteration of uraninite. Uraninite that has commenced alteration to form coffinite

486 and/or various uranyl silicates will typically have lower EPMA analytical totals and contain

487 elevated SiO_2, Fe_2O_3 and CaO. Data presentation and filtering procedures are given in Appendix

488 2.

489 **EPMA data**

490 Sub-division of domains within Class 1-3 uraninites is based on PbO_2 content. There are very

491 few analyses in the range 8.0-10.0 wt% PbO_2, hence a cut-off of ≥ 8.5 wt% PbO_2 was utilized for

492 the "high-Pb" category, whereas analyses with PbO_2 contents of <8.5 wt% were considered as

493 "low-Pb". "High-Pb" and "low-Pb" domains co-exist within single zoned and cob-web uraninite

494 grains (Figs. 4b-c and 6a-b). CaO content was used in lieu of PbO_2 to differentiate between

495 different Class 4 sub-groups. A cut-off of 4 wt% CaO was chosen, but unlike PbO_2, there is no

496 natural bimodal distribution of CaO content to aid data separation.

22

497   To highlight the presence of "high-Pb" and "low-Pb" domains within a single grain,

498   representative points where EPMA analysis were made are marked on Fig. 4c. Multiple analyses

499   were made in these domains (mean values given in Table 3). Mean PbO_2 contents of the "high-

500   Pb" and "low-Pb" domains are 14.85 and 6.72 wt%, respectively.

501   On average, Class 1 uraninites (Tables 2 and A6) have analytical totals between 100.43 and

502   101.91 wt%, and contain 60.93–66.53 wt% UO_2, with high levels of other components: 17.42–

503   18.35 wt% PbO_2, <mdl–7.42 wt% ThO_2, 2.83–3.11 wt% Y_2O_3, 4.12–4.41 wt% Ce_2O_3 and 2.38–

504   3.27 wt% AF. Class 1 uraninites feature some of the lowest apfu totals, and range between 1.067

505   and 1.076.

506   Class 2 uraninites (Tables 3, A6 and A7) of the high-Pb sub-class have analytical totals

507   between 98.70 and 100.75 wt%, and contain 65.18–75.38 wt% UO_2, 13.41–17.57 wt% PbO_2,

508   <mdl–0.87 wt% ThO_2, 1.45–3.35 wt% Y_2O_3, 1.48–5.11 wt% Ce_2O_3 and 1.66–4.13 wt% AF. In

509   comparison, the low-Pb zoned uraninites have analytical totals between 95.21 and 96.68 wt%,

510   and contain 75.46–78.13 wt% UO_2, 3.64–6.72 wt% PbO_2, <mdl–0.06 wt% ThO_2, 2.24–2.99 wt%

511   Y_2O_3, 0.59–2.03 wt% Ce_2O_3 and 3.48–5.78 wt% AF. Class 2 uraninites have apfu totals between

512   1.072 and 1.114.

513   Class 3 (cob-web) uraninites of the high-Pb sub-class (Tables 4a and A8) have analytical

514   totals between 97.42 and 100.18 wt%, and contain 62.99–71.72 wt% UO_2, 12.31–18.17 wt%

515   PbO_2, < mdl–0.46 wt% ThO_2, 2.25–3.62 wt% Y_2O_3, 2.68–6.11 wt% Ce_2O_3, 2.01–3.14 wt% AF,

516   and apfu totals of 1.059-1.108. Low-Pb cob-web uraninites (Tables 4b and A9) have analytical

517   totals ranging between 95.57 and 96.94 wt%, and contain 69.52–77.80 wt% UO_2, 5.25–8.13 wt%

518   PbO_2, <mdl–0.64 wt% ThO_2, 1.58–3.58 wt% Y_2O_3, 1.01–3.45 wt% Ce_2O_3, 4.42–6.24 wt% AF,

23

519   and apfu totals between 1.076 and 1.121. Domains containing higher concentrations of CaO

520   typically have higher apfu totals.

521   All Class 4 uraninites are chemically similar and clearly distinct from uraninites of Classes 1-

522   3 (Tables 5 and A10). Massive uraninites have analytical totals ranging from 95.30 to 98.84

523   wt%, and contain 78.86–82.02 wt% UO_2, 2.18–6.92 wt% PbO_2, 0.23–0.58 wt% Na_2O, 0.27–0.63

524   wt% MnO, 0.58–1.88 wt% Y_2O_3, 0.44–0.96 wt% Ce_2O_3 and 5.07–8.04 wt% AF. Class 4

525   uraninites have the largest apfu totals (1.086 and 1.158), correlating with higher CaO

526   concentrations.

527   Uraninites of Classes 1-3 clearly contain higher PbO_2 and lower UO_2 contents than their Class

528   4 counterparts (compare PbO_2 and UO_2 data in Tables 2-4 to Table 5). Class 1 uraninites also

529   have higher ThO_2 contents than Class 2/3 uraninites (compare ThO_2 data in Table 2 to Tables 3-

530   4). All uraninites in Classes 1-3 contain elevated ΣREY compared to Class 4 uraninites (compare

531   Ce_2O_3 and Y_2O_3 data in Tables 2-4 to Table 5).

532   Chemical heterogeneity in a Class 3 uraninite grain (grain S18.12) is shown in Fig. 6a. Point 1

533   is located in sector-zoned regions of the grain with higher Pb and ΣREY (16.03 wt% PbO_2,

534   ΣREY 0.193 apfu; Table 4a) and low AF (2.37 wt%). In comparison, point 2 is located in an

535   altered domain with lower Pb (7.70 wt% PbO_2, Table 4b), similar ΣREY content (ΣREY 0.186

536   apfu; Table 4b) and higher AF (5.21 wt%). Point 3 is placed in 'wispy' uraninite (8.13 wt%

537   PbO_2, AF of 5.34 wt% and ΣREY 0.162 apfu; Table 4b). PbO_2 content and AF are clearly

538   inversely related but the ΣREY content can be elevated in both the high-Pb domains and the

539   more altered regions (high AF) of a given grain.

540   The Class 3 uraninite (grain S18.63), shown in Fig. 6b, represents a further example of

541   chemical heterogeneity. Some of the sector-zoned twins (p4) contain elevated PbO_2 (16.28 wt%;

24

542   Table 4a) and ΣREY (ΣREY 0.165 apfu), and have a lower AF of 2.83 wt%. Incipient alteration

543   of some of the sector-zoned areas can also be seen (p5) where PbO_2 content decreases (5.25

544   wt%, Table 4b), as has the ΣREY content (ΣREY 0.126 apfu), but the AF has increased to 6.23

545   wt%. This example highlights that not all sector-zoned and twinned uraninite contains elevated

546   PbO_2 and/or ΣREY, especially when altered.

547   Uraninites with higher analytical totals and ΣREY (i.e., Class 1, Table 2) tend to have the

548   lowest AF and apfu totals closer to unity. Those with the lowest analytical totals and ΣREY, but

549   highest AF and apfu totals are the low-Pb uraninites of Classes 2 and 3 (Tables 3 and 4b), as well

550   as high-Ca Class 4 uraninites (Table 5). Comparatively, the high-Pb Class 2 and 3 uraninites, and

551   the low-Ca Class 4 uraninites have higher analytical totals and ΣREY, but lower AF and apfu

552   totals. A decrease in total wt% oxides is attributable to the presence of REY-minerals containing

553   other, unmeasured components (e.g., carbon (as CO_3) in synchysite, and possibly also levels of

554   hydration). It is inferred that the higher concentrations of impurity elements (Ca, Si, Na, Mn)

555   cause the increase in total apfu. It can thus be inferred that AF rather than ΣREY contributes to

556   variation in apfu totals.

557   **DISCUSSION**

558   **Evaluation of crystal structural formulae**

559   Selected SAED and HR-TEM results show that the primary and cob-web grains both have

560   cubic, fluorite-type crystal structure, which supports the use of UO_2 stoichiometry for calculation

561   of crystal-chemical formulae of the uranium oxide phases examined here. The presence of

562   lattice-bound Pb and ΣREY within uraninite is supported by TEM-EDX measurements in the

563   oscillatory-zoned part of primary uraninite, as well as from the REY-free domain in the cob-web

25

564 uraninite grain. Nanoscale inclusions are, however, also found in both foils representing the

565 primary and cob-web uraninites. Inclusions which are pore-attached or occur along fractures are

566 indicative of replacement/alteration caused by interaction with hydrothermal fluid. Not all of the

567 identified inclusions are pore-attached or related to fractures, but all are located immediately

568 adjacent to areas which contain such inclusions.

569 The presence of galena in both primary and cob-web classes (the latter is not shown here) in

570 parts of grains affected by superimposed micro-fracturing with sulfide filling, infers intra-grain

571 mobilization of this element from the unaffected parts of the same uraninite grains where Pb is

572 trapped within the crystal lattice. Results here are concordant with findings for Pb in zircon

573 (Utsunomiya et al. 2004); it is proposed that Pb is present in two oxidation states: Pb^{4+} (lattice-

574 bound) and Pb^{2+} (inclusions). Considering the similarity between U^{4+} and Zr^{4+} in terms of ionic

575 charge and size, and the fact that both can exist as oxides (i.e., baddeleyite, ZrO_2), an assumption

576 can be made regarding the dominant Pb-species in uraninite (Pb^{4+} rather than Pb^{2+}). The Pb^{4+} ion

577 substitutes directly for U^{4+} in the crystal lattice.

578 The EPMA data (Tables 2-5) calculated at UO_2 stoichiometry show a sum of cations ~1 but

579 the presence of mono-, di- and trivalent elements (ΣREY, Ca etc.) in uraninite drive

580 stoichiometry towards hypostoichiometric M^*O_{2-x}, where M^* is the sum of cations. Charge

581 balance calculations predict an O deficit in the range 0.15-0.29 apfu. Both hypo- and

582 hyperstoichiometric compounds, UO_{2-x} and UO_{2+x}, are known from experimental work (Ruello et

583 al. 2005; Desgranges et al. 2009). Excess oxygen, up to 2.25 O atoms, has been invoked by

584 Janeczek and Ewing (1992b) to occur in (U^{6+}-bearing) uraninite without modification of the

585 fluorite structure, even though uncertainties surround the implications such hyperstoichiometry

586 have for the electronic properties of uraninite (Ruello et al. 2005; Andersson et al. 2013).

587   Evidence for up to 60 mol% ΣREY_2O_3 incorporation into uraninite, while preserving the fluorite

588   structure is given by Wilson et al. (1961). The authors discuss the unusual properties of 'mixed

589   valence' solid solutions for $UO_{2+x}La_2O_3$ and $UO_{2-x}La_2O_3$ compounds. The presence of mixed

590   valence U can thus be a form of valence compensation at the time of uraninite formation rather

591   than a consequence of an 'auto-oxidation' process as proposed by Janeczek and Ewing (1992b),

592   even if we acknowledge that both mechanisms are equally possible depending on the origin of

593   uraninite.

594   Uraninite grains studied by FIB-TEM have the fluorite structure with no unequivocal

595   evidence for superstructuring, or for the presence of other U-oxide structures (U_3O_7, U_4O_9 etc.).

596   There is a lack of information about the stability and integrity of the fluorite structure at

597   compositions of M^*O_{2-x}. We could find no evidence for ordering of O vacancies in the OD

598   uraninites by electron diffraction. Although evidence for superstructuring or other U-oxide

599   structures may yet be identified in other grains at OD, the following consideration of crystal

600   structural formulae addresses only construction of a chemical formula that maintains the

601   observed fluorite structure.

602   Modifying the structural formula for uraninite given by Janeczek and Ewing (1992b) to

603   include the minor amounts of mono- (Na) and pentavalent (Nb, As; M2) cations in our analyses,

604   yields:

$$\left({}^*U_{1-x-y-z-u-w}^{4+} U_x^{6+}\ {}^*REY_y^{3+} M1_z^{2+} Na_u^+ M2_w^{5+} \right) O_{2+x-0.5y-z-1.5u+0.5w}$$
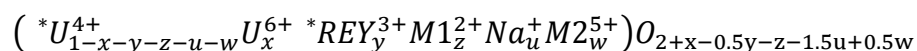
605   Other tetravalent ions (Th, Pb, Si, Zr, Ti) in our analyses are included with U^{4+} (${}^*U^{4+}$); trivalent

606   ΣREY included in ${}^*REY$; and M1 includes the divalent cations, Ca and Mn.

607   The key assumptions are: that all Pb is lattice-bound (concordant with the evidence presented)

608   and occurs in the tetravalent state; and that all the tetravalent atoms mentioned fit the U^{4+} site

27

609   rather than being interstitial. The same is valid for the ΣREY and divalent atoms here. The above

610   formula also ignores the possibility of site vacancies to achieve charge balance; abundant

611   vacancies would also induce superstructuring. As mentioned above, any measured Fe, Cu, S and

612   P are considered inclusion-bound and have been ignored, even if Fe remains a component of AF.

613   A further key assumption is that there is no F^-, or OH^- substitution for O.

614   Without independent measurement of wt% oxygen, or of the U^{6+}/U^{4+} ratio in uraninite, the

615   value of x will depend upon the stoichiometry of the compound implying $x+0.5w-0.5y-z-1.5u=0$

616   in the above formulae. We thus take the ideal M^*O_2 stoichiometry as a basis for calculating the

617   relative proportions of U^{6+} and U^{4+}. This calculation involves assigning U to U^{6+} at levels needed

618   to bring the formula to M^*O_2. Tables 6a and 6b report the recalculated structural formulae and

619   $U^{6+}/(U^{4+}+U^{6+})$ ratios for each of the 37 analyses across the four classes (Tables 2-5). Charge

620   compensation for the mono-, di- and trivalent elements at different U^{6+}/U^{4+} ratios is illustrated in

621   Fig. 11. The correlation is excellent and any deviation from perfect correlation can be ascribed to

622   a combination of analytical error, vacancies, and potentially to variation in M^*O_{2-x} ratio from

623   hypo- to hyperstoichiometry. Independent evaluation of U^{6+}/U^{4+} in uraninite would be required

624   to test the validity of these findings.

625   If the potential effects of post-depositional alteration are ignored, calculated U^{6+}/U^{4+} ratios in

626   uraninite reflect unique conditions at the time of deposition where the high ΣREY (and other

627   cations mentioned above) in uraninite requires charge compensation by additional U^{6+}. However,

628   the compatibility of LREE and Y^{3+} with U^{4+} rather than U^{6+} accounts for the formation of

629   uraninite with higher U^{4+} at that time. The presence of U^{6+}, inferred in 1.6 Ga U-bearing hematite

630   (Ciobanu et al. 2013), and the coexistence of that hematite with primary uraninite, can be

631   accounted for via numerous scenarios including by co-precipitation of the two oxides from U^{6+}-

632 bearing fluids or a U^{4+}-bearing fluid reacting with oxidized meteoric water. The high

633 concentration of ΣREY in the same fluid may also have driven stabilization of the fluorite

634 structure rather than U_3O_8 or other U^{6+}-dominant compounds. The calculated $U^{6+}/(U^{4+}+U^{6+})$

635 ratios for Class 1-3 uraninites are broadly similar (0.23-0.46), whereas the Class 4 uraninites

636 (with two exceptions) have higher values (0.42-0.52). This is consistent with their crystallization

637 at a different stage in deposit evolution, as discussed below.

Uraninite compositional ranges

639 The UO_2 content of uraninites at OD ranges from 61 to 82 wt% in Classes 1 and 4,

640 respectively (Fig. 12a). Such variability is typical for unaltered 'old' Precambrian uraninite e.g.,

641 77 and 98 wt% UO_2, for Oklo and Alm Bos, respectively (Janeczek et al. 1996). The wt% UO_2

642 variation depends on the age (U decaying to radiogenic Pb), cationic substitutions (Th, Ca,

643 ΣREY etc.), and degree of alteration/oxidation.

644 All uraninites at OD contain PbO_2 (Fig. 12b). However, PbO_2 concentrations in Class 1-3

645 uraninites are much higher (max. ~18 wt%) than in massive uraninites (max. ~7 wt%). In some

646 cases, PbO_2 concentrations are higher at the rims of the uraninite grains (Fig. 4b, c) and there is

647 reduced porosity in these domains (Fig. 4c). The inverse correlation between Pb-concentration

648 and degree of porosity may be linked to leaching and grain-scale element migration.

649 Elevated ThO_2 is only found in uraninites of Class 1 (mean 4.95 wt%, maximum 7.4 wt%,

650 Tables 2 and A6). Uraninite of Classes 2-3 contains much lower ThO_2 (<mdl-0.6 wt%, Tables 3,

651 4a, 4b, A6-A9) and <mdl ThO_2 is recorded in massive uraninite (Tables 5, A10). Uraninite

652 shows a wide range in ThO_2 content, with uraninite precipitated from magmatic or high-

653 temperature (>350 ºC) hydrothermal fluids containing 1.1 to 9.5 wt% ThO_2 (e.g., Frimmel et al.

29

654   2014). In contrast, lower-temperature (<250 °C), hydrothermal uraninite is expected to have low–

655   Th concentrations (Hazen et al. 2009).

656   The ΣREY content of OD uraninites is also variable, with uraninites of Classes 1-3 having

657   elevated ΣREY (11-16 wt% ΣREY$_2$O$_3$; Figs. 12d-e) but Class 4 has ΣREY concentrations of

658   only ~4 wt%. Such variability is reported elsewhere (e.g., Fryer and Taylor 1987; Hidaka et al.

659   1992; Förster 1999; Pal and Rhede 2013), with high-temperature uraninites (>350 °C),

660   particularly those associated with granites and pegmatites containing up to 12.5 wt% REY$_2$O$_3$. In

661   contrast, low-temperature sedimentary uraninites typically contain lower REY$_2$O$_3$.

662   Uraninites commonly contain either homogeneous or zoned-Ca distribution within individual

663   grains. The CaO content of OD uraninite ranges from ~1 to ~5 wt% for Class 1 (Fig. 13c) and

664   Class 4 uraninites, respectively. Calcium contents tend to be highest in uraninite formed at low

665   temperature or hydrothermal conditions (Frondel 1958; Janeczek and Ewing 1992a; Fayek et al.

666   2000). Magmatic uraninite tends to have CaO contents of up to 0.5 wt%, or ~12 mol% (Förster

667   1999), whereas hydrothermally altered or low-temperature uraninite can have very high CaO

668   contents of 11.9 wt% (Xu et al. 1981).

669   The AF varies from ~3 wt% for Class 1 up to ~8 wt% for some of the Class 4 uraninites (Fig.

670   13d). A similar trend can be seen for Na$_2$O and MnO (Fig. 13a, b) contents although the

671   concentrations are lower. Comparable results are reported for the McArthur River deposit, with

672   0.03 to 9.66 wt% SiO$_2$, 0.10 to 1.84 wt% FeO, and 0.06 to 3.45 wt% CaO (Alexandre and Kyser

673   2005), and thus a maximum AF of ~15 wt%.

674   **Compositional trends**

675   There are clear compositional differences between the 4 classes (Figs. 12-15). Classes 1–3

676   have higher concentrations of PbO$_2$ but lower UO$_2$ than Class 4 uraninites (Figs. 12a-b and 14a).

30

677   There is however grain-scale variability, with high- and low-PbO_2 domains within individual

678   uraninite grains of Classes 2 and 3, thus these are segregated based on 'high' versus 'low' Pb

679   contents. Uraninites of Classes 1–3 contain elevated concentrations of Ce_2O_3 and Y_2O_3, Nb_2O_5

680   (low-Pb sub-class) and As_2O_3 (low-Pb sub-class), but lower concentrations of Na_2O, MnO, CaO,

681   SiO_2, Fe_2O_3, P_2O_5, Al_2O_3 and K_2O compared to Class 4. Thus, PbO_2, Ce_2O_3, Y_2O_3 all negatively

682   correlate with UO_2 and are therefore higher in Class 1-3 uraninite. Nb_2O_5 and As_2O_3 (Figs. 13e-

683   f) display less discernable trends, but have higher concentrations in low-Pb Class 1-3 uraninites.

684   All uraninites of Classes 1-3 contain elevated Nb_2O_5 relative to Class 4 uraninites. Interestingly,

685   the As_2O_3 content of Class 4 pisoliths is similar to that of the low-Pb uraninites of Classes 2 and

686   3.

687   In most cases, and despite some overlap, the distinct chemistry of the different uraninite

688   textural classes allows for discrimination of classes (Figs. 14 and 15), especially between the

689   zoned or cob-web uraninites (low-Pb) and massive uraninites. Furthermore, AF values for the

690   massive uraninites are also higher than for the zoned and cob-web uraninites. Components

691   offering a clear discrimination include PbO_2, CaO, AF and Nb_2O_5. Oxides that do not

692   discriminate the textural classes include total oxide, Ce_2O_3, Y_2O_5, Na_2O and MnO.

693   **Uraninite evolution**

694   The genetic significance of minor and trace elements within uraninite has been the theme of

695   discussion in studies dealing with various deposit types and ages spanning from Archean to

696   recent (e.g., Leroy and Turpin 1988; Janeczek and Ewing 1992b; Kotzer and Kyser 1993; Fayek

697   et al. 1997; Alexandre and Kyser 2005; Mercadier et al. 2011). There is dispersed literature on

698   minor/trace elements signatures in uraninite from IOCG deposits, but none on IOCG-U deposits

699   such as OD. More recently, minor/trace elements signatures and distributions have been used as

31

700   a tool in provenance studies (e.g., Depiné et al. 2013; Frimmel et al. 2014). Uraninites with high

701   Th/U (>0.01) ratio or high-ΣREY (>1 wt% ΣREY; Mercadier et al. 2011) are generally formed

702   in higher temperature (i.e., >350 ^{0}C) environments, including those thought to be precipitated

703   from high-temperature magmatic or magmatic-hydrothermal fluids. The Th/U varies across the

704   different uraninite classes, with primary uraninite exhibiting the highest values and the massive

705   uraninites the lowest values. Thorium is known to partition into co-crystallizing LREE-minerals,

706   notably monazite (e.g., Watt, 1995). Monazite is one of the earliest REY-minerals formed at OD,

707   and has been identified as inclusions in magmatic apatite (Krneta et al. 2015); it is detected here

708   as nanoscale inclusions within REY-depleted domains of cob-web uraninite. Furthermore, the

709   Th/U ratio may also be used as a tracer of protolith rocks, since the highest-Th concentration is

710   in primary uraninite, which is hosted by the GRV-breccia. Uraninite from OD shows decreasing

711   trends of LREE and Y from Classes 1-3 to 4 (Fig. 14c, d), but Y is still in high-concentrations in

712   the massive categories (Y_2O_3 >1 wt%), with the exception of the coffinite-uraninite intergrowth

713   sub-type. The latter may be a consequence of the preferential incorporation of HREE (Y as a

714   proxy) into coffinite relative to uraninite.

715   The overall character of the two distinct geochemical trends: (i) primary to cob-web; and (ii)

716   massive uraninite, are shown and commented above (Figs. 12-15). The evolution of uraninite

717   across Classes 1-3 along geochemical trend (i) is particularly instructive for understanding U-

718   mineralization from early, RDG-derived hydrothermal fluids, to the later fluids responsible for

719   the main sulfide deposition at OD during the 1.6 Ga event that accounts for alteration and

720   brecciation of granite, forming the mineralized hematite-sericite breccias.

721   Few previous studies have linked textural and compositional changes in uraninite grains from

722   the micron- to nanoscale. The fact that abundant Pb and ΣREY are present within the same

723   grains, either lattice-bound (oscillatory-zoned domains), or as discrete mineral inclusions,

724   indicates that the range of textures and compositions of uraninite from primary to cob-web

725   classes follow an evolutionary trend where the same grain experiences cycles of *in-situ* growth,

726   dissolution and recrystallization. The presence of rhythmic intergrowths between uraninite and

727   Cu-Fe-sulfides, and their co-existence with domains showing changes in the crystal morphology

728   from core to margins, are indicative of fluid-mineral interactions leading to pseudomorphic

729   replacement and coarsening. This is one of the key characteristics of geochemical systems in

730   which mineral reactions involving dissolution and re-precipitation are coupled (i.e., coupled

731   dissolution re-precipitation reaction, CDRR; Putnis 2002). Importantly, CDRR also provides a

732   mechanism for mineral-fluid exchange of minor/trace elements and their redistribution within a

733   host mineral, confining them within the same grain or immediately adjacent areas.

734   TEM-EDX support for lattice-bound lead in oscillatory-zoned grains implies that following

735   uranium decay, radiogenic Pb is retained within the uraninite lattice. Reasoning for the presence

736   of (oxidized) radiogenic Pb^{4+} within zircon (Kramers et al. 2009), and thus by analogy within

737   uraninite, include: (1) Pb^{4+} has a similar charge and ionic radii to U^{4+} and Th^{4+} in the same

738   coordination (Pb^{2+} is 25% larger); (2) the radioactive decay process releases both α- and β-

739   particles, which creates a highly oxidizing environment within the host mineral, thus directly

740   producing radiogenic Pb^{4+} which is retained by uraninite; (3) the ability of the uraninite lattice to

741   accommodate intermediate daughter products of radioactive decay (i.e., restrict escape of radon),

742   in turn suggesting that little radiogenic Pb has escaped from the grain; 4) the high concentration

743   of Pb within the oldest (1.6 Ga) uraninites are linked to re-crystallization due to self-annealing of

744   radiation damage minimizing structural strain within the lattice, and thus producing the high- and

745   low-Pb domains.

746   The presence of inclusion-hosted Pb (galena), as well as regions of high- and low-Pb content,

747   may indicate that either: (i) some of the Pb^{4+} has been converted to Pb^{2+} (via auto-reduction), and

748   is forced out of the uraninite structure due to Pb^{2+} incompatibility; or (ii) radiation damage to

749   uraninite (i.e., fission tracks, metamict domains, regions impacted by release of He) has formed

750   amorphous regions which allow for Pb diffusion and/or percolation of fluids into uraninite.

751   These conclusions are concordant with data and hypotheses made for substitution by Pb^{4+} for

752   Zr^{4+} in zircon (Utsunomiya et al. 2004; Kramers et al. 2009). However, metamict domains like

753   those preserved in zircon (Utsunomiya et al. 2004) are not observed in uraninite. Instead

754   inclusion nucleation, fracture healing and recrystallization, occur much faster in uraninite than in

755   zircon (Hazen et al. 2009). Lead mobility is supported by the presence of Pb-rich and -poor

756   domains, eventually leading to different styles of zonation patterns within the same grain (Fig.

757   5). If there is an increase in fS_2 at the same time, galena and other sulfides (seen in parts of grains

758   affected by porosity and nanofractures) can form within pores. CDRR is also driven by transient

759   porosity and can thus provide a ready site for inclusion nucleation during cation diffusion or

760   fluid percolation.

761   **Uraninite generations and timing of mineralization**

762   Attempts have been made to use Pb/U ratios in uraninite to predict chemical age (e.g., Bowles

763   1990) but inaccurate age estimates can be obtained for uraninites which have perturbed U, Pb or

764   Th contents. At OD, limited studies (e.g., Trueman et al. 1986; Johnson 1993) have proposed

765   disturbance of the Pb-U systematics in uraninite, giving a range of apparent uraninite formation

766   ages and Pb loss ages, each with differing Pb/U values. For this reason, Pb/U ratios are used to

767   differentiate the relative timing of the various uraninite classes rather than for calculation of

768   absolute ages. Two distinct groups of Pb/U ratios for uraninites of Classes 1-3: 0.15-0.25 (high-

34

769 Pb types); and ~0.075 (low-Pb types) are seen on Figs. 12f and 14f. Pb/U ratios for massive

770 uraninites vary but are typically <0.075.

771 Thus there appears to be at least two generations of uraninites at OD. Uraninites of Classes 1-

772 3 (primary, zoned or cob-web type) represent an "early" uraninite generation since these contain

773 the much higher levels of Pb. Massive Class 4 uraninites represent the "late" stage of

774 mineralization.

775 Uraninite from the early generation can also be linked by trends of variation and zonation

776 patterns. Class 1 uraninites are thought to form first, and via progressive *in-situ* alteration form

777 Class 2 and 3 uraninites. This is apparent from variations in PbO_2, Ce_2O_3, Y_2O_3 (Figs. 12b, d, e)

778 and Nb_2O_5 (Fig. 13e). Based on the ΣREY and Th contents of Class 1 uraninite, it is inferred that

779 the U and ΣREY were sourced from the same, granite-derived hydrothermal fluid. Both zoned

780 and cob-web uraninites also contain elevated Na, Mn (as well as Ca, Si and Fe; Fig. 13a, b), and

781 so must have experienced some degree of alteration.

782 Chemical zonation patterns are also seen throughout uraninites of Classes 1-3 but not Class 4.

783 Solid state diffusion, driven by radiation induced self-annealing and thermal events have

784 contributed to migration of Pb and ΣREY towards the rims of the uraninite grains, causing some

785 of the observed zonation patterns. Formation of sulfides, seen as micron- to nanoscale inclusions

786 and veinlets within uraninites from primary to cob-web types, correlates with influx of Cu-S-

787 bearing fluids throughout the evolution of these uraninites.

788 Late uraninites (Class 4) are readily distinguished from the early uraninites by their low

789 ΣREY contents (Figs. 12d-e and 14c-d), elevated AF (Figs. 13d and 15d), and differences in

790 adjacent minerals (Fig. 2). Due to their low ΣREY content, Class 4 uraninites are thought to be

791 derived from lower temperature (<250 °C) hydrothermal fluids and may be interpreted as

35

792   reprecipitation products of remobilized U, or alternatively, could indicate a new influx of U from

793   an external source. Janeczek and Ewing (1992a), Kotzer and Kyser (1993), Fayek et al. (1997)

794   and Fayek and Kyser (1997) have described how old, coarse-grained, Pb-rich, Si-poor,

795   crystalline uraninites are partially or completely dissolved under oxidizing conditions, with U

796   reprecipitated as younger, fine-grained uraninites containing little Pb but enriched Si. The

797   massive uraninites are also found in association with sulfides, which are thought to aid

798   precipitation of U, as a change in redox conditions upon contact of an oxidizing fluid with a

799   reducing substrate may induce uraninite precipitation.

800   There are some similarities, notably the Pb/U ratios, between the low-Pb zoned, cob-web

801   uraninites and massive uraninites. This may indicate that the as yet inadequately constrained

802   post-1.6 Ga "resetting" events resulted in precipitation of massive uraninite, and may also have

803   induced some of the chemical zonation observed within the zoned and cob-web uraninites. Based

804   on trends identified by Evins et al. (2005), Pb-loss in OD uraninites (for example, on the plot of

805   AF versus Pb/U; Fig. 15f) appears to be driven by a combination of diffusion and

806   recrystallization, and in areas of fluid infiltration, dominated by leaching.

807   # IMPLICATIONS

808   Cycles of fluid circulation, element mobility and mineral precipitation at Olympic Dam over

809   the past 1.6 billion years remain poorly constrained. Nevertheless, the micro-analytical data and

810   petrographic observations reported here, including nanoscale characterization of individual

811   uraninite grains, provide evidence for at least two main uraninite mineralizing events at Olympic

812   Dam and multiple stages of U dissolution and reprecipitation. Although a substantial part of the

813   data presented here is focused on early crystalline uraninite, this is only sparsely preserved, with

814   the majority of uraninite represented by massive-aphanitic varieties, the products of post-1590

815 Ma dissolution, reprecipitation, and possibly addition of uranium into the system. The

816 differences in chemistry and textures between early and late uraninites highlight crystallization at

817 different stages during deposit evolution. Moreover, the calculated oxidation state

818 ($U^{6+}/(U^{4+}+U^{6+})$) of the 'early' and 'late' populations point to different conditions at the time of

819 formation. It is likely that all late uraninites formed at significantly lower temperatures (T<250

820 °C).

821   Observations of lattice-bound Pb and ΣREY within uraninite that maintains a fluorite

822 structure, and recognition of oscillatory and sectorial zoning, also add confidence in the revision

823 of the crystal structural formula outlined above. The inference of tetravalent radiogenic Pb in

824 oscillatory-zoned uraninite, as in zircon, provides another way to calculate EPMA analyses, in

825 particular for older uraninite. Validation of the oxidation states of both U and Pb should be

826 sought to endorse these interpretations, which also carry implications for the deportment and

827 mobilization of radionuclides within the deposit, and implicitly, their behavior during mineral

828 processing.

829   Results outlined here, supplemented by TEM observations, support the assumption that at

830 least part of the Pb is accommodated in the uraninite structure, and possibly as Pb^{4+}. The

831 calculation method followed is, however, only suitable if HR-TEM observations and/or XAS (X-

832 ray Absorption Spectroscopy) analyses are available. EPMA analysis alone can be readily

833 contaminated by nano-inclusions of galena or other Pb-bearing phases.

834   Further work is required to better constrain the processes involved in transformation of early

835 uraninites (primary through cob-web), and whether or not this involves superstructuring or

836 formation of other U-oxide phases. This includes assessment of the relative orientations of

837 uraninite to sulfides from cob-web categories to substantiate the hypothesis suggested here that

838   CDRR is the main driving mechanism for early uraninite evolution. Further insights into U-

839   mineralization may also be gained from interpretation of chondrite-normalized ΣREY

840   fractionation trends and other trace element patterns for distinct uraninite populations.

841   Uraninite is, however, only part of the uranium mineralization story at OD. Coffinite and

842   brannerite are also present, and work is ongoing to understand their formation, chemical

843   composition and relationships with other minerals. A robust genetic model for the OD deposit

844   will be developed in the future, and a key foundation for this will be an understanding of the

845   evolution of uranium mineralogy, particularly the correlation of textures with compositions, and

846   with age populations obtained by uraninite geochronology. Such outcomes could ultimately form

847   the basis for a conceptual model that could be applied to analogous U-bearing IOCG systems

848   formed in the aftermath of the Great Oxidation Event at ~2.2 Ga.

ACKNOWLEDGEMENTS

REFERENCES

860

861 Alexandre, P. and Kyser, T.K. (2005) Effects of Cationic Substitutions and Alteration in

862   Uraninite, and Implications for the Dating of Uranium Deposits. The Canadian Mineralogist,

863   43, 1005-1017.

864 Allen, G.C. and Holmes, N.R. (1995) A mechanism for the UO_2 to α-U_3O_8 phase transformation.

865   Journal of Nuclear Materials, 223, 231-237.

866 Andersson, D.A., Baldinozzi, G., Desgranges, L., Conradson, D.R. and Conradson, S.D. (2013)

867   Density Functional Theory Calculations of UO_2 Oxidation: Evolution of UO_{2+x}, U_4O_{9-y}, U_3O_7,

868   and U_3O_8. Inorganic Chemistry, 52, 2769-2778.

869 Bourdon, B., Henderson, G.M., Lundstrom, C.C. and Turner, S.P. (2003) Introduction to U-

870   series geochemistry. In B. Bourdon, G.M. Henderson, C.C. Lundstrom and S.P. Turner, Eds.,

871   Uranium-Series Geochemistry, 52, p. 1-21. Reviews in Mineralogy and Geochemistry,

872   Mineralogical Society of America, Chantilly, Virginia.

873 Bowles, J.F.W. (1990) Age dating of individual grains of uraninite in rocks from electron

874   microprobe analyses. Chemical Geology, 83, 47-53.

875 Ciobanu, C.L., Cook, N.J., Utsunomiya, S., Pring, A. and Green, L. (2011) Focussed ion beam-

876   transmission electron microscopy applications in ore mineralogy: Bridging micro- and

877   nanoscale observations. Ore Geology Reviews, 42, 6-31.

878 Ciobanu, C.L., Wade, B.P., Cook, N.J., Schmidt Mumm, A. and Giles, D. (2013) Uranium-

879   bearing hematite from the Olympic Dam Cu-U-Au deposit, South Australia: A geochemical

880   tracer and reconnaissance Pb-Pb geochronometer. Precambrian Research, 238, 129-147.

881 Creaser, R.A. and Cooper, J.A. (1993) U-Pb geochronology of middle Proterozoic felsic

882 magmatism surrounding the Olympic Dam Cu-U-Au-Ag and Moonta Cu-Au-Ag deposits,

883 South Australia. Economic Geology, 88, 186-197.

884 Deditius, A.P., Utsunomiya, S. and Ewing, R.C. (2007) Fate of trace elements during alteration

885 of uraninite in a hydrothermal vein-type U-deposit from Marshall Pass, Colorado, USA.

886 Geochimica et Cosmochimica Acta, 71, 4954-4973.

887 Deditius, A.P., Utsunomiya, S., Wall, M.A., Pointeau, V. and Ewing, R.C. (2009) Crystal

888 chemistry and radiation-induced amorphization of P-coffinite from the natural fission reactor

889 at Bangombé, Gabon. American Mineralogist, 94, 827-837.

890 Depiné, M., Frimmel, H.E., Emsbo, P., Koenig, A.E. and Kern, M. (2013) Trace element

891 distribution in uraninite from Mesoarchaean Witwatersrand conglomerates (South Africa)

892 supports placer model and magmatogenic source. Mineralium Deposita, 48, 423-435.

893 Desgranges, L., Baldinozzi, G., Rousseau, G., Nièpce, J.-C. and Calvarin, G. (2009) Neutron

894 Diffraction Study of the in Situ Oxidation of UO_2. Inorganic Chemistry, 48, 7585-7592.

895 Donovan, J.J. (2014) Probe for EPMA: Acquistion, Automation and Analysis. Ver. 10.3.5

896 Xtreme Edition, Probe Software, Inc., Oregon, United States of America.

897 Ehrig, K., McPhie, J. and Kamenetsky, V. (2012) Geology and mineralogical zonation of the

898 Olympic Dam Iron Oxide Cu-U-Au-Ag deposit, South Australia. In J.W. Hedenquist, M.

899 Harris and F. Camus, Eds., Geology and Genesis of Major Copper Deposits and Districts of

900 the World: A Tribute to Richard H. Sillitoe, Special Publication Number 16, p. 237-267.

901 Society of Economic Geologists, Littleton, Colorado.

902 Evins, L.Z., Jensen, K.A. and Ewing, R.C. (2005) Uraninite recrystallization and Pb loss in the

903   Oklo and Bangombé natural fission reactors, Gabon. Geochimica et Cosmochimica Acta, 69,

904   1589-1606.

905 Fayek, M., Burns, P., Guo, Y.X. and Ewing, R.C. (2000) Micro-structures associated with

906   uraninite alteration. Journal of Nuclear Materials, 277, 204-210.

907 Fayek, M., Janeczek, J. and Ewing, R.C. (1997) Mineral chemistry and oxygen isotopic analyses

908   of uraninite, pitchblende and uranium alteration minerals from the Cigar Lake Deposit,

909   Saskatchewan, Canada. Applied Geochemistry, 12, 549-565.

910 Fayek, M. and Kyser, T.K. (1997) Characterization of multiple fluid-flow events and rare-earth-

911   element mobility associated with formation of unconformity-type uranium deposits in the

912   Athabasca Basin, Saskatchewan. The Canadian Mineralogist, 35, 627-658.

913 Finch, R.J. and Murakami, T. (1999) Systematics and paragenesis of uranium minerals. In P.C.

914   Burns and R.J. Finch, Eds., Uranium: Mineralogy, Geochemistry and the Environment, 38, p.

915   91-179. Reviews in Mineralogy and Geochemistry, Mineralogical Society of America,

916   Chantilly, Virginia.

917 Flint, R.B., Blissett, A.H., Conor, C.H., Cowley, W.M., Cross, K.C., Creaser, R.A., Daly, S.J.,

918   Krieg, G.W., Major, R.B., Teale, G.S. and Parker, A.J. (1993) Mesoproterozoic. In J.F.

919   Drexel, W.V. Preiss and A.J. Parker, Eds., The Geology of South Australia: The Precambrian,

920   1, Bulletin 54, p. 106-169. Geological Survey of South Australia, Adelaide.

921 Foden, J., Elburg, M., Dougherty-Page, J. and Burtt, A. (2006) The timing and duration of the

922   Delamerian Orogeny: Correlation with the Ross Orogen and implications for Gondwana

923   assembly. The Journal of Geology, 114, 189-210.

924   Förster, H.J. (1999) The chemical composition of uraninite in Variscan granites of the

925   Erzgebirge, Germany. Mineral Magazine, 63.

926   Frimmel, H.E., Schedel, S. and Brätz, H. (2014) Uraninite chemistry as forensic tool for

927   provenance analysis. Applied Geochemistry, 48, 104-121.

928   Frondel, C. (1958) Systematic mineralogy of uranium and thorium. U.S. Geological Survey

929   Bulletin.

930   Fryer, B.J. and Taylor, R.P. (1987) Rare-earth element distributions in uraninites: Implications

931   for ore genesis. Chemical Geology, 63, 101-108.

932   Gauthier-Lafaye, F., Holliger, P. and Blanc, P.L. (1996) Natural fission reactors in the

933   Franceville basin, Gabon: A review of the conditions and results of a "critical event" in a

934   geologic system. Geochimica et Cosmochimica Acta, 60, 4831-4852.

935   Goemann, K. (2012) Mineral analysis by EPMA. AMAS12 EPMA workshop presentation notes,

936   p. 6-14. Australian Microbeam Analysis Society, Sydney, Australia.

937   Haynes, D.W., Cross, K.C., Bills, R.T. and Reed, M.H. (1995) Olympic Dam ore genesis: a

938   fluid-mixing model. Economic Geology, 90, 281-307.

939   Hazen, R.M., Ewing, R.C. and Sverjensky, D.A. (2009) Evolution of uranium and thorium

940   minerals. American Mineralogist, 94, 1293-1311.

941   Hidaka, H., Holliger, P., Shimizu, H. and Masuda, A. (1992) Lanthanide tetrad effect observed in

942   the Oklo and ordinary uraninites and its implication for their forming processes. Geochemical

943   Journal, 26, 337-346.

944   Hitzman, M.W., Oreskes, N. and Einaudi, M.T. (1992) Geological characteristics and tectonic

945   setting of proterozoic iron oxide (Cu-U-Au-REE) deposits. Precambrian Research, 58, 241-

946   287.

947   Janeczek, J. and Ewing, R.C. (1991) X-ray powder diffraction study of annealed uraninite.

948   Journal of Nuclear Materials, 185, 66-77.

949   —— (1992a) Dissolution and alteration of uraninite under reducing conditions. Journal of

950   Nuclear Materials, 190, 157-173.

951   —— (1992b) Structural formula of uraninite. Journal of Nuclear Materials, 190, 128-132.

952   —— (1995) Mechanisms of lead release from uraninite in the natural fission reactors in Gabon.

953   Geochimica et Cosmochimica Acta, 59, 1917-1931.

954   Janeczek, J., Ewing, R.C., Oversby, V.M. and Werme, L.O. (1996) Uraninite and UO_2 in spent

955   nuclear fuel: a comparison. Journal of Nuclear Materials, 238, 121-130.

956   Johnson, J.P. (1993) The geochronology and radiogenic isotope systematics of the Olympic Dam

957   Copper-Uranium-Gold-Silver deposit, South Australia, unpublished Ph.D. thesis, The

958   Australian National University, Canberra, Australia.

959   Johnson, J.P. and Cross, K.C. (1995) U-Pb geochronological constraints on the genesis of the

960   Olympic Dam Cu-U-Au-Ag deposit, South Australia. Economic Geology, 90, 1046-1063.

961   Kotzer, T.G. and Kyser, T.K. (1993) O, U, and Pb isotopic and chemical variations in uraninite:

962   implications for determining the temporal and fluid history of ancient terrains. American

963   Mineralogist, 78, 1262-1274.

964   Kramers, J., Frei, R., Newville, M., Kober, B. and Villa, I. (2009) On the valency state of

965   radiogenic lead in zircon and its consequences. Chemical Geology, 261, 4-11.

966   Krneta, S., Ciobanu, C.L., Cook, N.J., Ehrig, K. and Kamenetsky, V.S. (2015) Apatite in the

967   Olympic Dam Fe-oxide Cu-U-Au-Ag deposit. In Proceedings for Mineral Resources in a

968   Sustainable World, 3, p. 1103-1106. 13th Biennial SGA Meeting, Nancy, France, August

969   2015.

970   Leroy, J.L. and Turpin, L. (1988) REE, Th and U behaviour during hydrothermal and supergene

971   processes in a granitic environment. Chemical Geology, 68, 239-251.

972   McPhie, J., Kamenetsky, V.S., Chambefort, I., Ehrig, K. and Green, N. (2011) Origin of the

973   supergiant Olympic Dam Cu-U-Au-Ag deposit, South Australia: Was a sedimentary basin

974   involved? . Geology, 39, 795-798.

975   Mercadier, J., Cuney, M., Lach, P., Boiron, M.-C., Bonhoure, J., Richard, A., Leisen, M. and

976   Kister, P. (2011) Origin of uranium deposits revealed by their rare earth element signature.

977   Terra Nova, 23, 264-269.

978   Mortimer, G.E., Cooper, J.A., Paterson, H.L., Cross, K.C., Hudson, G.R.T. and Uppill, R.K.

979   (1988) Zircon U-Pb dating in the vicinity of the Olympic Dam Cu-U-Au deposit, Roxby

980   Downs, South Australia. Economic Geology and the Bulletin of the Society of Economic

981   Geologists, 83, 694-709.

982   Oreskes, N. (1990) American geological practice: participation and examination. Part 1: Origin

983   of REE-enriched hematite breccias at Olympic Dam, South Australia, unpublished Ph.D.

984   thesis, Stamford University, Stamford, CA.

985   Oreskes, N. and Einaudi, M.T. (1990) Origin of rare earth element-enriched hematite breccias at

986   the Olympic Dam Cu-U-Au-Ag deposit, Roxby Downs, South Australia. Economic Geology,

987   85, 1-28.

988   —— (1992) Origin of hydrothermal fluids at Olympic Dam; preliminary results from fluid

989   inclusions and stable isotopes. Economic Geology, 87, 64-90.

990   Pal, D.C. and Rhede, D. (2013) Geochemistry and chemical dating of uraninite in the Jaduguda

991   Uranium Deposit, Singhbhum Shear Zone, India - Implications for uranium mineralization

992   and geochemical evolution of uraninite. Economic Geology, 108, 1499-1515.

993   Polito, P.A., Kyser, T.K., Marlatt, J., Alexandre, P., Bajwah, Z. and Drever, G. (2004)

994   Significance of Alteration Assemblages for the Origin and Evolution of the Proterozoic

995   Nabarlek Unconformity-Related Uranium Deposit, Northern Territory, Australia. Economic

996   Geology, 99, 113-139.

997   Putnis, A. (2002) Mineral replacement reactions: from macroscopic observations to microscopic

998   mechanisms. Mineral Magazine, 66, 689-708.

999   Ram, R., Charalambous, F.A., McMaster, S., Pownceby, M.I., Tardio, J. and Bhargava, S.K.

1000   (2013) Chemical and micro-structural characterisation studies on natural uraninite and

1001   associated gangue minerals. Minerals Engineering, 45, 159-169.

1002   Reeve, J.S., Cross, K.C., Smith, R.N. and Oreskes, N. (1990) The Olympic Dam copper-

1003   uranium-gold-silver deposit, South Australia. In F.E. Hughes, Ed., Geology of Mineral

1004   Deposits of Australia and Papua New Guniea, 14, p. p. 1009-1035. Australian Institute of

1005   Mining & Metallurgy Monograph, Melbourne.

1006   Roberts, D.E. and Hudson, G.R.T. (1983) The Olympic Dam copper-uranium-gold deposit,

1007   Roxby Downs, South Australia. Economic Geology, 78, 799-822.

1008   Roudil, D., Bonhoure, J., Pik, R., Cuney, M., Jégou, C. and Gauthier-Lafaye, F. (2008) Diffusion

1009   of radiogenic helium in natural uranium oxides. Journal of Nuclear Materials, 378, 70-78.

1010   Ruello, P., Petot-Ervas, G., Petot, C. and Desgranges, L. (2005) Electrical conductivity and

1011   thermoelectric power of uranium dioxide. Journal of the American Ceramic Society, 88, 604-

1012   611.

1013   Skirrow, R.G., Bastrakov, E.N., Barovich, K., Fraser, G.L., Creaser, R.A., Fanning, C.M.,

1014   Raymond, O.L. and Davidson, G.J. (2007) Timing of Iron Oxide Cu-Au-(U) hydrothermal

45

1015   activity and Nd isotope constraints on metal sources in the Gawler Craton, South Australia.

1016   Economic Geology, 102, 1441-1470.

1017   Trueman, N.A., Long, J.V.P., Reed, S.J.B. and Chinner, G.A. (1986) The lead-uranium

1018   systematics, and rare-earth-element distributions of some Olympic Dam and Stuart Shelf

1019   mineralization. Internal Report, Western Mining Corporation, Adelaide.

1020   Utsunomiya, S., Palenik, C.S., Valley, J.W., Cavosie, A.J., Wilde, S.A. and Ewing, R.C. (2004)

1021   Nanoscale occurrence of Pb in an Archean zircon. Geochimica et Cosmochimica Acta, 68,

1022   4679-4686.

1023   Watt, G.R. (1995) High-thorium monazite-(Ce) formed during disequilibrium melting of

1024   metapelites under granulite-facies conditions. Mineralogical Magazine, 59, 735-743.

1025   Wilson, W.B., Alexander, C.A. and Gerds, A.F. (1961) Stabilization of UO_2. Journal of

1026   Inorganic and Nuclear Chemistry, 20, 242-251.

1027   Wyckoff, R.W.G. (1963) Crystal Structures, 2nd ed., Wiley Publishers, New York.

1028   Xu, G., Wang, A., Gu, Q., Zhang, J., Zhang, Z. and Huang, Y. (1981) Some characteristics of

1029   uranium oxides in China. Bulletin de Mineralogie, 104, 565-574.

1030   Zhao, J.-x. and McCulloch, M.T. (1993) Sm-Nd mineral isochron ages of Late Proterozoic dyke

1031   swarms in Australia: evidence for two distinctive events of mafic magmatism and crustal

1032   extension. Chemical Geology, 109, 341-354.

1033   **FIGURE CAPTIONS**

1034   Fig. 1: Ternary plots displaying mineralogical variability of typical OD ores compared to

1035   samples selected for this study. Data plotted are analyzed modal abundances (wt%) from

1036   MLA XMOD and SPL_Lite shown as relative proportions of: **(a)** uraninite, coffinite and

1037   brannerite (SPL data); **(b)** hematite, quartz and sericite (XMOD data); **(c)** chalcocite, bornite

1038   and chalcopyrite (XMOD data); **(d)** pyrite, bornite and chalcopyrite (XMOD data).

1039   Fig. 2: Column chart displaying wt% of various minerals in association with uraninite (MLA

1040   data; Table A4). Association data have been averaged for selected samples in each class,

1041   namely: Class 1 data are average of S15 and S17; Classes 2 & 3 data are average of S2, S5,

1042   S6, S15, S17, S18, S19 and S23; Class 4 (coff/uran intergrowths) data are values for S1; Class

1043   4 (crustiform/pisoliths) data are average of S4, S11 and S21.

1044   Fig. 3: Typical OD uraninite texture (S4) from a high-grade uranium zone within hematitic

1045   breccia. Uraninite and sulfides (chalcocite and bornite) are contiguous (almost vein-like) and

1046   are intimately intergrown, with crustiform to stringer-like and massive uraninite. Hematite

1047   and quartz are the dominant components of the breccia. In some cases, uraninite rims discrete

1048   hematite and/or quartz grains. The grain outlines of quartz and/or hematite grains are

1049   sometimes irregular and resemble dissolution textures. **(a)** False color MLA SPL_Lite map;

1050   **(b)** Back-scatter electron (BSE) image of area mapped in (a).

1051   Fig. 4: Back-scatter electron (BSE) images of selected primary, zoned and cob-web uraninites

1052   with brightness and contrast optimized to display chemical zonation; **(a)** euhedral, cubic Class

1053   1 (primary) uraninite (Urn, S15.68, Table 2) in matrix of quartz (Qz), sericite (Ser) and

1054   hematite (Hem), showing oscillatory zonation of $U \pm Pb \pm \Sigma REY \pm Ca \pm Fe$ (box indicates

1055   where TEM foil was cut); **(b)** Class 2 (zoned) uraninite (S17, Table 2) in hematite, sericite,

1056   bornite (Bn) matrix displaying oscillatory zonation due to variation in $U \pm Pb \pm Ca \pm \Sigma REY$,

1057   with inward marginal replacement by bornite (bornite colored black within grain bounded by

1058   dashed line); **(c)** Class 2 (zoned), prismatic uraninite (S17.12, Table 3) with bornite and

1059   fluorite (Fl) infilling cracks; note decrease in porosity between central region and rim possibly

47

1060   due to migration of radiogenic Pb towards the rim (white dotted lines). Chemical variability of

1061   U ± Pb ± Ca ± Si ± ΣREY highlighted by mean composition values in Table 3 (where p1, p2

1062   represent example spot locations); **(d)** broken Class 3 (cob-web) uraninite (S17.26, Table 4a)

1063   displaying concentric ringed intergrowths of uraninite and bornite with some bornite

1064   replacement diagonally crosscutting marginal zones. Fluorite blebs also present with incipient

1065   formation of coffinite (Cof).

1066 Fig. 5: BSE images and false color EPMA maps of Class 2 (zoned) uraninite (S17.12, Table 3):

1067   **(a)** BSE image of zoned, prismatic uraninite (Urn) with bornite (Bn) and fluorite (Fl) infilling

1068   cracks, surrounded by hematite (Hem), quartz (Qz), sericite (Ser), bornite and fluorite; **(b)**

1069   reduced brightness and contrast of uraninite in (a) highlighting chemical variability, with

1070   increased Pb and ΣREY and reduced porosity towards rim (white dotted lines); **(c-f)** EPMA

1071   maps displaying the relative distribution in Pb (measurement mode: WDS), S (EDS), Ce

1072   (WDS) and Nd (EDS), respectively. Note that square chemical zonation pattern differs from

1073   the outline of the prismatic grain.

1074 Fig. 6: BSE images of Class 3 (cob-web uraninites); **(a)** cob-web uraninite grain (Urn, S18.12)

1075   with rhythmic core-to-margin intergrowths of uraninite and bornite. Octagonal grain outline

1076   features a core with cubic habit containing bornite and fluorite. Sectorial domains of higher

1077   Pb/ΣREY uraninite are present, as well as more wispy, less coherent uraninite (higher Ca, Si);

1078   see Tables 4a (p1) and 4b (p2, p3) for selected spot analyses expressing variation in U ± Pb ±

1079   Ca ± Si ± ΣREY; **(b)** cob-web uraninite (S18.63), with hexagonal-outlined core. Displays

1080   twinning and contains sectorial zonation, also with wispy (higher Ca, Si) uraninite. Entire

1081   grain contained within a hematite (Hem) lath; see Tables 4a (p4) and 4b (p5) for selected spot

1082   analyses; **(c)** cob-web uraninite (S15.22) with rhythmic intergrowths and inclusions of

1083   chalcopyrite (Ccp) and fluorite (Fl). Displays higher degree of rounding, and 'swelling' of the

1084   margins, possibly due to multiple stages of uranium dissolution and reprecipitation and/or

1085   new fluorite growth; **(d)** cob-web uraninite (S15.3, Table 4a, b) with cubic-habit uraninite at

1086   center, chalcopyrite and fluorite rhythmic intergrowths (box indicates TEM foil location).

1087   Fig. 7: BSE images of Class 4 (massive) uraninites; **(a)** complex intergrowth of massive

1088   uraninite (Urn-(Pb)=high Pb, S1, Table 5) with uraninite-coffinite symplectites around more

1089   homogenous, colloform coffinite(Cof) rimming quartz (Qz). Fine-grained galena (Gn) and

1090   bornite (Bn) are present throughout the uraninite. Matrix consists of finely intergrown fluorite,

1091   siderite (Sd) and sericite (Ser); **(b)** uraninite-bornite pisoliths (S4, Table 5) associated with

1092   sericite and hematite (Hem) laths and hematite-bornite clasts in quartz matrix; **(c)**

1093   crustiform/banded massive uraninite (S21, Table 5) associated with bornite and quartz; **(d)**

1094   massive uraninite (S11.52, Table 5) associated with chalcopyrite; reduced brightness and

1095   contrast reveal mottling due to variation in Ca and Si content, as well as domains of Si-rich

1096   aphanitic uraninite (homogeneous grey patches).

1097   Fig. 8: **(a)** Secondary Electron (SE) image showing oscillatory and sectorial zoning in Class 1

1098   (primary) uraninite, as exposed by FIB-cross sectioning of grain in Fig. 4a. **(b)** TEM image

1099   showing uraninite and surrounding minerals in the foil obtained after lifting and thinning slice

1100   in (a). Note the foil represents only the lower part of the sectioned grain; i.e., black outline on

1101   (a), which is higher in Pb (+ ΣREY) concentrations (brighter zone on the SE and BSE

1102   images). Note also sulfides and fluorite inclusions on left but no inclusions or fractures

1103   throughout main part of foil. **(c)** Partial High Angle Dark Field (HADF)-STEM image

1104   showing detail of zonation. The area is marked by a square in (b). Note absence of inclusions

1105   and fractures, as well as the sub-μm scale of the oscillatory zoning pattern **(d)** SE image

1106   showing sub-μm galena inclusion in uraninite at location marked in (b). Fluor-fluorite; Gn-

1107   galena; Hm-hematite; Ser-sericite; Urn-uraninite.

1108   Fig. 9: **(a)** SE image showing location of FIB cut (Pt strip as bright rectangle) across grain in Fig.

1109   6d. This was set across two domains differing in terms of the presence of REY-mineral

1110   inclusions (bounded by dashed line) and with different orientations (as seen from ion beam

1111   imaging during cross-sectioning). Two generations of pore-attached inclusions can be

1112   inferred: (i) early coarser pores with multi-component phases precipitated within them; and

1113   (ii) trails of nm-scale inclusions and nm-scale veinlets crosscutting the early inclusions with

1114   only a few sulfide inclusions present. **(b)** Collage of TEM images showing foil obtained from

1115   FIB-cut in (a). Dashed line separates the domain rich in REY-mineral inclusions. **(c)** TEM

1116   image showing some of the largest REY-mineral inclusions in an area marked on (b). **(d-e)**

1117   SAEDs obtained at the same specimen tilt. i.e., down to [11-2] zone axis in uraninite, showing

1118   the different orientation of the two domains; location of SAEDs is shown as white circles on

1119   (b). The angle between (111)* uraninite axis in each domain is ~60^0. Abbreviations as Fig. 8;

1120   Mon-monazite; Ser-sericite; Synch-synchysite-(Ce).

1121   Fig. 10: **(a)** HR-TEM image showing lattice fringes for uraninite (sample S15.68) with

1122   orientation as shown in the SAED from the inset. **(b-d)** SAEDs showing uraninite down to

1123   zone axes as marked from sample S15.68 in (b) and sample S15.3 in (c-d). Note the coherent

1124   intergrowths between (111)* axis in uraninite and (100)* axis in monazite in (c). In (d)

1125   satellite reflections (arrowed) are present parallel to (h00) rows in uraninite. **(e-f)** TEM-EDX

1126   spectra of uraninite from locations as marked on Figs. 8c and 9b. Note absence of REY peaks
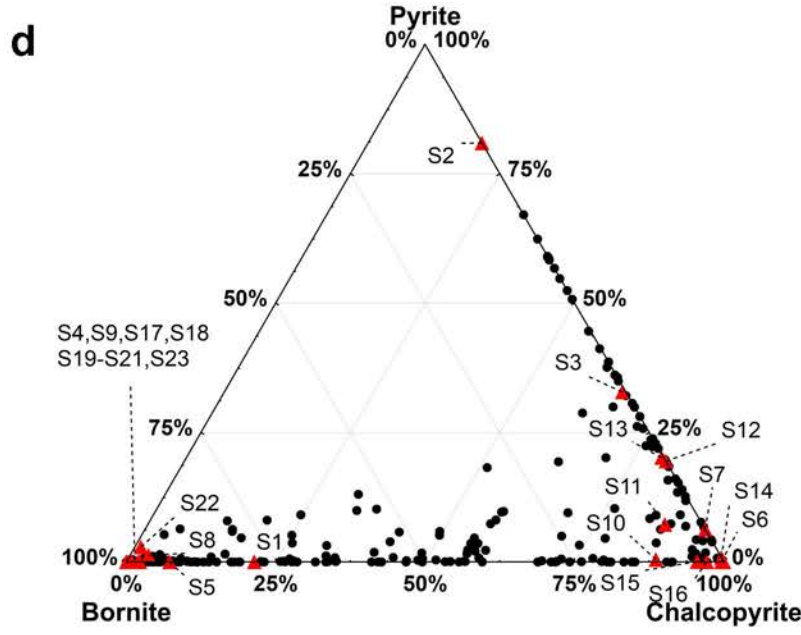
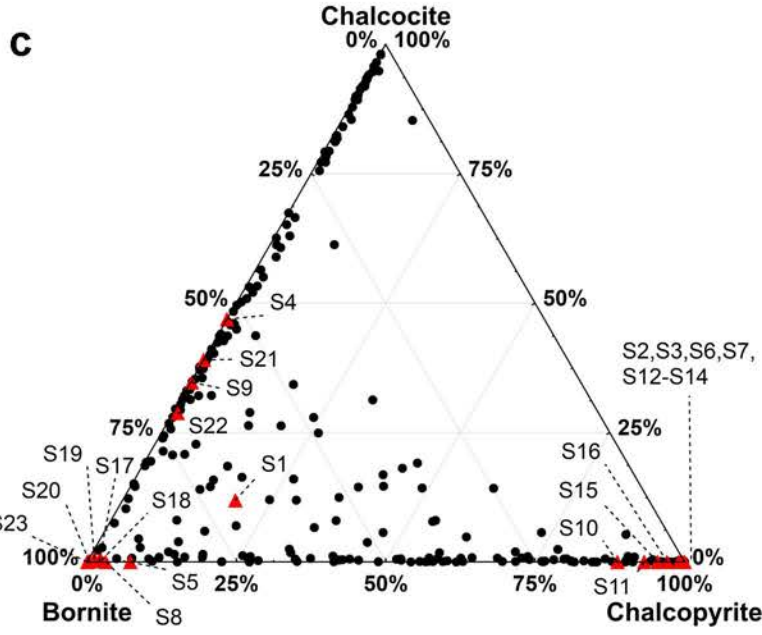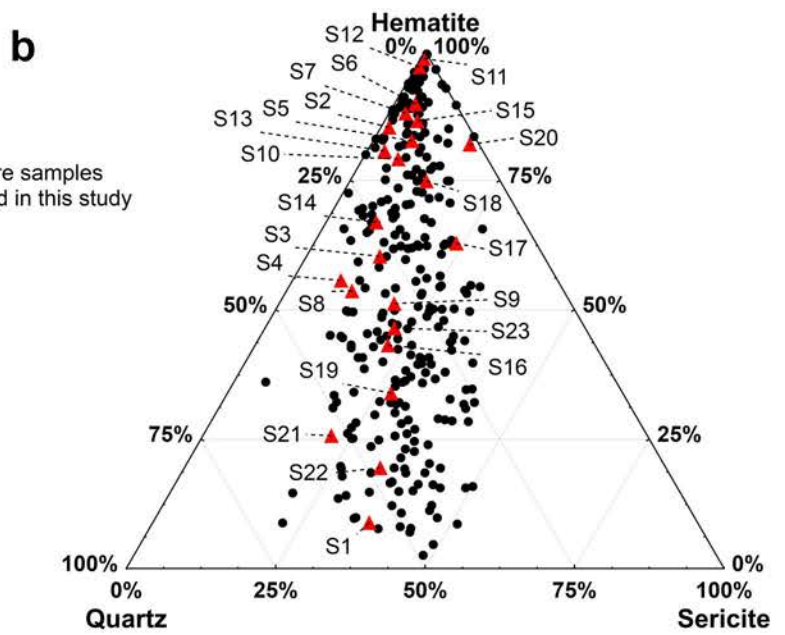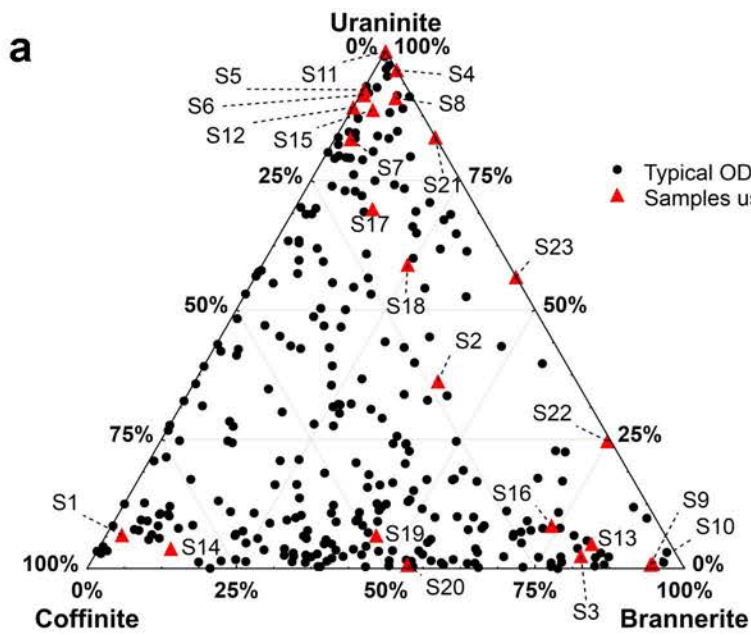1127   in the uraninite for the domain rich in REY-minerals.

1128   Fig. 11: Plot of calculated $U^{6+}/(U^{4+}+U^{6+})$ against charge compensation factor $[= (\,{}^*REY \times$

1129 $4/3) + (M1 \times 4/2) + (Na \times 4/1) - (M2 \times 4/5)]$.

1130   Fig. 12: Box-plots summarizing compositional variability for the different classes of uraninite:

1131   **(a)** UO_2; **(b)** PbO_2; **(c)** total oxide; **(d)** Ce_2O_3; **(e)** Y_2O_3; **(f)** Pb/U. The numbering of the

1132   categories on the x-axis reflects the uraninite classes: 1) primary [N=3]; 2,3) zoned/cob-web

1133   (high-Pb) [N=208]; 2,3) zoned/cob-web (low-Pb) [N=117]; 4) coffinite/uraninite intergrowths

1134   [N=28]; 4) massive [N=221]; and 4) pisoliths [N=4]. Upper box value (UBV) is the 75th

1135   percentile of data, whilst the lower box value (LBV) is the 25th percentile of data. Whiskers

1136   represent <25th percentile and >75th percentile of data. The central tendency is displayed via

1137   the population mean (represented by the dark square). Calculated outliers are: Point

1138   Value>UBV+1.5×(UBV-LBV) or Point Value<LBV-1.5×(UBV-LBV). Calculated extremes

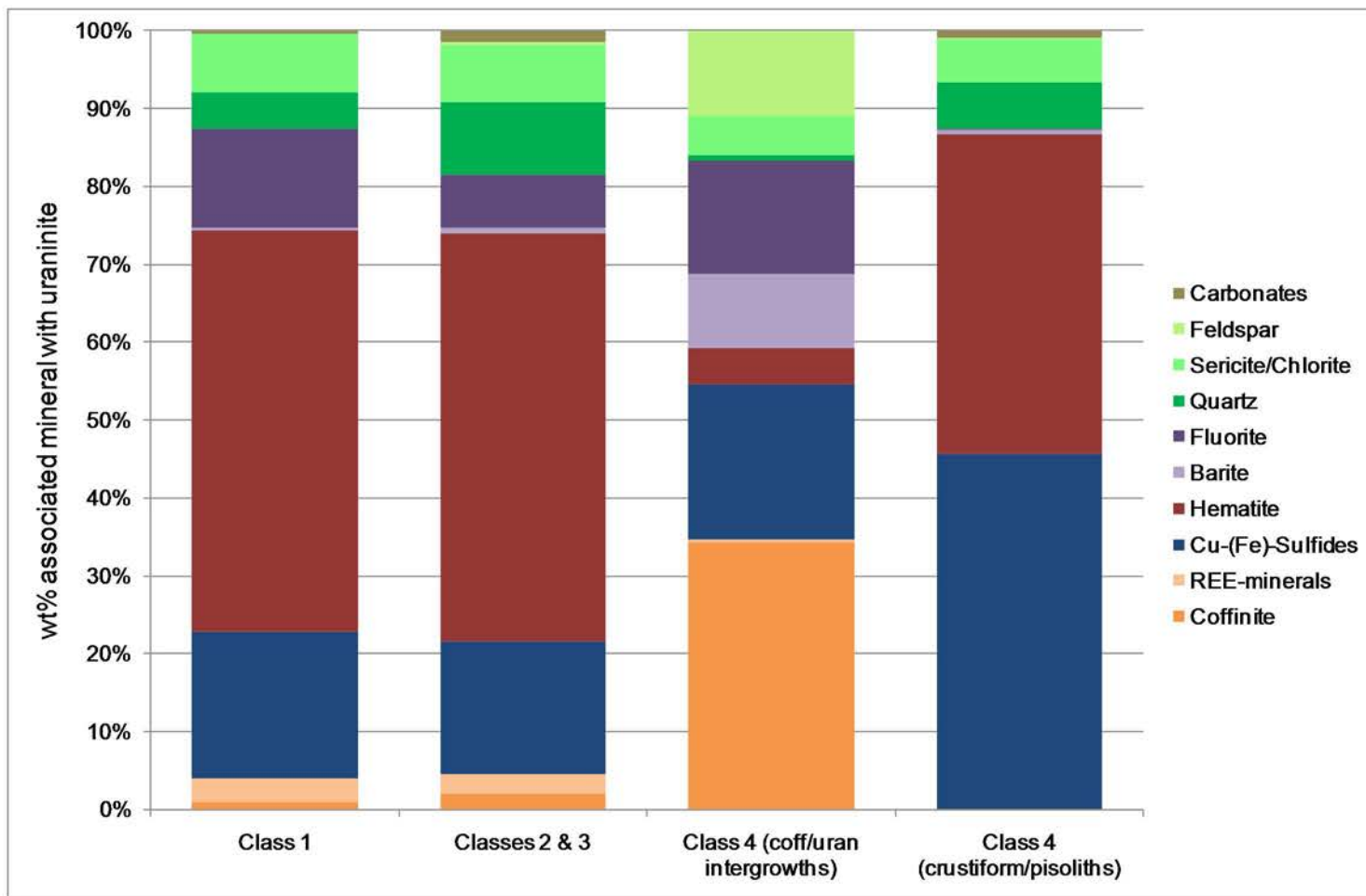1139   are: Point Value>UBV+3×(UBV-LBV) or Point Value<LBV-3×(UBV-LBV).

1140   Fig. 13: Box-plots summarizing compositional variability for the different classes of uraninite:

1141   **(a)** Na_2O; **(b)** MnO; **(c)** CaO; **(d)** AF $(CaO+SiO_2+Fe_2O_3)$; **(e)** Nb_2O_5; **(f)** As_2O_3. Data

1142   displayed and indexed using same convention as Fig. 12.

1143   Fig. 14: Scatter-plots summarizing variation vs. UO_2 wt% for the different classes of uraninite:

1144   **(a)** PbO_2; **(b)** total oxides; **(c)** Ce_2O_3; **(d)** Y_2O_3.
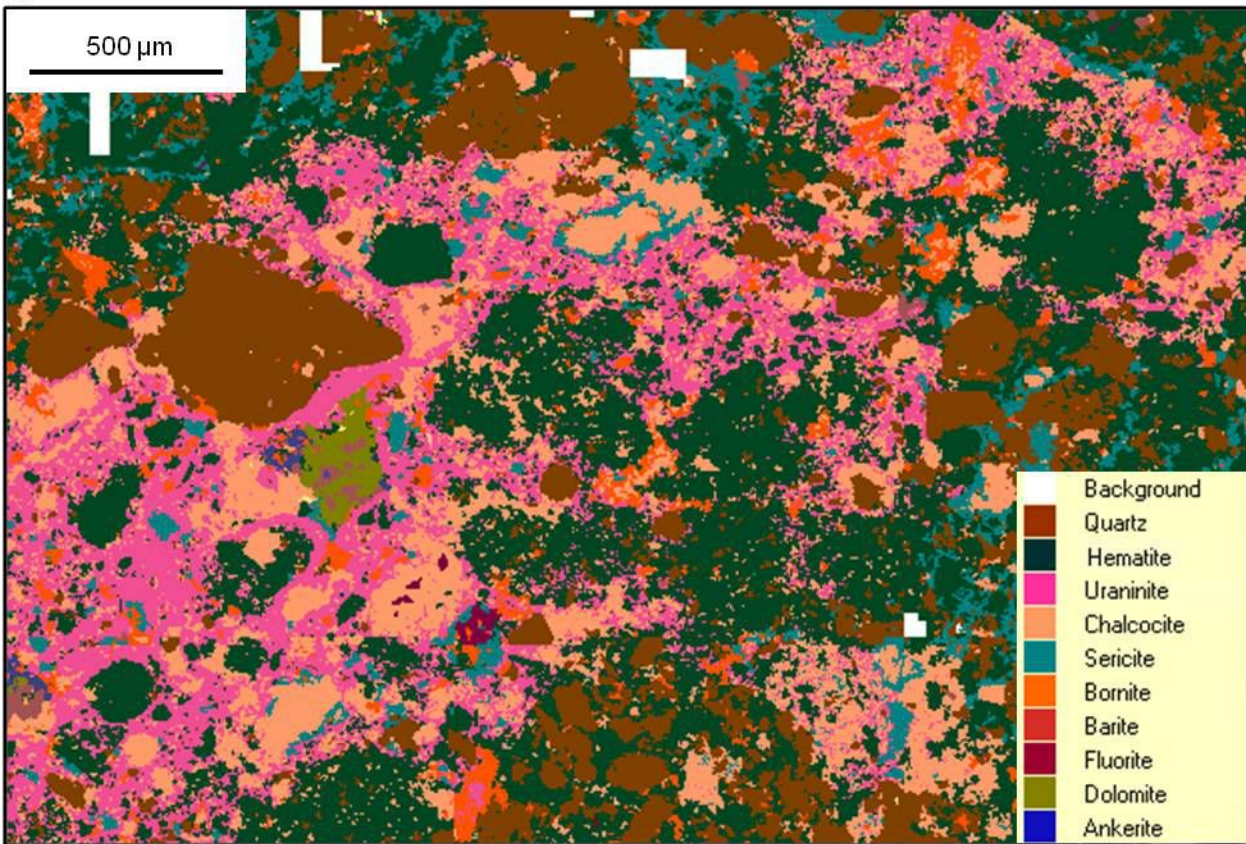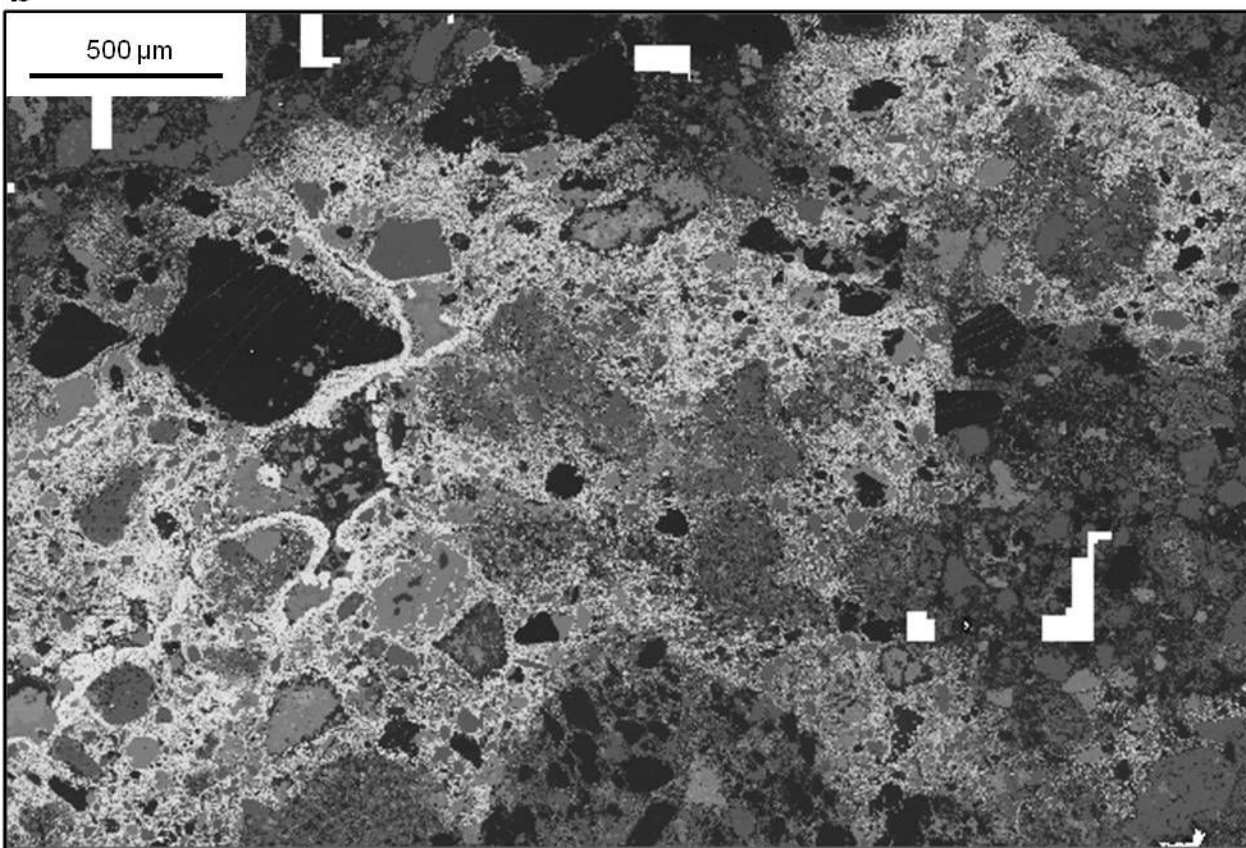
1145   Fig. 15: Scatter-plots summarizing the compositional variability vs. UO_2 wt% for the different

1146   classes of uraninite: **(a)** Na_2O; **(b)** MnO; **(c)** CaO; **(d)** AF $(CaO+SiO_2+Fe_2O_3)$; **(e)** Nb_2O_5; **(f)**
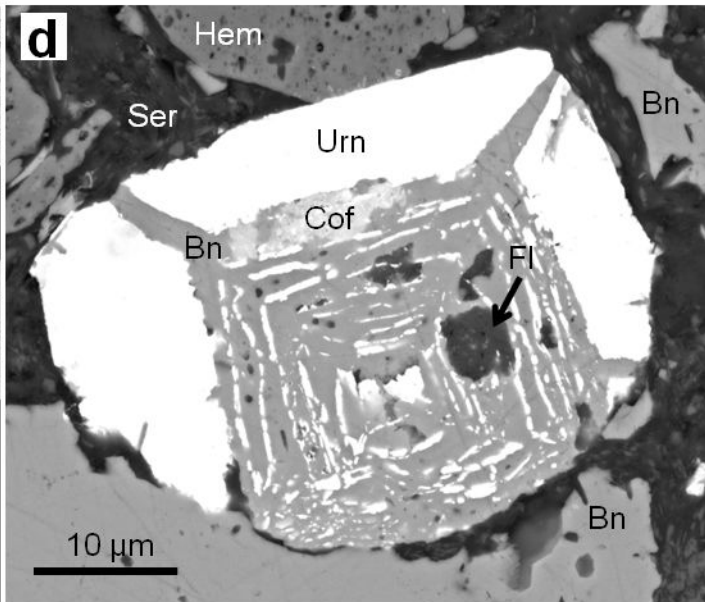
1147   AF $(CaO+SiO_2+Fe_2O_3)$ vs. Pb/U.

Macmillan et al. Fig. 1

Macmillan et al. Fig. 2

a

500 µm

	Background
	Quartz
	Hematite
	Uraninite
	Chalcocite
	Sericite
	Bornite
	Barite
	Fluorite
	Dolomite
	Ankerite

b

500 µm

Macmillan et al. Fig. 3

Macmillan et al. Fig. 4

a Hem, Urn, Qz, Fl, Bn, Ser, Fl, 50 µm

b Urn-(Ca), Urn-(Pb,REY)

c Pb Mα — Relative Concentration: High → Low

d S Kα

e Ce Lα

f Nd Lα
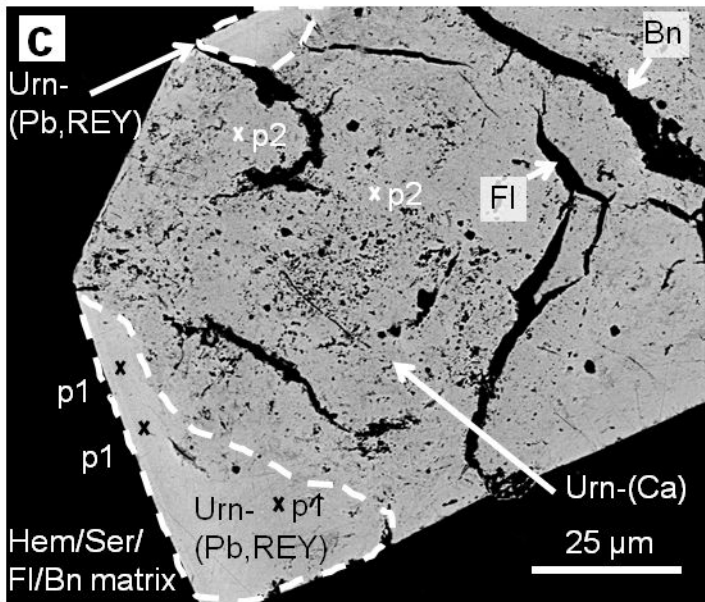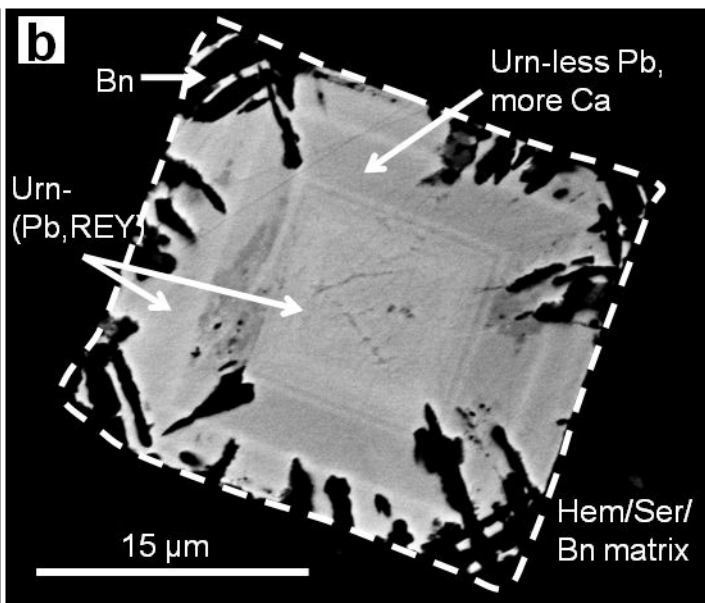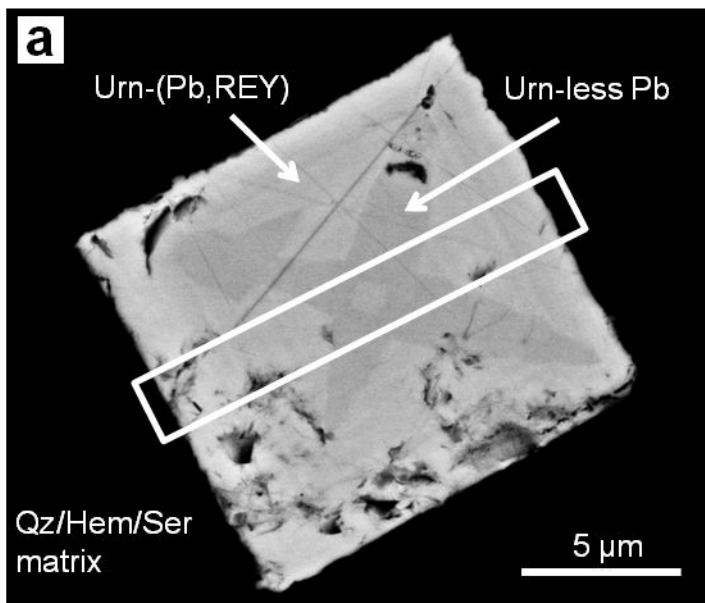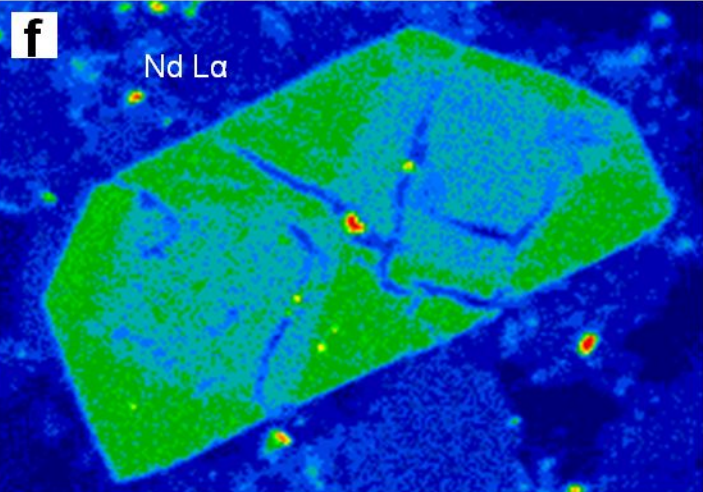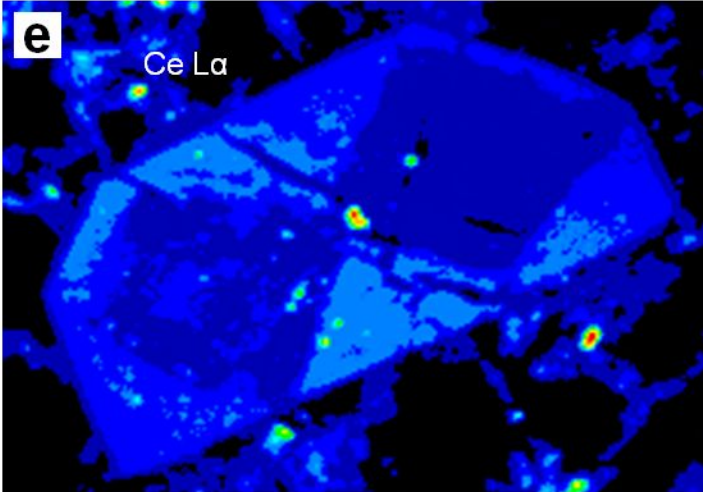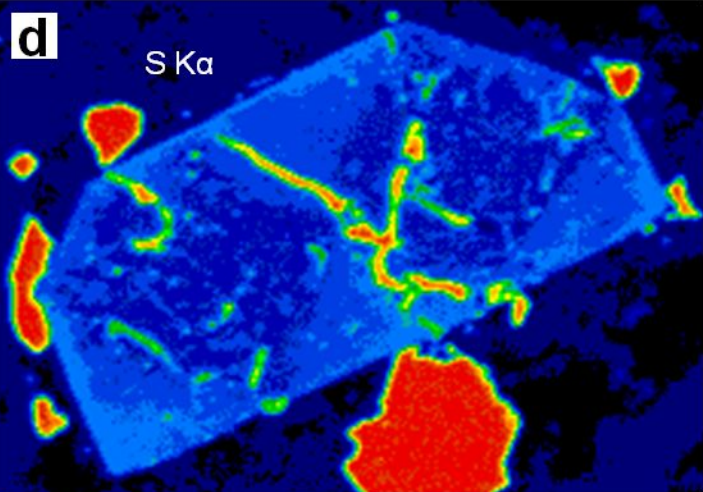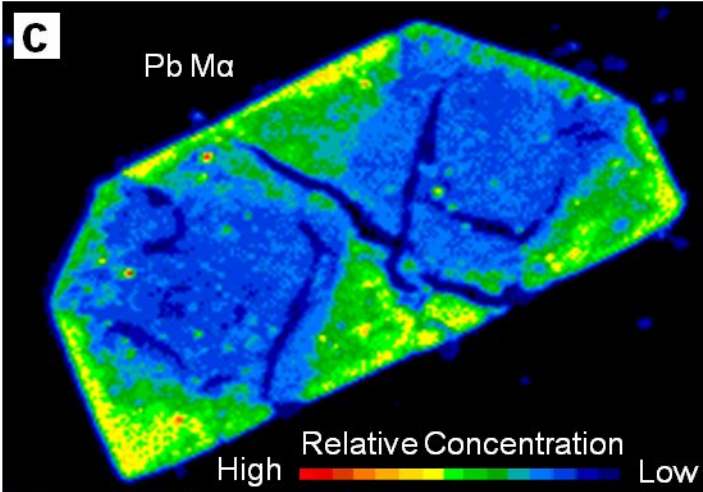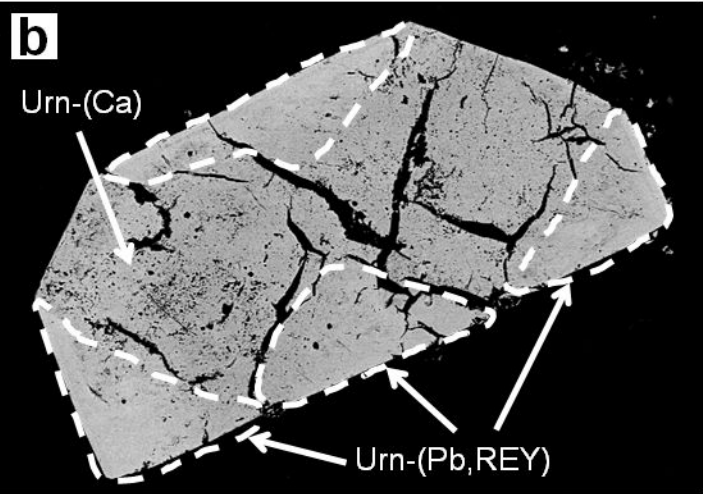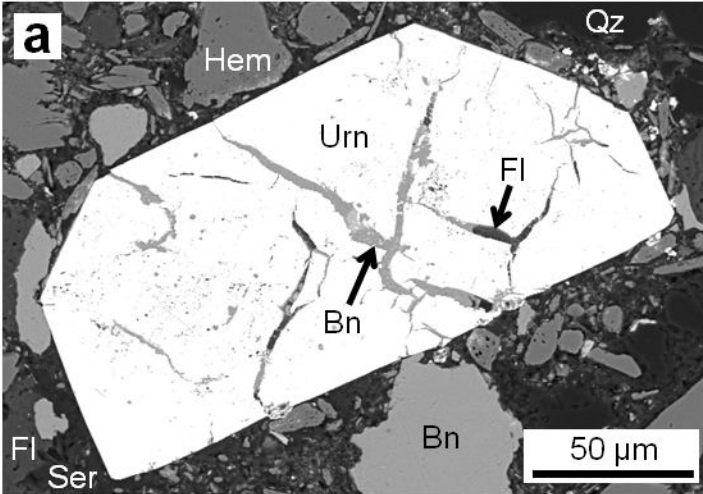
Macmillan et al. Fig. 5
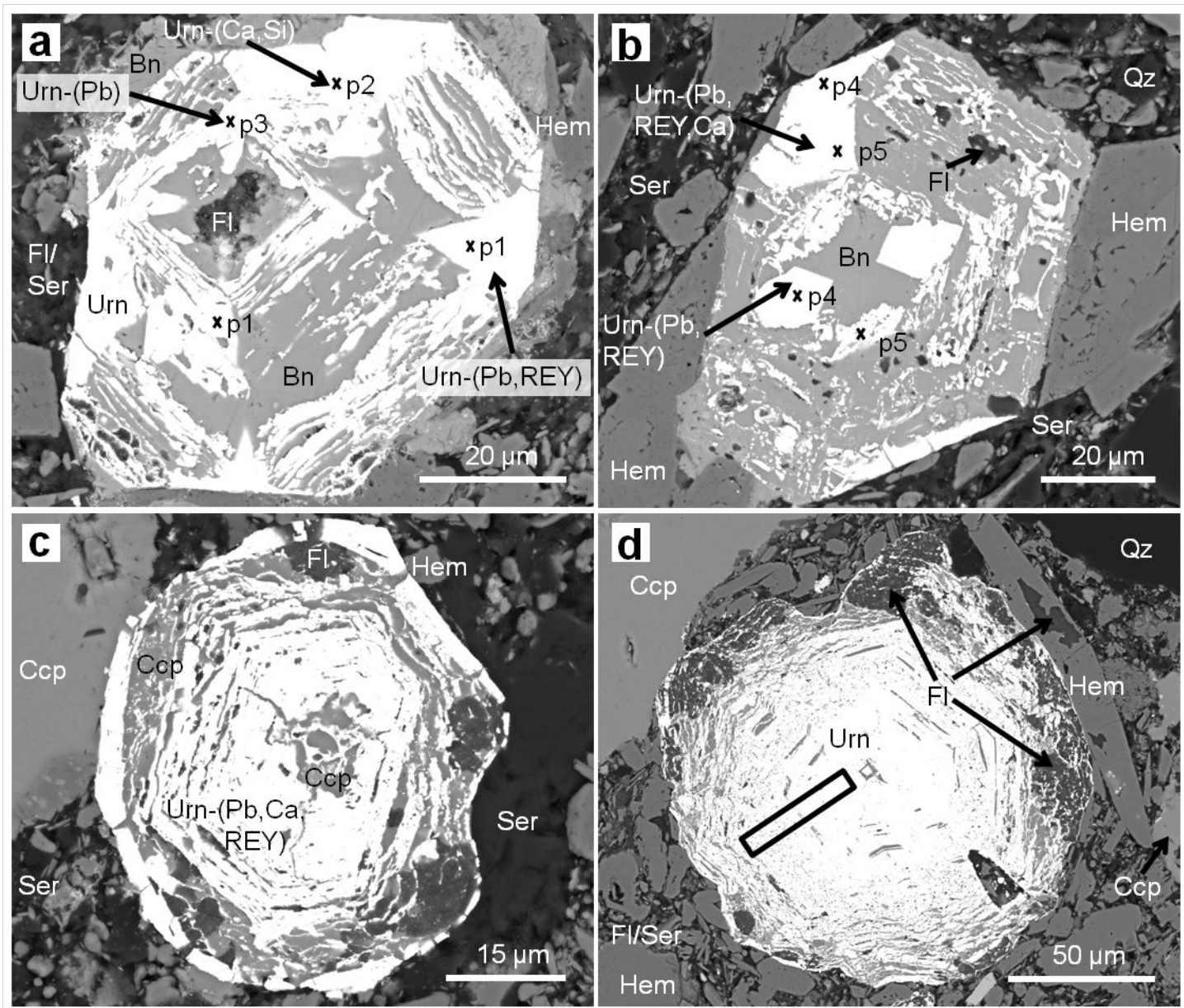
Macmillan et al. Fig. 6

Macmillan et al. Fig. 7

FIB-cut (S15.68; Fig. 4a)

a

4 μm

b

TEM foil (S15.68)

Gn

Ser

zonation

Bn/Cp

Fluor

Hm

Ser

c

b

1 μm

c

SP.1

1 μm

d

Gn

Urn

100 nm

Macmillan et al Fig. 8

(a) domain rich in REE-min incl. — Bn/Cp — FIB-cut (S15.3; Fig. 5d) — 10 µm

(b) domain free of REE-min. incl. — e — SP.3 — d — c — SP.2 — domain rich in REE-min. incl. — Bn/Cp — 1 µm

(c) Mon — Synch — 100 nm

(d) (111)*

(e) (111)*

Macmillan et al Fig. 9
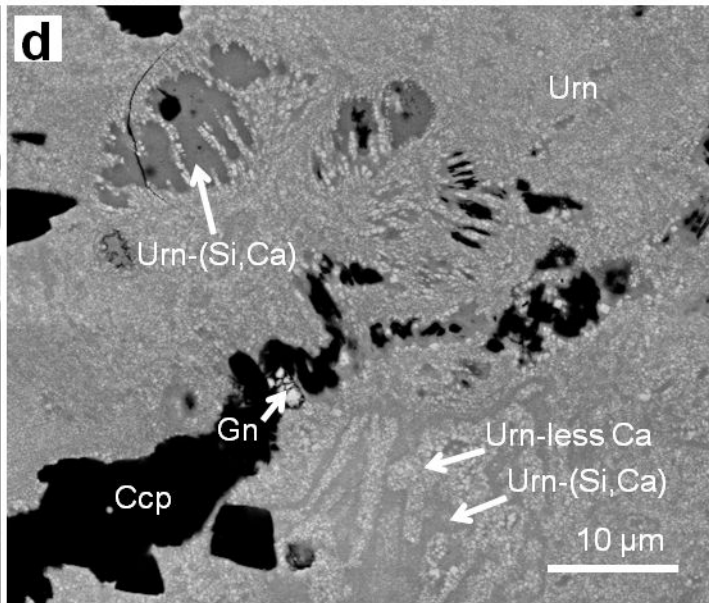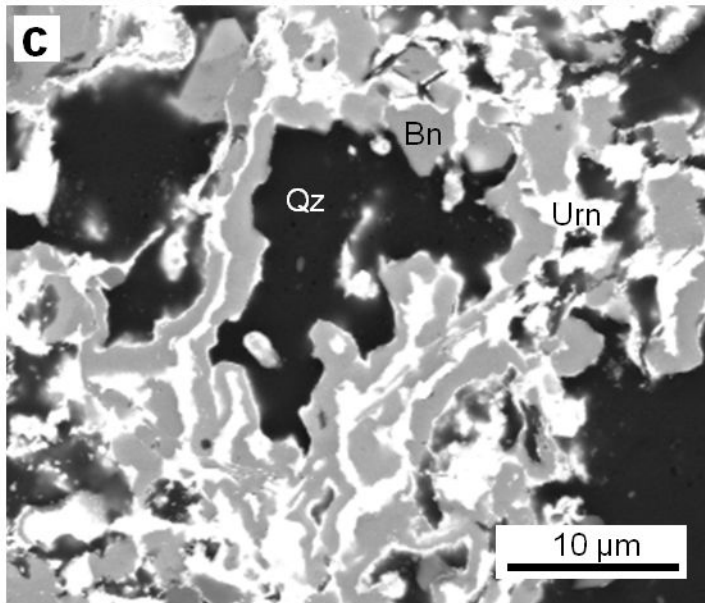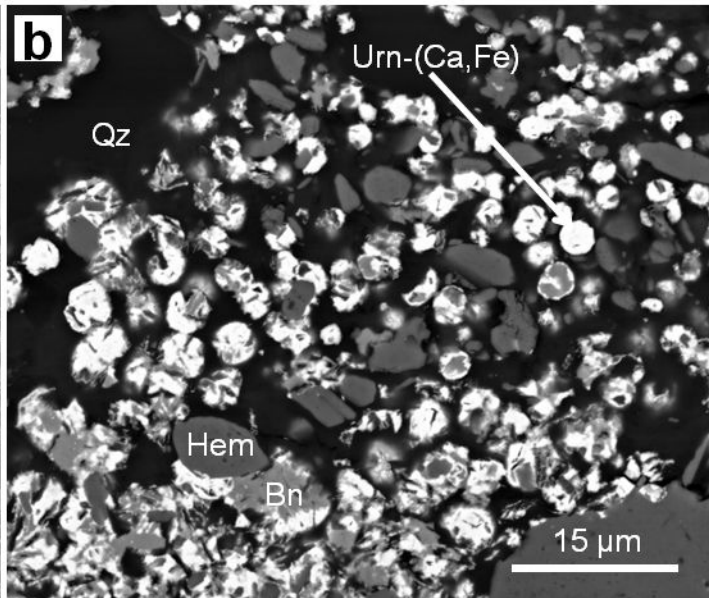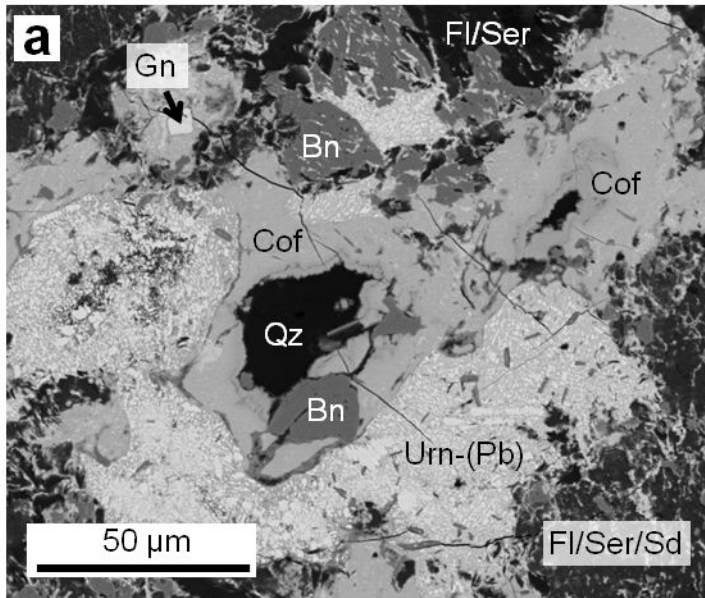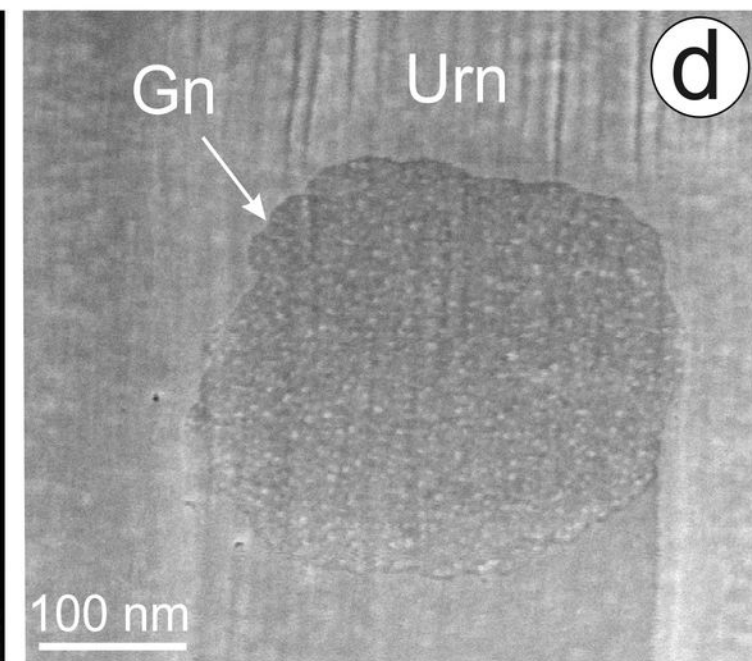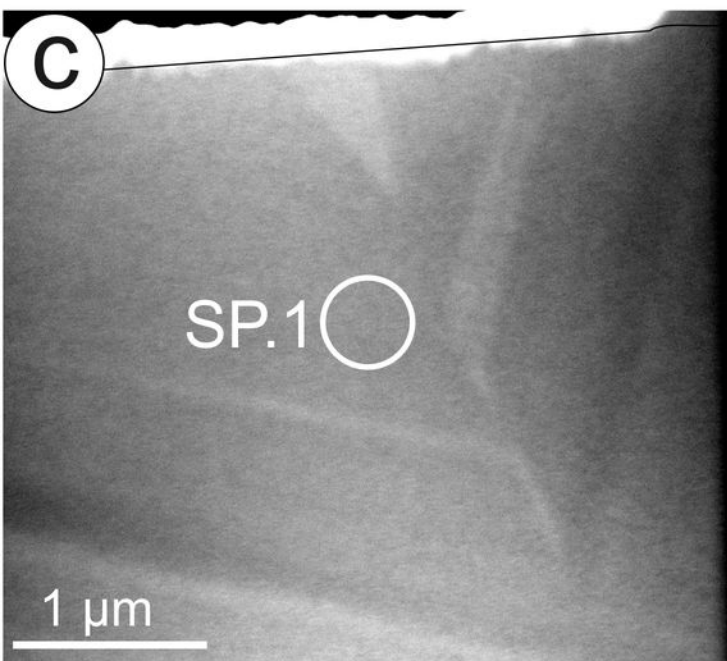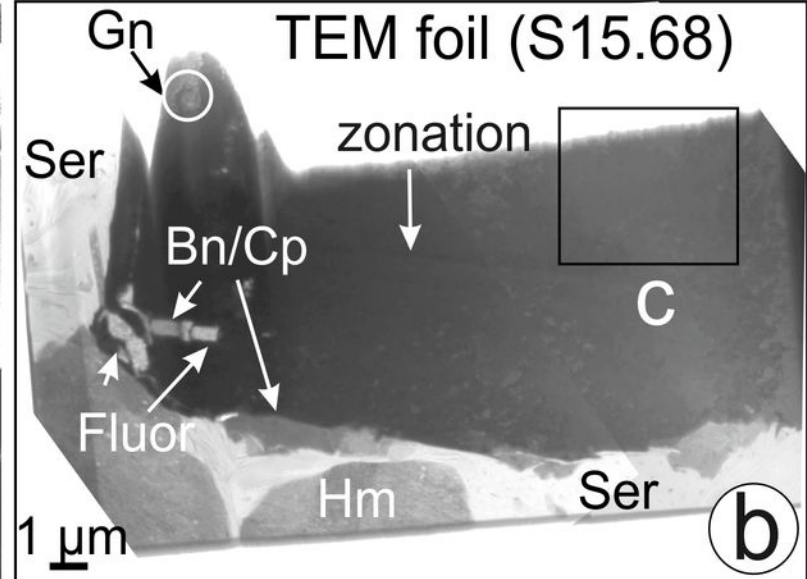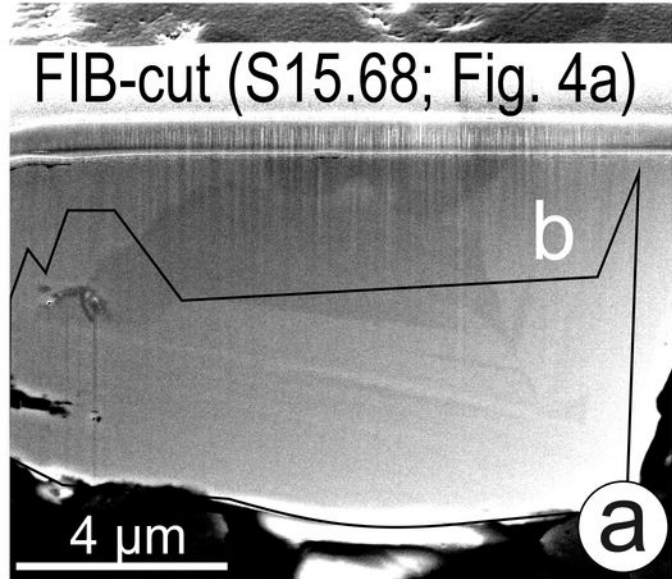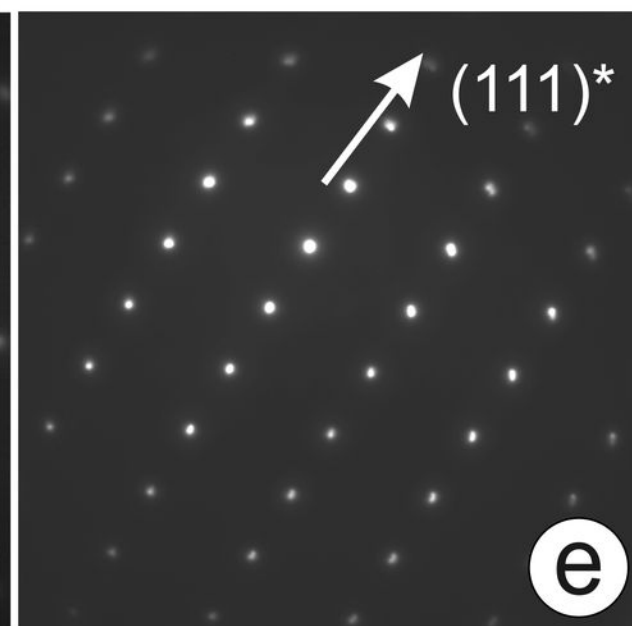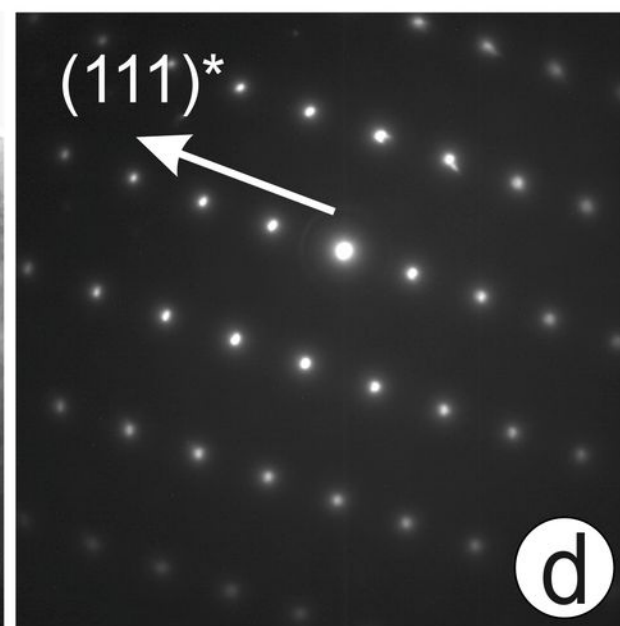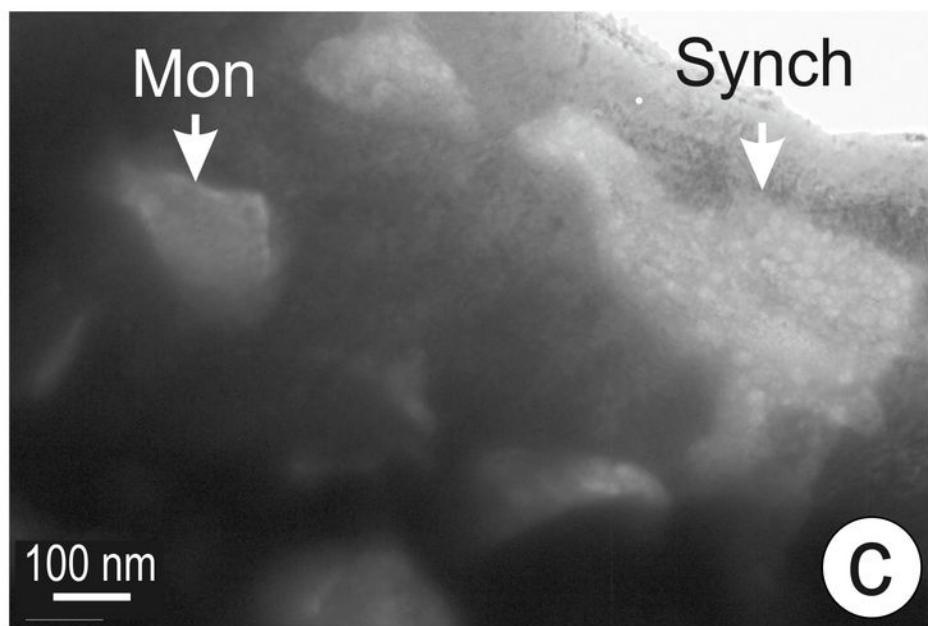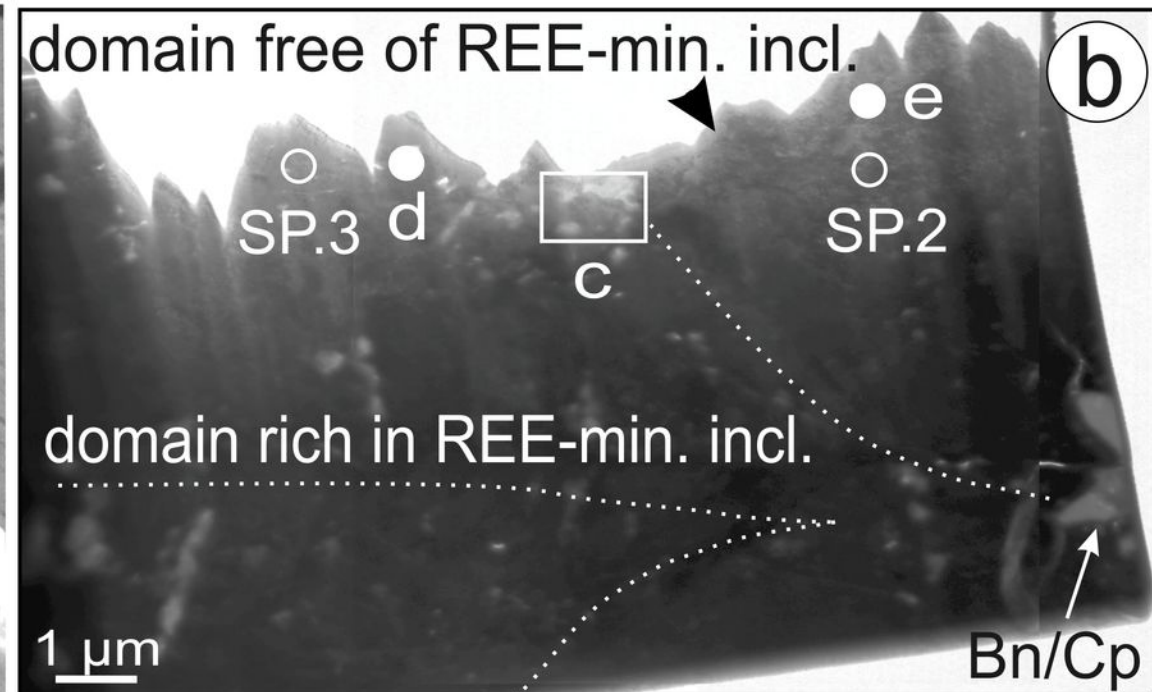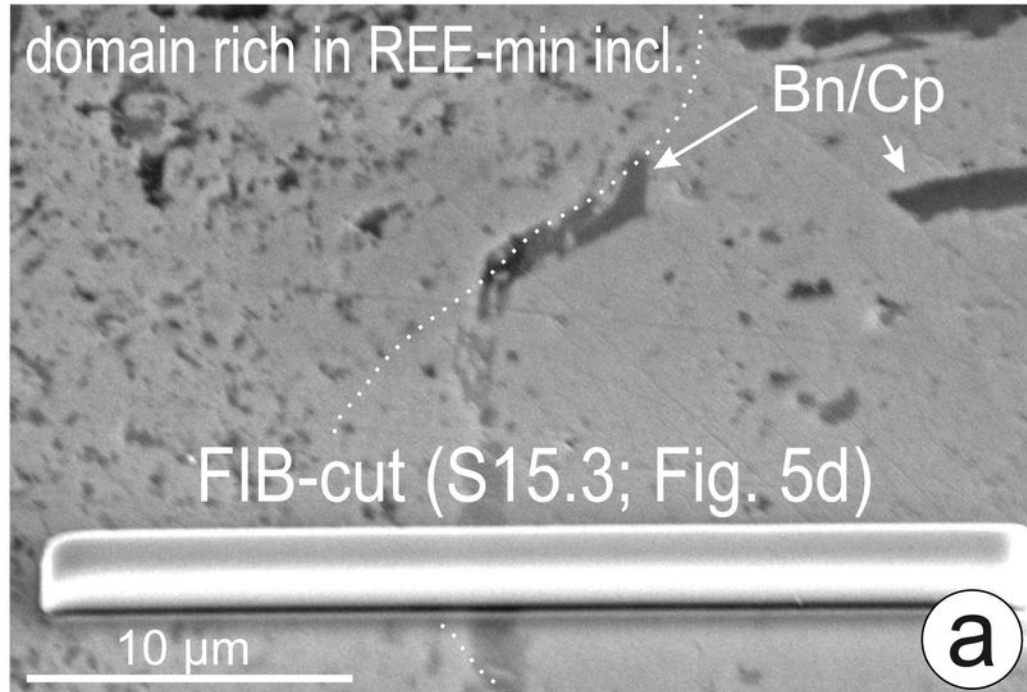
Macmillan et al Fig. 10

Macmillan et al. Fig. 11

Macmillan et al. Fig. 12

Macmillan et al. Fig. 13

Macmillan et al. Fig. 14

Macmillan et al. Fig. 15

Table 1: Sample details (ID, depth, U$_3$O$_8$ grade) with summary of uraninite textures and relative proportions of U-minerals in each sample.

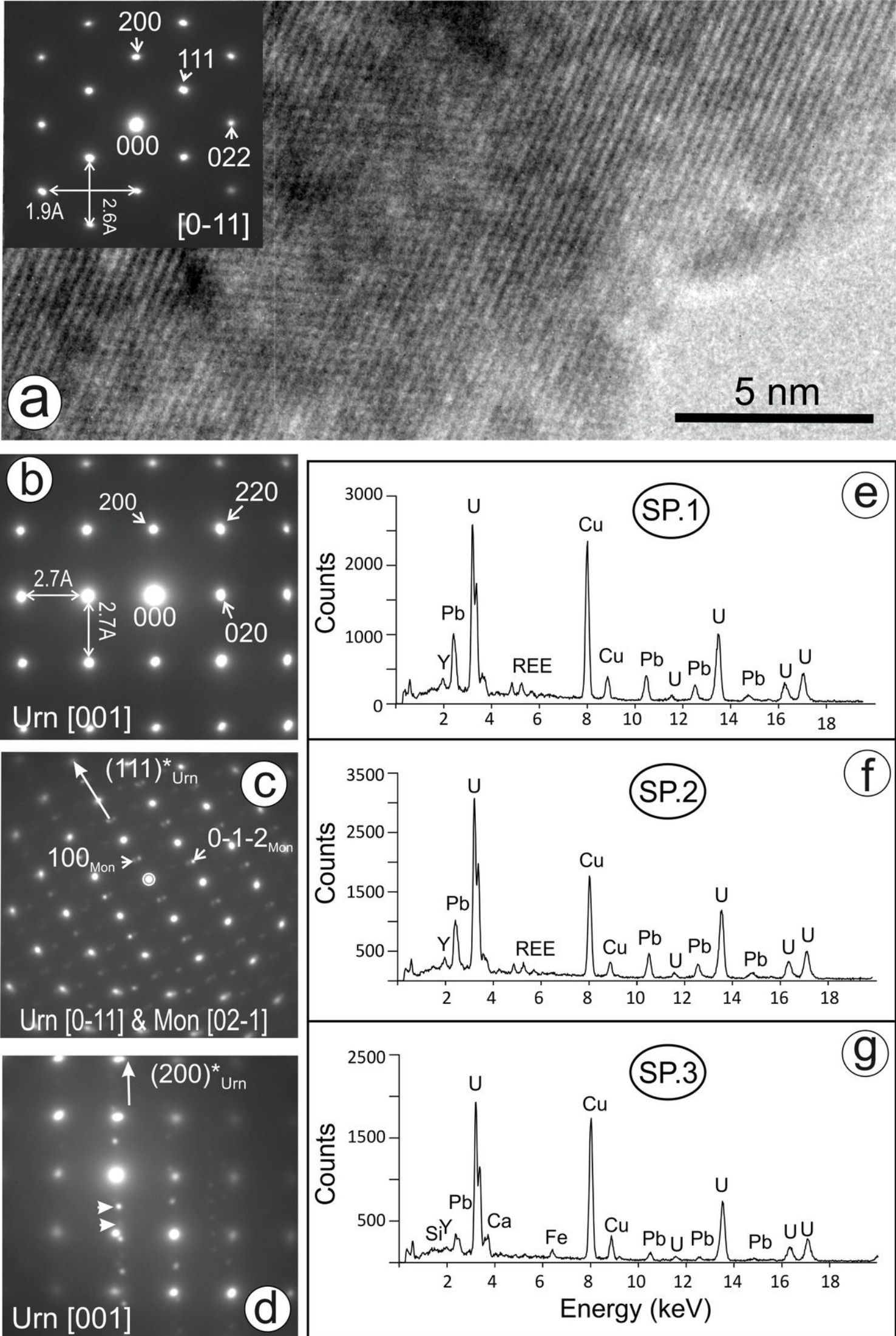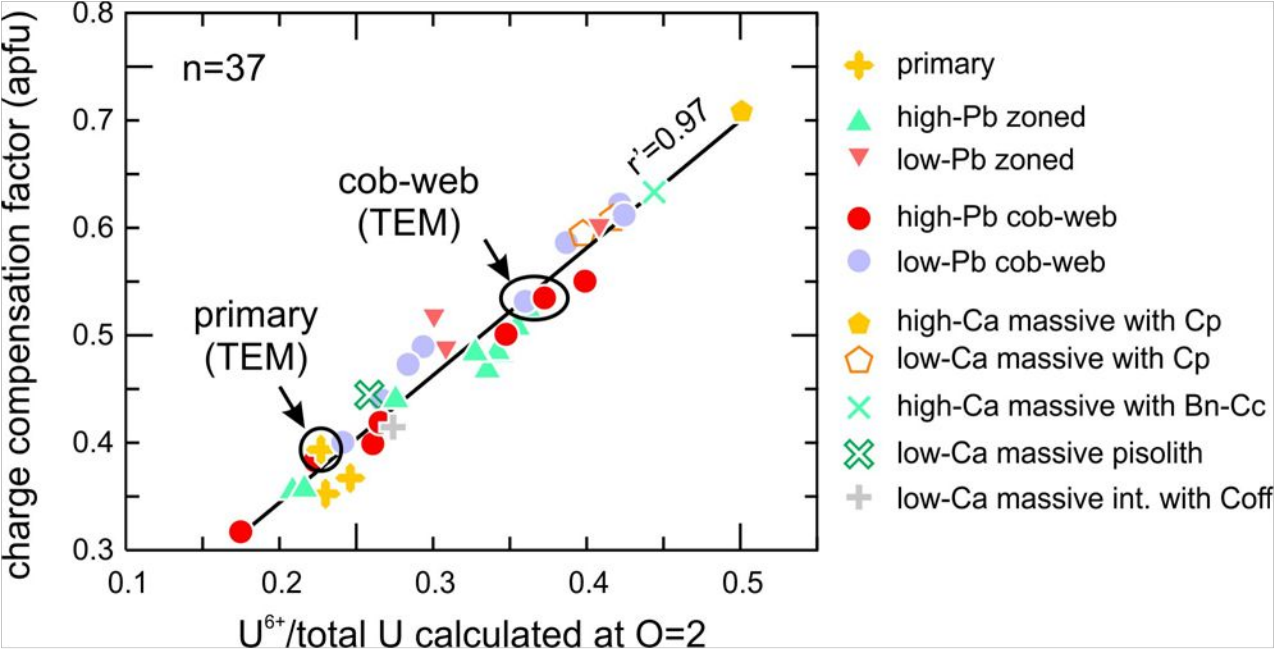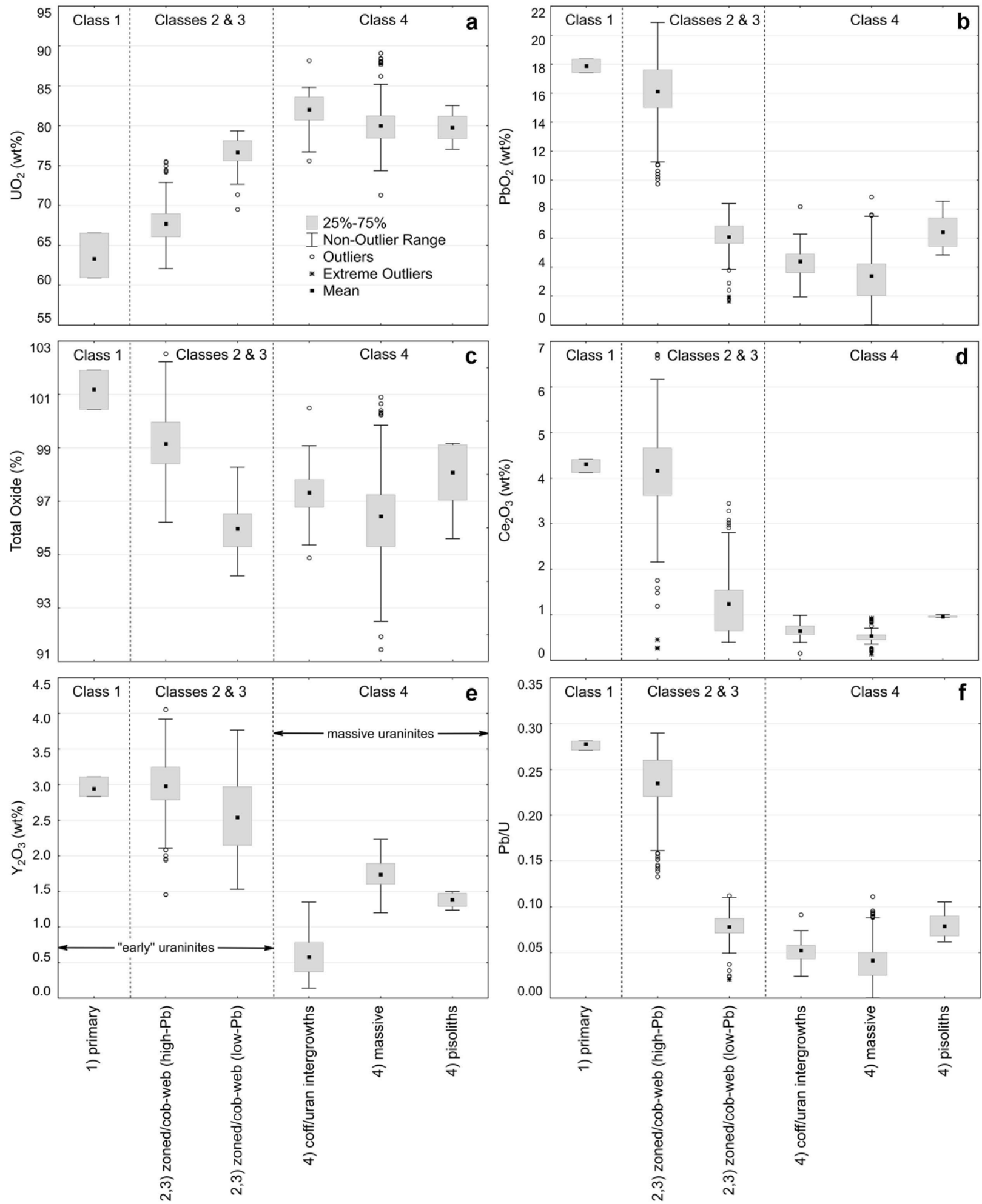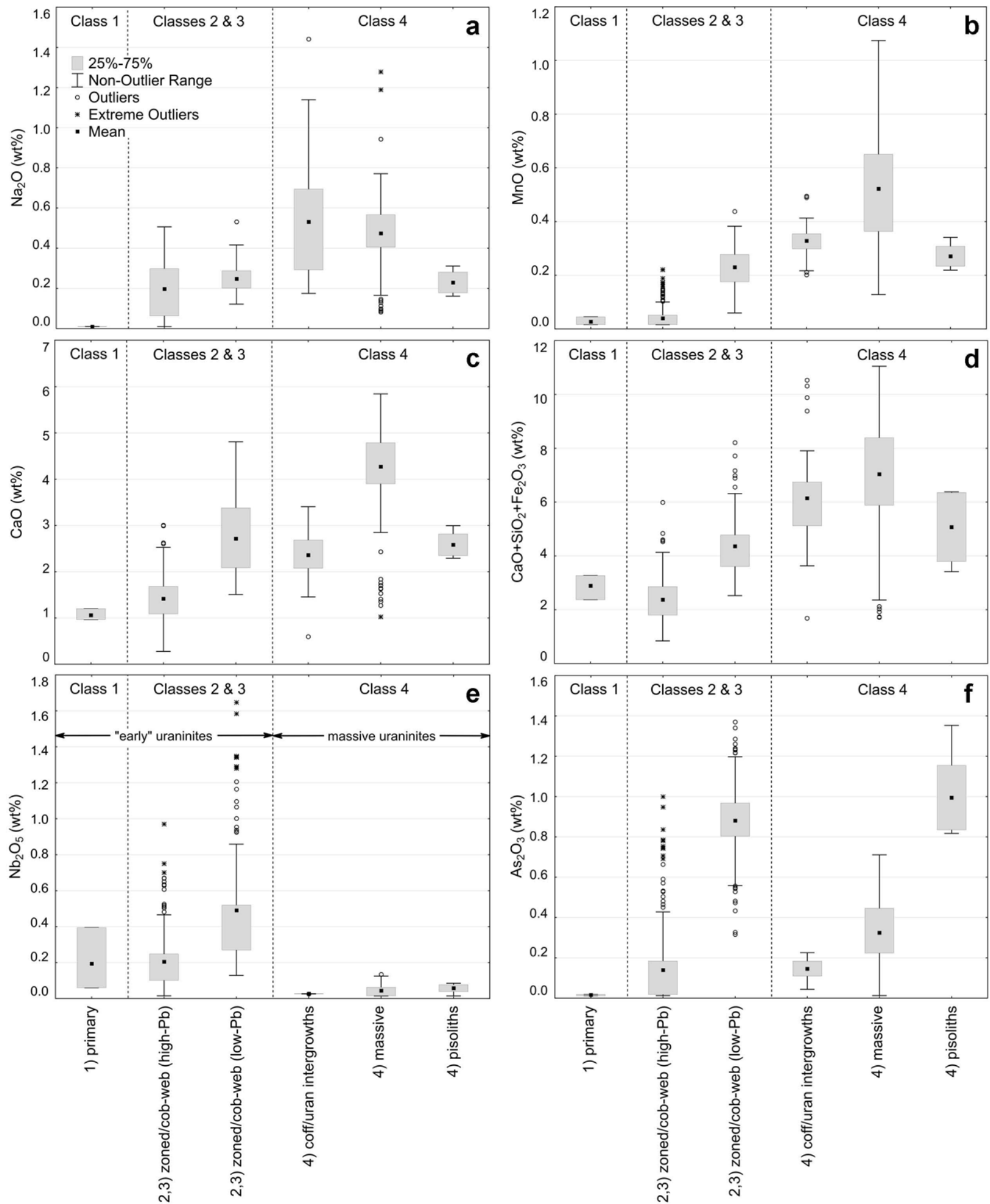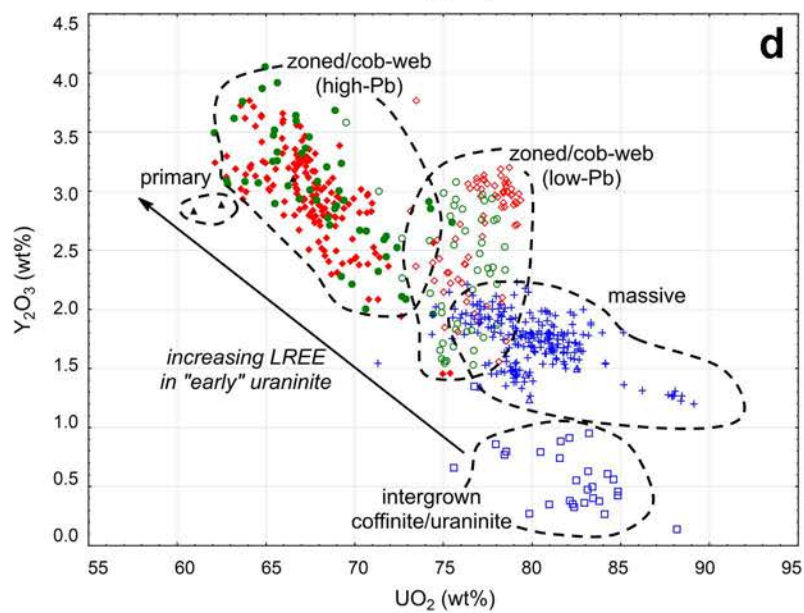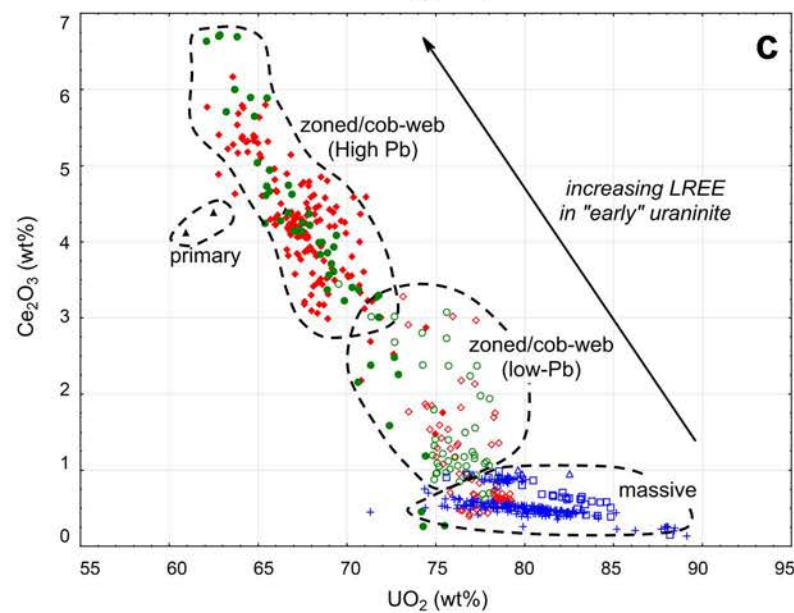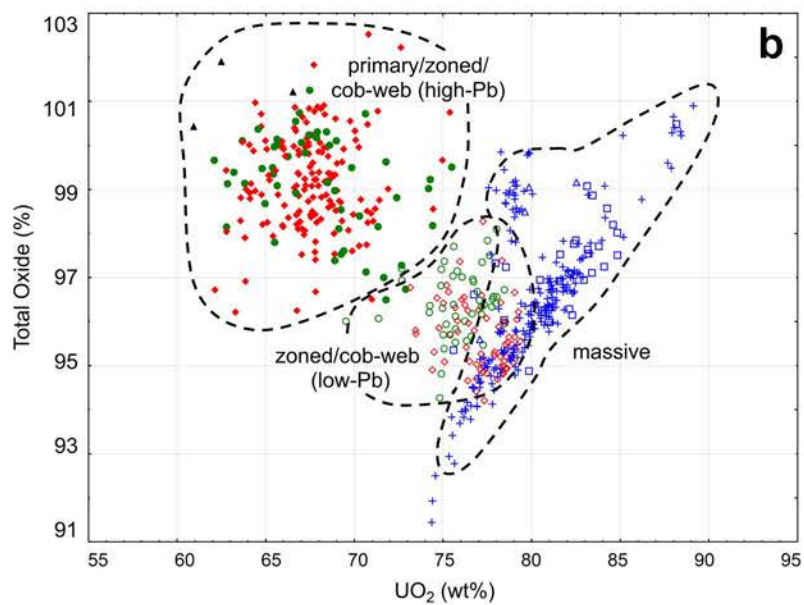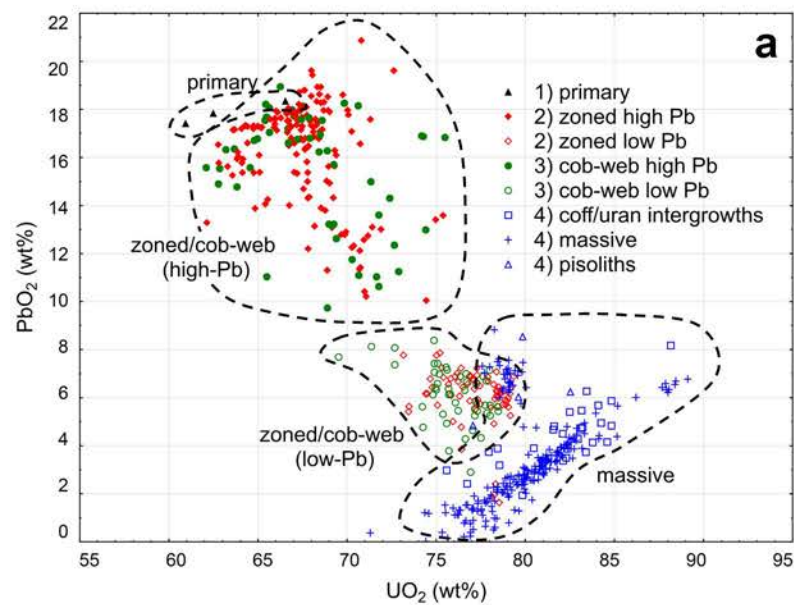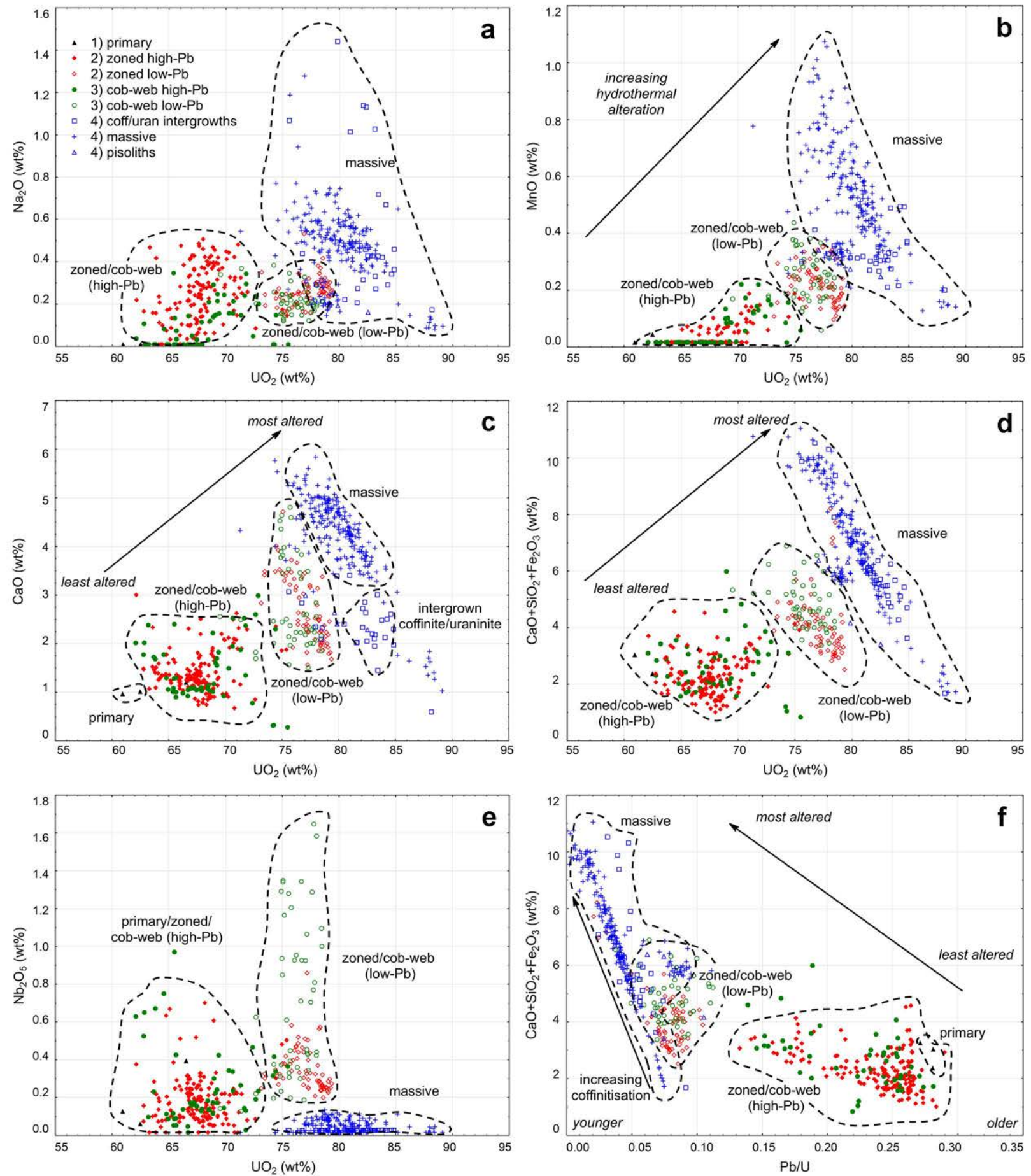| Sample ID	Sample No.	Hole ID	Depth (m)	U$_3$O$_8$ Grade (ppm)	Uraninite	Coffinite	Brannerite	Breccia Type[b]	Uraninite Texture Type
S1 [c,e]	RX7253	RD1303	471.9	21326	6	91	3	GRNH	Massive (coff/uran intergrowths & stringer/anastomozing intergrown with bornite and sericite)
S2 [c]	RX7254	RD1304	890.1	781	36	23	41	HEMH	Zoned (<10 μm in size, rims partially dissolved), fine grained "dusting" of U-minerals (in hematite or chalcopyrite)
S3	RX7255	RD1305	691.0	364	2	16	82	GRNL	Fine grained "dusting" of U-minerals (in hematite, associated coffinite and carbonates)
S4 [c,e]	RX7256	RD1988	880.8	6914	96	0	4	HEMH	Massive (pisoliths and crustiform forming cement inbetween hematite and bornite/chalcocite)
S5 [c]	RX7257	RD1988	1618.9	597	93	7	0	HEM	Zoned and cob-web (associated with bornite), very altered with Si/Ca/Fe rich inclusions
S6 [c]	RX7258	RD1988	1768.8	408	91	8	1	HEM	Zoned and cob-web (associated with chalcopyrite), very altered with Si/Ca/Fe rich inclusions
S7	RX7259	RD1988	1808.9	369	83	14	3	HEM	Fine grained "dusting" of U-minerals (in hematite)
S8	RX7260	RD2080	479.7	1686	91	3	6	GRNL	Massive in vein (crustiform, intergrown with hematite) and fine grained "dusting" of U-minerals in hematite
S9	RX7261	RD3000W1	936.3	387	1	5	94	HEMH	Fine grained "dusting" of U-minerals (minor)
S10	RX7262	RD3000W1	948.2	382	1	5	94	HEMH	Fine grained "dusting" of U-minerals (minor)
S11 [c,d,e]	RX7263	RD3002	470.9	145840	100	0	0	HEM	Massive (crustiform/anastomozing intergrown with chalcopyrite, hematite)
S12	RX7264	RD3002	472.4	119	89	11	0	HEM	Fine grained "dusting" of U-minerals (in hematite)
S13	RX7265	RD3022	921.6	2244	5	13	82	HEM	Fine grained "dusting" of U-minerals (minor)
S14	RX7266	RD3022	968.2	731	4	84	12	HEM	Fine grained "dusting" of U-minerals (in hematite and chalcopyrite)
S15 [c,e]	RX7267	RD3035	675.5	1293	89	8	3	HEMH	Primary, zoned and advanced cob-web (associated with chalcopyrite); cob-web types display more rounding and rhythmic intergrowths
S16	RX7268	RD3035	876.8	638	8	18	74	HEM	Fine grained "dusting" of U-minerals (in hematite, chalcopyrite, quartz and carbonates)
S17 [c,e]	RX7269	RD3035	970.5	1605	70	17	13	HEMF	Primary, zoned and cob-web (associated with bornite); best example of zoned with chemical zonation (Fig. 5); many cob-web types have bn/hem selvedges
S18 [c,e]	RX7270	RD3307	1092.8	1153	59	17	24	HEM	Zoned and intense cob-web (associated with bornite); best examples of twinning and sectorially zoned cob-web types; some coffinite growth on rims of cob-web types
S19 [c]	RX7272	RD3554	494.4	425	6	49	45	GRNH	Zoned and cob-web (partially dissolved/altered, associated with bornite) and fine grained
S20	RX7273	RD3554	498.2	139	1	46	53	GRNH	Fine grained "dusting" of U-minerals (minor) in hematite and bornite
S21 [c,e]	RX7274	RD3560	716.3	11259	83	0	17	GRNL	Massive (crustiform and pisoliths; associated with bornite, hematite ± sericite ± quartz ± siderite)
S22	RX7275	RD3560	719.6	494	24	1	75	GRNL	Fine grained "dusting" of U-minerals (minor) in hematite and quartz
S23 [c]	RX7276	RD3560	726.7	408	56	0	44	GRNL	Zoned (<10 μm in size) and fine grained "dusting" of U-minerals in hematite ± sericite ± quartz

a) Relative proportions of coffinite/brannerite/uraninite as determined from MLA sparse phase liberation mapping (SPL_Lite) data.

b) Breccia types: GRNH = Roxby Downs Granite (RDG; 90-70%) with some hematite (10-30%) breccia, matrix contains hematised sericite, quartz; GRNL = RDG (70-40%) with hematite (30-60%) breccia, granitic clasts with hematite rich matrix; HEMH = Hematite (60-90%) with RDG (40-10%) breccia, hematitic rich matrix supported breccia with hematitic clasts; HEM = Hematite (>90%) with RDG (<10%) breccia, hematitic rich matrix and clasts with strong hematite alteration; HEMF = Hematite with GRV clasts, often porphyritic with chloritised phenocrysts.

c) MLA Data for minerals found in association with uraninite (Table A4) used as input for Fig. 2.

d) MLA SPL_Lite false-colour mineral map (Fig. 3) of this sample.

e) EPMA data for these samples collated in Tables 2-5 and A6-A10 (7 samples).

Table 2: Electron probe microanalytical data for selected primary uraninites.

Sample no.	S17.11a	S17.11b	S15.68
Valid N (analyses)	1 (Fig. 4b)	1 (Fig. 4b)	1 (Fig. 4a)
(wt%)			
UO_2	62.48	60.93	66.53
PbO_2	17.84	17.42	18.35
ThO_2	7.41	7.42	<mdl
Na_2O	<mdl	<mdl	<mdl
SiO_2	0.06	0.56	0.13
P_2O_5	<mdl	<mdl	<mdl
SO_3	<mdl	<mdl	<mdl
CaO	1.01	0.97	1.2
TiO_2	<mdl	0.04	<mdl
MnO	0.04	<mdl	<mdl
Fe_2O_3	1.3	1.51	1.93
Cu_2O	0.11	0.09	0.1
As_2O_3	<mdl	<mdl	<mdl
ZrO_2	0.05	0.05	0.07
Nb_2O_5	0.06	0.13	0.39
Y_2O_3	2.89	2.83	3.11
Ce_2O_3	4.39	4.12	4.41
La_2O_3	0.55	0.53	0.51
Pr_2O_3	0.47	0.45	0.53
Nd_2O_3	2.27	2.3	2.75
Sm_2O_3	0.38	0.49	0.52
Gd_2O_3	0.54	0.54	0.61
Total Oxide	101.91	100.43	101.22
SiO_2+CaO+Fe_2O_3	2.38	3.04	3.27
Pb/U	0.28	0.28	0.27

Uraninite Formula (apfu) - based on 2 O			
U^{4+}	0.566	0.552	0.603
Pb^{4+}	0.196	0.191	0.201
Th^{4+}	0.069	0.069	0.000
Na^+	0.000	0.000	0.000
Si^{4+}	0.002	0.023	0.005
Ca^{2+}	0.044	0.042	0.052
Ti^{4+}	0.000	0.001	0.000
Mn^{2+}	0.001	0.000	0.000
As^{5+}	0.000	0.000	0.000
Zr^{4+}	0.001	0.001	0.001
Nb^{5+}	0.001	0.002	0.007
Y^{3+}	0.063	0.061	0.067
Ce^{3+}	0.065	0.061	0.066
La^{3+}	0.008	0.008	0.008
Pr^{3+}	0.007	0.007	0.008
Nd^{3+}	0.033	0.033	0.040
Sm^{3+}	0.005	0.007	0.007
Gd^{3+}	0.007	0.007	0.008
Total	1.070	1.067	1.076
ΣREY	0.189	0.185	0.204

Note: Sample ID is of the form: "SXX.xx" where "SXX" = sample ID as represented in Table 1, "xx" = grain number analysed
Cu_2O, Fe_2O_3, SO_3, P_2O_5 have been assumed to be inclusion bound, so removed from apfu calculations
As_2O_3 has been used for oxide determination, but has been converted to As^{5+} within the apfu calculations

Table 3: Electron probe microanalytical data for selected zoned uraninites.

Sample no.	S17.12 [a]	S17.12 [b]	S17.28 [a]	S17.36 [a]	S17.47 [a]	S17.52 [a]	S17.61 [a]	S17.63 [a]	S18.29 [b]	S18.2 [b]	S18.29 [a]	S18.29 [a]
Valid N (analyses)	41 (Fig. 4c)	20 (Fig. 4c)	10	4	14	23	7	14	9	39	1	1
(wt%)	Mean (p1)	Mean (p2)	Mean	Mean	Mean	Mean	Mean	Mean	Mean	Mean		
UO_2	69.75	75.46	66.46	65.18	68.23	66.22	67.11	66.47	77.39	78.13	74.97	75.38
PbO_2	14.85	6.72	17.24	16.96	17.18	16.52	17.57	17.43	3.64	6.25	13.41	13.58
ThO_2	<mdl	0.06	0.13	0.30	0.37	0.10	0.79	0.87	<mdl	0.05	<mdl	<mdl
Na_2O	0.32	0.21	0.20	0.11	0.35	0.22	0.24	0.18	0.32	0.28	0.17	0.15
SiO_2	0.21	0.30	0.14	0.09	0.16	0.14	0.23	0.11	1.30	0.50	0.83	0.71
P_2O_5	<mdl	0.02	<mdl	<mdl	<mdl	<mdl	<mdl	<mdl	0.09	0.04	0.10	0.07
SO_3	0.03	0.12	<mdl	<mdl	<mdl	<mdl	0.02	<mdl	<mdl	<mdl	<mdl	<mdl
CaO	1.59	3.42	1.20	1.26	1.23	1.36	1.10	1.25	2.44	2.24	1.86	1.88
TiO_2	<mdl	0.04	<mdl	<mdl	<mdl	<mdl	<mdl	<mdl	0.08	0.08	0.03	0.05
MnO	0.06	0.25	<mdl	<mdl	<mdl	<mdl	<mdl	<mdl	0.25	0.19	0.19	0.17
Fe_2O_3	0.54	0.63	0.32	0.43	0.71	0.66	1.34	0.40	2.04	0.73	1.33	1.45
Cu_2O	0.14	0.16	0.22	0.73	0.25	0.25	0.33	0.15	0.45	0.11	0.55	0.75
As_2O_3	0.30	1.12	0.07	<mdl	0.05	0.05	<mdl	0.07	0.68	0.87	0.35	0.30
ZrO_2	0.06	0.06	0.05	0.05	0.06	0.06	0.06	0.05	0.08	0.08	0.04	0.08
Nb_2O_5	0.16	0.39	0.19	0.20	0.15	0.24	0.15	0.17	0.50	0.28	0.48	0.50
Y_2O_3	2.66	2.27	3.19	3.35	2.88	3.28	3.02	3.17	2.24	2.99	1.45	1.46
Ce_2O_3	4.01	1.48	4.43	5.11	3.56	4.51	3.87	4.12	2.03	0.59	1.48	1.76
La_2O_3	0.47	0.25	0.55	0.61	0.46	0.56	0.48	0.51	0.28	0.19	0.32	0.36
Pr_2O_3	0.49	0.31	0.54	0.63	0.45	0.59	0.47	0.51	0.33	0.10	0.17	0.23
Nd_2O_3	2.39	1.66	2.67	2.82	2.15	2.77	2.22	2.52	1.60	0.62	1.12	1.34
Sm_2O_3	0.48	0.55	0.52	0.55	0.44	0.55	0.45	0.51	0.42	0.25	0.38	0.36
Gd_2O_3	0.48	0.60	0.57	0.63	0.49	0.58	0.57	0.56	0.49	0.61	0.30	0.26
Total Oxide	99.03	96.10	98.74	99.07	99.22	98.70	100.08	99.10	96.68	95.21	99.66	100.75
$SiO_2+CaO+Fe_2O_3$	2.34	4.35	1.66	1.77	2.10	2.16	2.66	1.76	5.78	3.48	3.92	4.13
Pb/U	0.21	0.09	0.26	0.26	0.25	0.25	0.26	0.26	0.05	0.08	0.18	0.18

Uraninite Formula (apfu) - based on 2 O

U^{4+}	0.636	0.691	0.609	0.599	0.627	0.607	0.615	0.608	0.710	0.732	0.682	0.681
Pb^{4+}	0.164	0.074	0.191	0.188	0.191	0.183	0.195	0.193	0.040	0.071	0.148	0.148
Th^{4+}	0.000	0.001	0.001	0.003	0.004	0.001	0.007	0.008	0.000	0.000	0.000	0.000
Na^{+}	0.025	0.017	0.016	0.009	0.028	0.017	0.019	0.015	0.026	0.023	0.014	0.011
Si^{4+}	0.009	0.012	0.006	0.004	0.007	0.006	0.009	0.004	0.054	0.021	0.034	0.029
Ca^{2+}	0.070	0.151	0.053	0.056	0.055	0.060	0.048	0.055	0.108	0.101	0.081	0.082
Ti^{4+}	0.000	0.001	0.000	0.000	0.000	0.000	0.000	0.000	0.002	0.002	0.001	0.001
Mn^{2+}	0.002	0.009	0.000	0.000	0.000	0.000	0.000	0.000	0.009	0.007	0.007	0.006
As^{5+}	0.007	0.028	0.002	0.000	0.001	0.001	0.000	0.002	0.017	0.022	0.009	0.007
Zr^{4+}	0.001	0.001	0.001	0.001	0.001	0.001	0.001	0.001	0.002	0.002	0.001	0.002
Nb^{5+}	0.003	0.007	0.004	0.004	0.003	0.004	0.003	0.003	0.009	0.005	0.009	0.009
Y^{3+}	0.058	0.050	0.070	0.073	0.063	0.072	0.066	0.069	0.049	0.067	0.032	0.032
Ce^{3+}	0.060	0.022	0.067	0.077	0.054	0.068	0.058	0.062	0.031	0.009	0.022	0.026
La^{3+}	0.007	0.004	0.008	0.009	0.007	0.008	0.007	0.008	0.004	0.003	0.005	0.005
Pr^{3+}	0.007	0.005	0.008	0.010	0.007	0.009	0.007	0.008	0.005	0.002	0.003	0.003
Nd^{3+}	0.035	0.024	0.039	0.042	0.032	0.041	0.033	0.037	0.024	0.009	0.016	0.019
Sm^{3+}	0.007	0.008	0.007	0.008	0.006	0.008	0.006	0.007	0.006	0.004	0.005	0.005
Gd^{3+}	0.007	0.008	0.008	0.009	0.007	0.008	0.008	0.008	0.007	0.008	0.004	0.004
Total	1.097	1.114	1.089	1.091	1.091	1.095	1.084	1.087	1.102	1.090	1.072	1.072
ΣREY	0.181	0.121	0.207	0.228	0.176	0.214	0.186	0.198	0.125	0.102	0.087	0.095

Note: Sample ID is of the form: "SXX.xx" where "SXX" = sample ID as represented in Table 1, "xx" = grain number analysed

Cu₂O, Fe₂O₃, SO₃, P₂O₅ have been assumed to be inclusion bound, so removed from apfu calculations

As₂O₃ has been used for oxide determination, but has been converted to As⁵⁺ within the apfu calculations

a) Zoned Uraninite (with high PbO_2) associated with bornite.
b) Zoned Uraninite (with low PbO_2) associated with bornite.

Table 4a: Electron probe microanalytical data for selected cob-web uraninites (high PbO$_2$ zones).

Sample no.	S15.3 [a]	S15.51 [a]	S17.26 [b]	S17.38 [b]	S18.12 [b]	S18.51 [b]	S18.63 [b]
Valid N (analyses)	3 (Fig. 6d)	8	6 (Fig. 4d)	3	11 (Fig. 6a)	8	1 (Fig. 6b)
(wt%)	Mean	Mean	Mean	Mean	Mean (p1)	Mean	(p4)
UO$_2$	69.77	71.72	66.19	62.99	68.03	70.65	68.88
PbO$_2$	12.31	13.40	18.17	16.09	16.03	15.45	16.28
ThO$_2$	0.46	<mdl	0.12	0.33	0.07	0.34	0.18
Na$_2$O	0.19	0.23	<mdl	0.02	0.10	0.06	0.14
SiO$_2$	0.10	0.12	0.21	0.12	0.35	0.90	0.41
P$_2$O$_5$	<mdl	0.01	0.01	<mdl	0.02	0.05	<mdl
SO$_3$	0.06	0.07	<mdl	<mdl	0.02	<mdl	<mdl
CaO	1.97	2.16	1.06	2.04	1.14	0.90	1.01
TiO$_2$	<mdl	0.01	<mdl	<mdl	0.01	0.07	0.05
MnO	0.12	0.12	<mdl	<mdl	0.04	0.07	0.10
Fe$_2$O$_3$	0.39	0.46	0.74	0.97	0.88	1.27	1.41
Cu$_2$O	0.20	0.14	0.95	1.15	0.85	0.58	0.53
As$_2$O$_3$	0.46	0.52	<mdl	<mdl	0.09	0.11	0.09
ZrO$_2$	0.14	0.18	0.06	0.05	0.07	0.11	0.10
Nb$_2$O$_5$	0.30	0.19	0.12	0.32	0.14	0.30	0.12
Y$_2$O$_3$	2.94	2.25	3.22	3.62	3.33	2.93	2.85
Ce$_2$O$_3$	3.79	2.71	4.53	6.11	3.95	2.68	3.37
La$_2$O$_3$	0.45	0.34	0.52	0.77	0.47	0.39	0.42
Pr$_2$O$_3$	0.44	0.34	0.52	0.73	0.45	0.30	0.38
Nd$_2$O$_3$	2.27	1.84	2.64	3.16	2.15	1.54	1.79
Sm$_2$O$_3$	0.51	0.44	0.51	0.55	0.44	0.38	0.38
Gd$_2$O$_3$	0.53	0.45	0.56	0.64	0.54	0.54	0.48
Total Oxide	97.42	97.74	100.18	99.72	99.18	99.61	98.97
SiO$_2$+CaO+Fe$_2$O$_3$	2.46	2.74	2.01	3.14	2.37	3.08	2.83
Pb/U	0.17	0.18	0.27	0.25	0.23	0.22	0.23

Uraninite Formula (apfu) - based on 2 O

U^{4+}	0.642	0.661	0.606	0.571	0.626	0.642	0.638
Pb^{4+}	0.137	0.149	0.201	0.176	0.178	0.170	0.183
Th^{4+}	0.004	0.000	0.001	0.003	0.001	0.003	0.002
Na$^+$	0.016	0.018	0.000	0.001	0.008	0.004	0.011
Si^{4+}	0.004	0.005	0.009	0.005	0.014	0.037	0.017
Ca^{2+}	0.087	0.096	0.047	0.089	0.051	0.039	0.045
Ti^{4+}	0.000	0.000	0.000	0.000	0.000	0.002	0.002
Mn^{2+}	0.004	0.004	0.000	0.000	0.001	0.002	0.004
As^{5+}	0.012	0.013	0.000	0.000	0.002	0.003	0.002
Zr^{4+}	0.003	0.004	0.001	0.001	0.001	0.002	0.002
Nb^{5+}	0.006	0.004	0.002	0.006	0.003	0.005	0.002
Y^{3+}	0.065	0.050	0.070	0.079	0.073	0.064	0.063
Ce^{3+}	0.057	0.041	0.068	0.091	0.060	0.040	0.051
La^{3+}	0.007	0.005	0.008	0.012	0.007	0.006	0.006
Pr^{3+}	0.007	0.005	0.008	0.011	0.007	0.005	0.006
Nd^{3+}	0.034	0.027	0.039	0.046	0.032	0.022	0.027
Sm^{3+}	0.007	0.006	0.007	0.008	0.006	0.005	0.005
Gd^{3+}	0.007	0.006	0.008	0.009	0.007	0.007	0.007
Total	1.099	1.095	1.075	1.108	1.079	1.059	1.073
ΣREY	0.184	0.141	0.208	0.254	0.193	0.149	0.165

Note: Sample ID is of the form: "SXX.xx" where "SXX" = sample ID as represented in Table 1, "xx" = grain number analysed

Cu$_2$O, Fe$_2$O$_3$, SO$_3$, P$_2$O$_5$ have been assumed to be inclusion bound, so removed from apfu calculations

As$_2$O$_3$ has been used for oxide determination, but has been converted to As^{5+} within the apfu calculations

a) Cob-web uraninite (with high PbO$_2$) associated with chalcopyrite.
b) Cob-web uraninite (with high PbO$_2$) associated with bornite.

Table 4b: Electron probe microanalytical data for selected cob-web uraninites (low PbO$_2$ zones).

Sample no.	S15.3 [a]	S15.51 [a]	S18.24 [b]	S18.59 [b]	S18.12 [b]	S18.12 [b]	S18.63 [b]	S18.51 [b]
Valid N (analyses)	5 (Fig. 6d)	8	11	6	1 (Fig. 6a)	1 (Fig. 6a)	3 (Fig. 6b)	1
(wt%)	Mean	Mean	Mean	Mean	(p2)	(p3)	Mean (p5)	
UO$_2$	75.51	76.05	77.80	75.94	69.52	71.35	74.62	72.67
PbO$_2$	7.05	6.86	5.61	5.47	7.70	8.13	5.25	7.38
ThO$_2$	0.57	<mdl	<mdl	0.27	0.10	<mdl	0.30	0.64
Na$_2$O	0.14	0.21	0.21	0.28	0.34	0.37	0.27	0.20
SiO$_2$	0.15	0.18	1.09	1.09	1.33	1.24	2.13	2.70
P$_2$O$_5$	0.02	0.06	0.05	0.05	0.13	0.10	0.07	0.07
SO$_3$	0.22	0.02	0.05	0.02	<mdl	<mdl	<mdl	<mdl
CaO	3.62	3.90	2.22	1.94	2.56	2.49	2.15	1.69
TiO$_2$	0.06	0.02	0.15	0.22	0.03	0.03	0.36	0.18
MnO	0.36	0.32	0.23	0.17	0.17	0.12	0.26	0.17
Fe$_2$O$_3$	0.65	0.59	1.24	1.32	1.45	1.48	1.95	1.85
Cu$_2$O	0.60	0.18	0.29	0.58	0.76	0.47	0.83	0.31
As$_2$O$_3$	1.07	1.00	0.80	0.50	0.69	0.55	0.61	0.53
ZrO$_2$	0.16	0.16	0.07	0.10	0.07	0.06	0.12	0.07
Nb$_2$O$_5$	1.30	0.35	0.99	0.30	0.14	0.13	0.26	0.63
Y$_2$O$_3$	1.58	1.80	2.53	2.83	3.58	3.00	2.36	2.27
Ce$_2$O$_3$	1.01	1.13	1.11	2.49	3.45	3.02	2.55	2.68
La$_2$O$_3$	0.19	0.23	0.23	0.31	0.42	0.36	0.35	0.37
Pr$_2$O$_3$	0.20	0.26	0.19	0.30	0.38	0.34	0.28	0.25
Nd$_2$O$_3$	1.17	1.25	1.01	1.63	2.07	1.82	1.34	1.54
Sm$_2$O$_3$	0.41	0.47	0.31	0.37	0.58	0.49	0.29	0.31
Gd$_2$O$_3$	0.49	0.52	0.55	0.50	0.55	0.51	0.40	0.42
Total Oxide	96.54	95.57	96.78	96.65	96.01	96.07	96.75	96.94
SiO$_2$+CaO+Fe$_2$O$_3$	4.42	4.67	4.55	4.34	5.21	5.34	6.23	6.24
Pb/U	0.09	0.09	0.07	0.07	0.11	0.11	0.07	0.10

Uraninite Formula (apfu) - based on 2 O

U^{4+}	0.689	0.703	0.705	0.700	0.629	0.652	0.667	0.636
Pb^{4+}	0.078	0.077	0.062	0.061	0.084	0.090	0.057	0.078
Th^{4+}	0.005	0.000	0.000	0.003	0.001	0.000	0.003	0.006
Na^{+}	0.011	0.017	0.017	0.022	0.027	0.029	0.021	0.015
Si^{4+}	0.006	0.007	0.044	0.045	0.054	0.051	0.086	0.106
Ca^{2+}	0.159	0.173	0.097	0.086	0.111	0.110	0.092	0.071
Ti^{4+}	0.002	0.001	0.005	0.007	0.001	0.001	0.011	0.005
Mn^{2+}	0.012	0.011	0.008	0.006	0.006	0.004	0.009	0.006
As^{5+}	0.027	0.025	0.020	0.013	0.017	0.014	0.015	0.013
Zr^{4+}	0.003	0.003	0.001	0.002	0.001	0.001	0.002	0.001
Nb^{5+}	0.024	0.007	0.018	0.006	0.003	0.002	0.005	0.011
Y^{3+}	0.034	0.040	0.055	0.062	0.078	0.065	0.050	0.047
Ce^{3+}	0.015	0.017	0.017	0.038	0.051	0.045	0.037	0.039
La^{3+}	0.003	0.003	0.003	0.005	0.006	0.005	0.005	0.005
Pr^{3+}	0.003	0.004	0.003	0.005	0.006	0.005	0.004	0.004
Nd^{3+}	0.017	0.019	0.015	0.024	0.030	0.027	0.019	0.022
Sm^{3+}	0.006	0.007	0.004	0.005	0.008	0.007	0.004	0.004
Gd^{3+}	0.007	0.007	0.007	0.007	0.007	0.007	0.005	0.005
Total	1.103	1.121	1.082	1.094	1.120	1.115	1.093	1.076
ΣREY	0.085	0.097	0.104	0.145	0.186	0.162	0.126	0.126

Note: Sample ID is of the form: "SXX.xx" where "SXX" = sample ID as represented in Table 1, "xx" = grain number analysed

Cu$_2$O, Fe$_2$O$_3$, SO$_3$, P$_2$O$_5$ have been assumed to be inclusion bound, so removed from apfu calculations

As$_2$O$_3$ has been used for oxide determination, but has been converted to As^{5+} within the apfu calculations

a) Cob-web uraninite (with low PbO$_2$) associated with chalcopyrite.
b) Cob-web uraninite (with low PbO$_2$) associated with bornite.

Table 5: Electron probe microanalytical data for massive uraninites.

Sample no.	S11.37 & S11.39 [a]	S11.46-48 & S11.52 & S11.55 [a]	S11.37 & S11.39 [b]	S11.46-48 & S11.52 & S11.55 [b]	S21 [c]	S4 [d]	S1 [e]
Valid N (analyses)	72 (Fig. 7d)	39 (Fig. 7d)	32 (Fig. 7d)	9 (Fig. 7d)	31 (Fig. 7c)	4 (Fig. 7b)	28 (Fig. 7a)
(wt%)	Mean	Mean	Mean	Mean	Mean	Mean	Mean
UO_2	78.86	79.20	81.68	80.39	78.94	79.76	82.02
PbO_2	2.18	2.21	3.76	2.77	6.92	6.41	4.38
ThO_2	<mdl	<mdl	<mdl	<mdl	<mdl	<mdl	<mdl
Na_2O	0.57	0.58	0.46	0.53	0.25	0.23	0.53
SiO_2	2.34	2.36	1.40	2.42	0.37	0.91	3.03
P_2O_5	0.18	0.19	0.11	0.16	0.04	0.01	0.45
SO_3	0.03	0.02	0.02	0.02	0.16	0.04	0.11
CaO	4.62	4.64	3.66	3.67	4.86	2.58	2.36
TiO_2	<mdl	<mdl	<mdl	<mdl	0.46	0.19	0.34
MnO	0.63	0.59	0.46	0.51	0.33	0.27	0.33
Fe_2O_3	1.08	0.98	0.76	0.99	0.70	1.58	0.76
Cu_2O	0.08	0.09	0.07	0.12	0.70	1.03	0.41
As_2O_3	0.34	0.33	0.21	0.32	0.50	0.99	0.15
ZrO_2	0.10	0.14	0.11	0.12	0.08	0.14	0.22
Nb_2O_5	<mdl	0.04	0.04	0.04	0.09	0.06	<mdl
Y_2O_3	1.87	1.88	1.74	1.81	1.47	1.38	0.58
Ce_2O_3	0.52	0.53	0.44	0.46	0.88	0.96	0.64
La_2O_3	0.21	0.21	0.19	0.20	0.23	0.31	0.30
Pr_2O_3	0.11	0.11	0.11	0.13	0.17	0.14	<mdl
Nd_2O_3	0.83	0.84	0.79	0.79	0.86	0.67	0.39
Sm_2O_3	0.27	0.29	0.24	0.29	0.37	0.19	0.09
Gd_2O_3	0.42	0.40	0.41	0.39	0.44	0.20	0.11
Total Oxide	95.30	95.66	96.68	96.17	98.84	98.08	97.32
$SiO_2+CaO+Fe_2O_3$	8.04	7.98	5.82	7.09	5.93	5.07	6.14
Pb/U	0.03	0.03	0.05	0.03	0.09	0.08	0.05

Uraninite Formula (apfu) - based on 2 O

U^{4+}	0.697	0.696	0.743	0.711	0.707	0.733	0.723
Pb^{4+}	0.023	0.023	0.041	0.030	0.075	0.071	0.047
Th^{4+}	0.000	0.000	0.000	0.000	0.000	0.000	0.000
Na^+	0.044	0.045	0.036	0.041	0.019	0.018	0.041
Si^{4+}	0.093	0.093	0.057	0.096	0.015	0.038	0.120
Ca^{2+}	0.196	0.196	0.160	0.156	0.209	0.114	0.100
Ti^{4+}	0.000	0.000	0.000	0.000	0.014	0.006	0.010
Mn^{2+}	0.021	0.020	0.016	0.017	0.011	0.009	0.011
As^{5+}	0.008	0.008	0.005	0.008	0.012	0.025	0.003
Zr^{4+}	0.002	0.003	0.002	0.002	0.002	0.003	0.004
Nb^{5+}	0.000	0.001	0.001	0.001	0.002	0.001	0.000
Y^{3+}	0.040	0.039	0.038	0.038	0.032	0.030	0.012
Ce^{3+}	0.008	0.008	0.007	0.007	0.013	0.015	0.009
La^{3+}	0.003	0.003	0.003	0.003	0.003	0.005	0.004
Pr^{3+}	0.002	0.002	0.002	0.002	0.003	0.002	0.000
Nd^{3+}	0.012	0.012	0.012	0.011	0.012	0.010	0.005
Sm^{3+}	0.004	0.004	0.003	0.004	0.005	0.003	0.001
Gd^{3+}	0.006	0.005	0.006	0.005	0.006	0.003	0.001
Total	1.158	1.158	1.131	1.133	1.140	1.086	1.094
ΣREY	0.073	0.073	0.069	0.070	0.074	0.067	0.034

Note: Sample ID is of the form: "SXX.xx" where "SXX" = sample ID as represented in Table 1, "xx" = grain number analysed

    Cu_2O, Fe_2O_3, SO_3, P_2O_5 have been assumed to be inclusion bound, so removed from apfu calculations

    As_2O_3 has been used for oxide determination, but has been converted to As^{5+} within the apfu calculations

a) Massive uraninite (with high CaO) associated with chalcopyrite.
b) Massive uraninite (with low CaO) associated with chalcopyrite.
c) Massive (crustiform) uraninite associated with bornite and/or chalcocite.
d) Uraninite pisoliths associated with bornite and/or chalcocite.
e) Massive uraninite intergrown with coffinite.

Table 6a: Calculated structural formulae for analysed Class 1-3 uraninites (apfu).

	Class 1 Primary			Class 2 Zoned (high-Pb)									Class 2 Zoned (low-Pb)			Class 3 Cob-web (high-Pb)						
	S17.11a	S17.11b	S15.68	S17.12	S17.28	S17.36	S17.47	S17.52	S17.61	S17.63	S18.29	S18.29	S17.12	S18.29	S18.2	S15.3	S15.51	S17.26	S17.38	S18.12	S18.51	S18.63
U^{4+}	0.393	0.385	0.416	0.399	0.391	0.377	0.404	0.375	0.408	0.395	0.504	0.502	0.418	0.462	0.512	0.402	0.430	0.420	0.312	0.431	0.492	0.457
Pb^{4+}	0.196	0.191	0.201	0.164	0.191	0.188	0.191	0.183	0.195	0.193	0.148	0.148	0.074	0.040	0.071	0.137	0.149	0.201	0.176	0.178	0.170	0.183
Th^{4+}	0.069	0.069	0.000	0.000	0.001	0.003	0.004	0.001	0.007	0.008	0.000	0.000	0.001	0.000	0.000	0.004	0.000	0.001	0.003	0.001	0.003	0.002
Si^{4+}	0.002	0.023	0.005	0.009	0.006	0.004	0.007	0.006	0.009	0.004	0.034	0.029	0.012	0.054	0.021	0.004	0.005	0.009	0.005	0.014	0.037	0.017
Zr^{4+}	0.001	0.001	0.001	0.001	0.001	0.001	0.001	0.001	0.001	0.001	0.001	0.002	0.001	0.002	0.002	0.003	0.004	0.001	0.001	0.001	0.002	0.002
Ti^{4+}	0.000	0.001	0.000	0.000	0.000	0.000	0.000	0.000	0.000	0.000	0.001	0.001	0.001	0.002	0.002	0.000	0.000	0.000	0.000	0.000	0.002	0.002
Total (U^*)	0.660	0.670	0.624	0.573	0.590	0.573	0.606	0.566	0.621	0.601	0.687	0.683	0.508	0.560	0.609	0.551	0.588	0.632	0.497	0.626	0.707	0.662
U^{6+} (x)	0.174	0.167	0.187	0.237	0.217	0.221	0.223	0.232	0.207	0.213	0.178	0.179	0.273	0.248	0.220	0.240	0.231	0.186	0.260	0.195	0.149	0.182
Y^{3+}	0.063	0.061	0.067	0.058	0.070	0.073	0.063	0.072	0.066	0.069	0.032	0.032	0.050	0.049	0.067	0.065	0.050	0.070	0.079	0.073	0.064	0.063
Ce^{3+}	0.065	0.061	0.066	0.060	0.067	0.077	0.054	0.068	0.058	0.062	0.022	0.026	0.022	0.031	0.009	0.057	0.041	0.068	0.091	0.060	0.040	0.051
La^{3+}	0.008	0.008	0.008	0.007	0.008	0.009	0.007	0.008	0.007	0.008	0.005	0.005	0.004	0.004	0.003	0.007	0.005	0.008	0.012	0.007	0.006	0.006
Pr^{3+}	0.007	0.007	0.008	0.007	0.008	0.010	0.007	0.009	0.007	0.008	0.003	0.003	0.005	0.005	0.002	0.007	0.005	0.008	0.011	0.007	0.005	0.006
Nd^{3+}	0.033	0.033	0.040	0.035	0.039	0.042	0.032	0.041	0.033	0.037	0.016	0.019	0.024	0.024	0.009	0.034	0.027	0.039	0.046	0.032	0.022	0.027
Sm^{3+}	0.005	0.007	0.007	0.007	0.007	0.008	0.006	0.008	0.006	0.007	0.005	0.005	0.008	0.006	0.004	0.007	0.006	0.007	0.008	0.006	0.005	0.005
Gd^{3+}	0.007	0.007	0.008	0.007	0.008	0.009	0.007	0.008	0.008	0.008	0.004	0.004	0.008	0.007	0.008	0.007	0.006	0.008	0.009	0.007	0.007	0.007
REY* (y)	0.189	0.185	0.204	0.181	0.207	0.228	0.176	0.214	0.186	0.198	0.087	0.095	0.121	0.125	0.102	0.184	0.141	0.208	0.254	0.193	0.149	0.165
Ca^{2+}	0.044	0.042	0.052	0.070	0.053	0.056	0.055	0.060	0.048	0.055	0.081	0.082	0.151	0.108	0.101	0.087	0.096	0.047	0.089	0.051	0.039	0.045
Mn^{2+}	0.001	0.000	0.000	0.002	0.000	0.000	0.000	0.000	0.000	0.000	0.007	0.006	0.009	0.009	0.007	0.004	0.004	0.000	0.000	0.001	0.002	0.004
M1 (z)	0.045	0.042	0.052	0.072	0.053	0.056	0.055	0.060	0.048	0.055	0.088	0.088	0.160	0.117	0.108	0.091	0.100	0.047	0.089	0.052	0.042	0.049
Na^+ (u)	0.000	0.000	0.000	0.025	0.016	0.009	0.028	0.017	0.019	0.015	0.014	0.011	0.017	0.026	0.023	0.016	0.018	0.000	0.001	0.008	0.004	0.011
As^{5+}	0.000	0.000	0.000	0.007	0.002	0.000	0.001	0.001	0.000	0.002	0.009	0.007	0.028	0.017	0.022	0.012	0.013	0.000	0.000	0.002	0.003	0.002
Nb^{5+}	0.001	0.002	0.007	0.003	0.004	0.004	0.003	0.004	0.003	0.003	0.009	0.009	0.007	0.009	0.005	0.006	0.004	0.002	0.006	0.003	0.005	0.002
M2 (w)	0.001	0.002	0.007	0.010	0.005	0.004	0.004	0.006	0.003	0.005	0.018	0.017	0.035	0.026	0.028	0.017	0.017	0.002	0.006	0.005	0.008	0.004
$U^{6+}/(U^{4+}+U^{6+})$	0.307	0.302	0.310	0.372	0.357	0.370	0.356	0.382	0.336	0.350	0.261	0.263	0.395	0.349	0.301	0.374	0.349	0.307	0.454	0.312	0.233	0.284

Note: Critical assumptions include -

- Mineral stoichiometry conforms to ideal $(U.....)O_2$.
- Cation valencies given in Tables 2-5 are correct.
- S^{6+}, Fe^{3+}, Cu^+, P^{5+} have been omitted since these elements are probably restricted to nanoscale inclusions.
- As is present as As^{5+}.
- All other elements measured are lattice-bound.
- Any anion substitutions (e.g., F^-, OH^- or CO_3^{2-} for O^{2-}) is insignificant.

Table 6b: Calculated structural formulae for analysed Class 3 (low-Pb only) and 4 uraninites (apfu).

	Class 3 Cob-web (low-Pb)								Class 4 Massive						
	S15.3	S18.24	S18.59	S18.12	S18.12	S18.63	S18.51	S15.51	S11.37 & S11.39	S11.46-48 & S11.52 & S11.55	S11.37 & S11.39	S11.46-48 & S11.52 & S11.55	S21	S4	S1
U^{4+}	0.440	0.504	0.470	0.342	0.376	0.440	0.448	0.415	0.333	0.333	0.434	0.398	0.380	0.522	0.494
Pb^{4+}	0.078	0.062	0.061	0.084	0.090	0.057	0.078	0.077	0.023	0.023	0.041	0.030	0.075	0.071	0.047
Th^{4+}	0.005	0.000	0.003	0.001	0.000	0.003	0.006	0.000	0.000	0.000	0.000	0.000	0.000	0.000	0.000
Si^{4+}	0.006	0.044	0.045	0.054	0.051	0.086	0.106	0.007	0.093	0.093	0.057	0.096	0.015	0.038	0.120
Zr^{4+}	0.003	0.001	0.002	0.001	0.001	0.002	0.001	0.003	0.002	0.003	0.002	0.002	0.002	0.003	0.004
Ti^{4+}	0.002	0.005	0.007	0.001	0.001	0.011	0.005	0.001	0.000	0.000	0.000	0.000	0.014	0.006	0.010
Total (U^*)	0.535	0.616	0.587	0.484	0.519	0.598	0.645	0.503	0.451	0.452	0.535	0.527	0.485	0.640	0.675
U^{6+} (x)	0.249	0.201	0.230	0.287	0.276	0.227	0.188	0.288	0.364	0.363	0.309	0.313	0.327	0.211	0.229
Y^{3+}	0.034	0.055	0.062	0.078	0.065	0.050	0.047	0.040	0.040	0.039	0.038	0.038	0.032	0.030	0.012
Ce^{3+}	0.015	0.017	0.038	0.051	0.045	0.037	0.039	0.017	0.008	0.008	0.007	0.007	0.013	0.015	0.009
La^{3+}	0.003	0.003	0.005	0.006	0.005	0.005	0.005	0.003	0.003	0.003	0.003	0.003	0.003	0.005	0.004
Pr^{3+}	0.003	0.003	0.005	0.006	0.005	0.004	0.004	0.004	0.002	0.002	0.002	0.002	0.003	0.002	0.000
Nd^{3+}	0.017	0.015	0.024	0.030	0.027	0.019	0.022	0.019	0.012	0.012	0.012	0.011	0.012	0.010	0.005
Sm^{3+}	0.006	0.004	0.005	0.008	0.007	0.004	0.004	0.007	0.004	0.004	0.003	0.004	0.005	0.003	0.001
Gd^{3+}	0.007	0.007	0.007	0.007	0.007	0.005	0.005	0.007	0.006	0.005	0.006	0.005	0.006	0.003	0.001
REY* (y)	0.085	0.104	0.145	0.186	0.162	0.126	0.126	0.097	0.073	0.073	0.069	0.070	0.074	0.067	0.034
Ca^{2+}	0.159	0.097	0.086	0.111	0.110	0.092	0.071	0.173	0.196	0.196	0.160	0.156	0.209	0.114	0.100
Mn^{2+}	0.012	0.008	0.006	0.006	0.004	0.009	0.006	0.011	0.021	0.020	0.016	0.017	0.011	0.009	0.011
M1 (z)	0.172	0.105	0.092	0.117	0.114	0.101	0.077	0.185	0.218	0.216	0.176	0.174	0.221	0.124	0.111
Na^+ (u)	0.011	0.017	0.022	0.027	0.029	0.021	0.015	0.017	0.044	0.045	0.036	0.041	0.019	0.018	0.041
As^{5+}	0.027	0.020	0.013	0.017	0.014	0.015	0.013	0.025	0.008	0.008	0.005	0.008	0.012	0.025	0.003
Nb^{5+}	0.024	0.018	0.006	0.003	0.002	0.005	0.011	0.007	0.000	0.001	0.001	0.001	0.002	0.001	0.000
M2 (w)	0.051	0.038	0.018	0.020	0.016	0.020	0.024	0.032	0.008	0.009	0.006	0.008	0.014	0.026	0.003
$U^{6+}/ (U^{4+}+U^{6+})$	0.361	0.286	0.329	0.456	0.423	0.340	0.295	0.409	0.522	0.522	0.416	0.440	0.463	0.288	0.316

Note: Critical assumptions include -

- Mineral stoichiometry conforms to ideal $(U.....)O_2$.

- Cation valencies given in Tables 2-5 are correct.

- S^{6+}, Fe^{3+}, Cu^+, P^{5+} should be omitted since these elements are probably restricted to nanoscale inclusions.

- As is present as As^{5+}.

- All other elements measured are lattice-bound.

- Any anion substitutions (e.g., F^-, OH^- or CO_3^{2-} for O^{2-}) is insignificant.